LATVIAN JOURNAL of PHYSICS and TECHNICAL SCIENCES

ISSN 0868 - 8257

4

(Vol. 60)

2023

CONTENTS

LATVIAN
JOURNAL
of
PHYSICS
and TECHNICAL
SCIENCES

LATVIJAS
FIZIKAS
un TEHNISKO
ZINĀTŅU
ŽURNĀLS

ЛАТВИЙСКИЙ
ФИЗИКО-
ТЕХНИЧЕСКИЙ
ЖУРНАЛ

Published six times a year since February 1964
Iznāk sešas reizes gadā kopš 1964. gada februāra
Выходит шесть раз в год с февраля 1964 года

4 (Vol. 60) • **2023**

RĪGA

Language Editor: O. Ivanova
Computer Designer: I. Begicevs

INDEXED (PUBLISHED) IN

www.scopus.com
www.sciendo.com
EBSCO (Academic Search Complete, www.epnet.com), INSPEC (www.iee.org.com).
VINITI (www.viniti.ru), Begell House Inc/ (EDC, www.edata-center.com).

Issuers: Institute of Physical Energetics,
Institute of Solid State Physics, University of Latvia
Registration Certificate Number: 000700221

Editorial Contacts:
14 Dzerbenes Street, Riga, LV-1006
LATVIA
tel: +371 26245896
M: +371 29363105
leo@lza.lv

LATVIAN JOURNAL OF PHYSICS
AND TECHNICAL SCIENCES
2023, N 4

DOI: 10.2478/lpts-2023-0021

ADAPTIVE FAULT LOCATOR FOR HIGH-VOLTAGE TRANSMISSION LINES BASED ON THE ESTIMATION OF POWER SYSTEM MODEL PARAMETERS

I. Zalitis, A. Dolgicers, J. Kozadajevs, J. Berkolds

Riga Technical University, Institute of Power Engineering
12-k1 Azenes Str., Riga, LV-1010, LATVIA
*e-mail: ivars.zalitis@rtu.lv

This paper presents an adaptive transmission line fault location method, which incorporates fault location devices at both line ends and utilises data import from a supervisory control and data acquisition system without strictly requiring data synchronisation. The developed method aims at achieving a higher degree of robustness, adaptiveness and accuracy. The adaptiveness is achieved by dynamic updating of mathematical models used on the basis of network-wide information, such as data on the state of circuit-breakers and apparent power at load and generation nodes. The robustness and accuracy are enhanced by incorporating two stages of identification of model parameters with the goal of reducing the decision variable space for the stage identifying fault parameters. Furthermore, in addition to utilisation of all measurements available at a particular substation, the developed method partially employs the measurements from the other end of the line by means of result cross-checks, but does not require a full data set, unlike deterministic-model-based methods. An optimisation-based approach, redundancy on the basis of extended measurement set, and cross-checks reduce the risk of fault location errors due to measurement errors or "voids" in the data available. Testing of the developed method demonstrates its accuracy and robustness in a wide range of pre-fault and fault regime scenarios, even when considering various pre-fault contingencies.

Keywords: *Fault location*, *modelling*, *optimisation, transmission lines*.

1. INTRODUCTION

Research has led to the development of various fault location (FL) techniques for high-voltage (HV) overhead transmission lines (OHTLs). First, one-terminal-measurement-based (OTMB) methods with fault loop impedance measurements were developed [1]. The improved digital device adaptation of this approach [2] is still in use in parts of the Baltic power systems. In contrast to the developed one, these methods are simpler and easier to implement, but they sometimes prove inaccurate due to the reactance effect [3], [4]. Additionally, if mismatching results of such FL devices from both substations are used, it requires experienced personnel to determine the correct fault location, which is avoided by the developed method.

Introduction of communication networks between different substations made measurements from both terminals available for use with corresponding fault point voltage equations to directly calculate the fault distance at once. One of these two-terminal-measurement-based (TTMB) methods utilises negative-sequence (NS) current and voltage phasors obtained at both line terminals [2], a different one uses both the positive-sequence (PS) and NS phasors [5]. TTMB methods are easy to implement and in most cases, they are more accurate than OTMB methods because they negate the reactance effect. The two equations of the voltage at the fault point are sometimes kept separate and optimisation is used to minimise the difference of the results obtained from them [6]–[8]. Both approaches are dependent on precise synchronisation of measurements during the fault and the reliability of the communication network. Falling trees, with a high probability, can damage not only the power line but also the communication cable attached to it, making such FL designs less reliable compared to the presented method. A method similar to [6]–[8], which also estimates the shift angle of unsynchronised measurements, has been proposed in [9]. This method can potentially avoid the problem of measurement synchronisation, but there is a risk that the estimated angle will be shifted by one or more periods, which could introduce errors if the fault path resistance is not stationary (e.g., faults caused by fallen trees, especially pines and similar trees).

Wide interest has also been devoted to the travelling-wave (TW) FL methods. Most TW methods determine the fault distance by either measuring the time required for the transient fault wave with a known wave propagation velocity to reflect from the fault location [10], [11] or the difference between the wave arrival times at both substations. TW methods are considered accurate but they require good correlators to recognise the actual fault wave and avoid errors caused by wave distortions due to irregularities of the power system or wave decay [12], [13]. Methods that apply an optimisation with measurements of fault transients have been proposed for FL as well [7], [14]; however, these methods, as well as the original-type TW methods, require a high sampling frequency resulting in more expensive devices, which is not required for the developed method.

A different group of methods is based on artificial neural networks (ANNs) [15]–[17]. ANNs provide an opportunity for performing different functions simultaneously, such as identification of the fault type and fault location, with a satisfactory accuracy.

These methods are promising [18] but they require an extensive training database and can be complicated to implement. A similar OTMB method using the k-nearest neighbour technique [19], which only uses voltage signal measurements, obtains the harmonic spectrum of this signal, and then uses a database of similarly processed recordings to recognise the fault location. This allows avoiding problems associated with communication networks and potential current transformer saturation; however, this method requires a high sampling frequency and a sufficient database of fault recordings. In comparison to these methods, the developed method only requires basic network data and periodic updates on the network structure and the power generated and consumed at the modelled nodes.

A FL method based on Monte-Carlo optimisation is also known [20]. This OTMB method replaces the unknown impedance of the remote-end power system with a probability distribution of its values and filters out solution variants that imply reactive power consumption at the fault location. This approach can be easily adapted to different fault types and retains a satisfactory accuracy even in cases when line-specific parameters vary, but it has a very high computation cost and papers that present this method do not consider complex line configurations.

This paper presents a future study on the parameter-estimation-based FL method [13]. The goal of this research is to make the previously developed method more adaptive, robust and accurate, first, by introducing automatic updates of the models, corresponding measurement data sets, and model outputs used, and by additional estimation of sequence impedances of the equivalent power system when network simplifications are employed. These improvements provide an ability to reflect changes of network topology due to disconnections of network elements prior to a fault not only in the exactly modelled part of the network, but also in network parts represented by an equivalent power system. Dynamic model updates are made on the basis of data from a supervisory control and data acquisition (SCADA) system. This includes the state of circuit breakers (CBs) to make the model graph match the actual system in exactly the modelled part, and apparent power at the connection nodes of modelled equivalent generation and load is also fetched from SCADA. Apparent powers are used directly in the model utilised by the first parameter estimation stage and later to determine generator electromotive forces (EMFs) and to calculate equivalent impedances representing loads for the model used by the second estimation stage. Furthermore, one extended model considering faults at any transmission line in a precisely modelled network part can now be used for several substations. None of the data requested from a SCADA system have strict requirements regarding synchronisation or transfer speed. Secondly, a further improvement is achieved by performing cross-checks of results obtained by individual FL devices at both ends of the faulted line before the selection of the best solution variant. The case study, which considers not only changes in network topology prior to a fault but also different pre-fault and fault scenario combinations, demonstrates the capabilities of the developed method.

Section 2 presents the new adaptive features and the methodology applied. Section 3 describes the case study network and discusses the obtained results. Finally, conclusions are provided.

2. AN ADAPTIVE FAULT LOCATION BASED ON TWO STAGES OF SYSTEM MODEL PARAMETER ESTIMATION

2.1. New Adaptive Features of the Developed Method

In order to overcome limitations imposed by the incomplete scope of information available to an OTMB FL device, and to make the developed FL method more adaptive while avoiding a requirement for exchanging precisely synchronised data, several options are chosen.

First, an ability to adapt models used for the two estimation stages prior to a fault is integrated in the developed method utilising indications of states of CBs from a SCADA system and element IDs assigned to each branch and at least part of the nodes of the equivalent circuits used. When disconnections of network elements split a model of a pre-fault state, the network parts that do not include FL devices controlling a faulted line are removed from the updated versions utilised for both pre-fault and fault state models to save computation time. While the accuracy of many existing FL methods is unaffected (e.g., TTMB methods [6]–[9],) or can even potentially improve (e.g., simple OTMB methods [1], [2]) in case of such pre-fault contingencies, the accuracy of methods such as those using ANNs, if the training database used does not include faults after contingencies, or those estimating the impedance of the equivalent power system as connected at the end of the line [20], if the other end of the line were to be disconnected, may be degraded.

Second, the developed method also requires the apparent powers of generators and loads available for corresponding nodes in both of the models used. These can be estimated [13], if necessary, but that increases the computation cost and the risk of errors, so measured data will be welcomed. In the pre-fault state model used by the first estimation stage, all of these apparent powers are included as power demand or injections at their respective nodes based on element IDs and node types (demand, power losses, constant power generation, generation with the possibility of power balancing). The only exception is when a pre-fault contingency breaks a link between a network part including relevant FL devices and an equivalent power system. In this case, if there is at least one source capable of balancing power in the remaining network part, one of the said sources is modelled as a constant EMF (balancing) source while others will remain as power injections. In order to achieve this, the model of the pre-fault state was changed from the one used previously [13] to one that operates with phase-to-earth voltages and employs earth as the base node of an equivalent circuit. The apparent powers of demand and generator nodes are also used for the model of the fault state, where equivalent load impedances are updated and generator powers are used to estimate generator EMFs at the moment of fault occurrence. The described model updates using SCADA data take place periodically before the occurrence of a fault, making both models updated near real time but without a strict synchronisation requirement for data exchange.

2.2. Estimation of Unknown Model Parameters

Both estimation stages are defined as optimisation tasks, which minimises the difference between the measurements from the controlled substation and the corresponding outputs of a mathematical model of the power system. The overall goal for both estimation stages is to determine their respective unknown model parameters with the best possible accuracy and within reasonable computation time. However, a strict limit of a maximum error of 5 % is only applied to the fault distance estimate, as estimation of other parameters is of secondary importance.

The first estimation stage is active before a fault occurs. and its purpose is to reduce the number of unknown parameters for the second estimation stage by determining the PS impedance of an equivalent power system, if such a simplification is used. As the NS current circulation paths coincide with PS ones, an estimate of a PS impedance also allows greatly limiting the expected values of an NS impedance. This is possible because the main reason for their difference is the dissimilarity between PS and NS impedances of rotating electric machines, which are well defined [21]. This stage uses phasors of the calculation phase obtained from processed measurement recordings of substation bus voltages and currents as well as power flows from all the branches connected to the substation buses.

These values are automatically compared to the corresponding outputs of a mathematical model of a pre-fault state. Next, a "difference" value, Δ, is calculated, which is utilised here as a conceptual representation of the actual objective function f_{OBJ} (Subsection 2.3). When the convergence criteria are met for the optimisation at both ends of the faulted line, the obtained solution variants are exchanged between FL devices for a cross-check (Subsection 2.3) before the selection of a final estimate. The PS impedance obtained is then used to update the pre-fault state model utilised to estimate generator EMFs. Next, the estimated PS impedance of an equivalent power system and generator EMFs are updated in the fault state model. At the same time, the PS impedance is used to set limits to potential values of the modulus and the X / R ratio of the NS impedance of the power system for the second estimation stage:

$$\begin{cases} 0.18\left|\dot{Z}_{\mathrm{SYS}}^{1}\right| \le \left|\dot{Z}_{\mathrm{SYS}}^{2}\right| \le 0.42\left|\dot{Z}_{\mathrm{SYS}}^{1}\right| \\ 0.1\, X_{\mathrm{SYS}}^{1}/R_{\mathrm{SYS}}^{1} - 2 \le X_{\mathrm{SYS}}^{2}/R_{\mathrm{SYS}}^{2} \le 0.4\, X_{\mathrm{SYS}}^{1}/R_{\mathrm{SYS}}^{1} + 2 \end{cases}, \quad (1)$$

where $\dot{Z}_{\mathrm{SYS}}^{1}$ – the estimated PS impedance of an equivalent power system, Ω; $\dot{Z}_{\mathrm{SYS}}^{2}$ – the NS impedance of an equivalent power system, Ω; R_{SYS}^{1}, R_{SYS}^{2}, X_{SYS}^{1}, X_{SYS}^{2} – the active and reactive components of $\dot{Z}_{\mathrm{SYS}}^{1}$ and $\dot{Z}_{\mathrm{SYS}}^{2}$, respectively, Ω.

The limits (1) are introduced by considering several factors. Firstly, on average for different generators, moduli of $\dot{Z}_{\mathrm{G}}^{2}$ constitute approximately 10 %–20 % of moduli $\dot{Z}_{\mathrm{G}}^{1}$ and ratios $X_{\mathrm{G}}^{2}/R_{\mathrm{G}}^{2}$ constitute 2 %–13 % of $X_{\mathrm{G}}^{1}/R_{\mathrm{G}}^{1}$ at steady-state conditions [21]. Secondly, the difference between PS and NS impedances is assumed lower than that for generators, considering that there should be a substantial number of connecting elements between remote generators and the busbars of an equivalent power system for one to employ such a simplification. Thirdly, the limits are then slightly extended by 2 % and 2 p.u. to account for potential errors of the estimated $\left|\dot{Z}_{\mathrm{SYS}}^{1}\right|$ and $X_{\mathrm{SYS}}^{1}/R_{\mathrm{SYS}}^{1}$ values.

As can be seen, the first estimation stage both removes one decision variable for the estimation of fault state parameters and limits the search space for a second one, thus improving the robustness and accuracy of the developed method. Addition of this stage does increase the total computation cost; however, this is partially offset by the reduced search space for the second stage and it does not increase the FL time as the first stage is active only before a fault occurs.

The second estimation stage is activated when a fault is cleared and measurement signals have been processed by removing the free decaying component (DC offset) and extracting phasors of the fundamental frequency [22] from the first full cycle. This part of signal recordings is chosen to minimise the possible differences between the values of EMFs used in a fault state model and actual EMFs due to potential electromechanical transients. The second estimation stage is tasked with estimation of fault distance α, equivalent fault path resistance R_{F}, NS, and zero-sequence (ZS) impedance of an equivalent power system $\dot{Z}_{\mathrm{SYS}}^{0}$. For calculating the objective function, the following phasors and values are determined and used separately by FL devices at both ends of a faulted OHTL:

- The phase voltages of busbars at the substation where the FL device is installed, and symmetrical components of the calculation phase derived from them;
- Phase currents for each branch connected to the substation and symmetrical components of the calculation phase currents derived from them;
- The symmetrical components of the calculation phase apparent power for each branch connected to the substation;
- The fault distance that would be analytically calculated by an existing OTMB FL method.

All of the phasors obtained from each of the branches that are connected to the substation are automatically arranged in a vector using an updated "relay" terminal (FL device) and element IDs. Thus, both the set of the measurement phasors and the results of the steady-state simulations automatically retain correct order and match an up-to-date pre-fault network topology. The fault distance estimate included as one of the measurements uses apparent reactance for a distance calculation and is implemented in an existing relay terminal [2]. For phase-to-earth faults in parallel OHTL, this distance is calculated according to the following equation:

$$\alpha = \mathrm{Im}\left(\dot{U}_{\mathrm{Fph}}/\dot{I}_{\mathrm{FL}}^{0}\right)/\left(\mathrm{Im}\left(\dot{Z}_{\mathrm{L1km}}^{1}\left[\dot{I}_{\mathrm{Fph}}+\dot{k}_{0\mathrm{FL}}\dot{I}_{\mathrm{FL}}^{0}+\dot{k}_{0\mathrm{M}}\dot{I}_{\mathrm{PL}}^{0}\right]/\dot{I}_{\mathrm{FL}}^{0}\right)L_{\mathrm{L}}\right), \tag{2}$$

where α – the fault distance, p.u.; $\dot{U}_{\mathrm{Fph}}$ and $\dot{I}_{\mathrm{Fph}}$ – the faulted phase voltage and current of the faulted line, V and A; $\dot{I}_{\mathrm{FL}}^{0}$ and $\dot{I}_{\mathrm{PL}}^{0}$ – the ZS currents of the faulted line and the healthy parallel line, A; $\dot{Z}_{\mathrm{L1km}}^{1}$ – the PS impedance of a one-kilometre-long section of the faulted line, Ω; $\dot{k}_{0\mathrm{FL}}$ – a ZS compensation coefficient, p.u.; $\dot{k}_{0\mathrm{M}}$ – the ZS mutual induction compensation coefficient (the ratio between the impedance of ZS mutual induction between both lines and the PS impedance of the faulted line), p.u.

When other fault types are considered, a similar OTMB FL formula would be used instead.

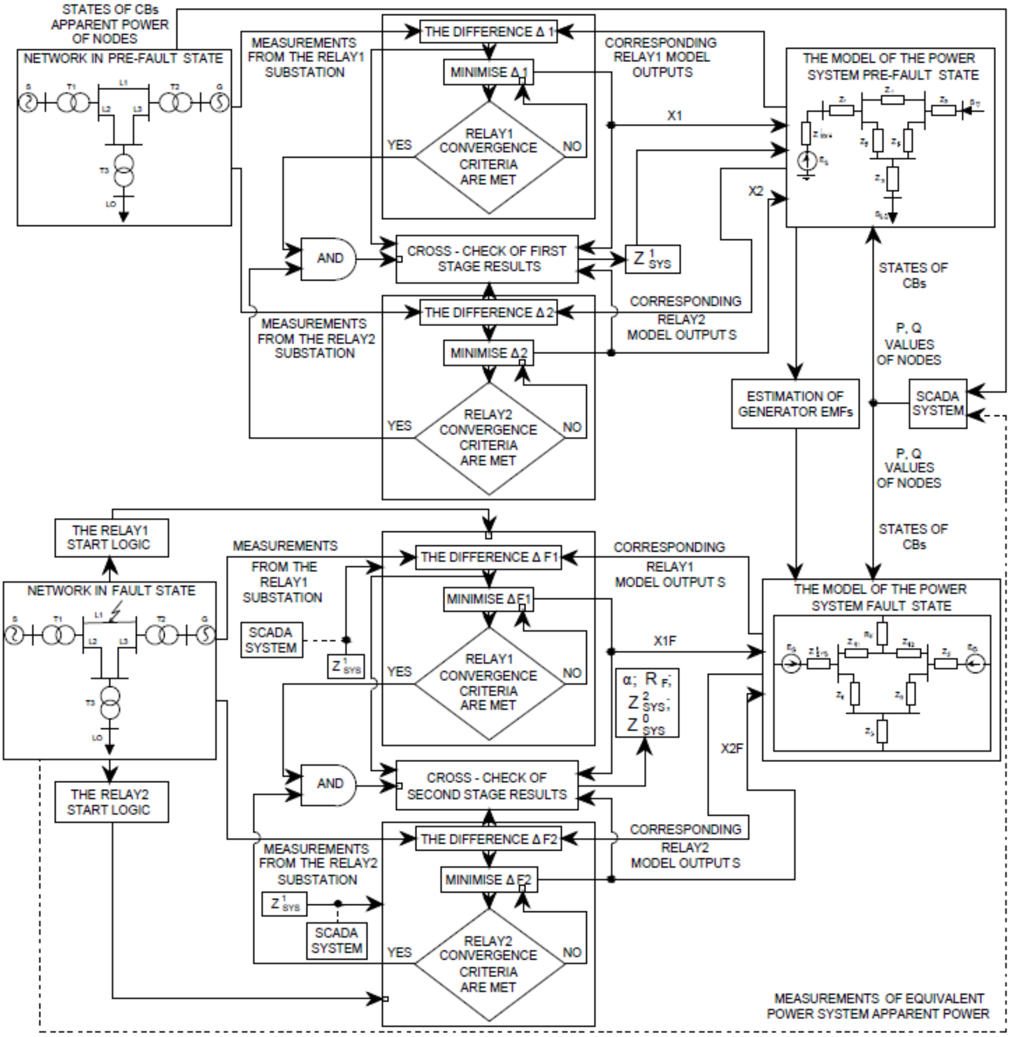

Fig. 1. The flowchart of the developed method.

When the convergence criteria of the optimisation for the second stage are met, a more rigorous cross-check is performed using the solution variants generated by FL devices at both ends of the line before selecting the most fitting solution overall. Finally, the value of α is extracted from the obtained group of decision variable values. The described framework using two stages of model parameter estimation with their respective solution cross-checks is presented as a flowchart below (Fig. 1). In the figure, X1, X2 represent decision variable vectors for the first and second “relay” terminal, respectively, which together provide a PS impedance of an equivalent power system, Z^1_{SYS}. X1F, X2F are decision variable vectors for the second (fault state) estimation stage. As can be seen in Fig. 1, an alternative version of the developed method is also considered in this study. It utilises additional measurements of apparent power flowing from an equivalent power system to its busbars for both estimation stages. The alternative version is analysed as a potential solution for rare cases where errors of estimated power system equivalent impedance might impact the overall FL accuracy and in order to see how much the additional measurement data affect the parameter estimation accuracy. However, it is still expected of the developed method to provide fault distance estimates with the aforementioned 5 % tolerance limit in all conceivable operational scenarios even without apparent power measurements added. Regardless of utilisation of the additional measurement data used for the model, updates and cross-checks do not require high-speed or synchronised communication channels between relay terminals at both ends of the faulted line. As a result, the FL in these terminals operate practically independently, except for cross-checking the obtained results.

Employing an optimisation, using measurements available from all the branches connected to a particular substation and integrating limited communication between FL devices and the SCADA system, the developed method can provide accurate fault distance estimates while avoiding dependence on the exchange of high-speed, synchronised measurement data.

2.3. The Optimisation Techniques and Cross-Checks Employed

An optimisation is utilised to determine the unknown parameters of a mathematical model by minimising the difference, Δ, between phasors obtained from measurement data and those calculated by using updated models of the considered network part. The actual objective function is calculated as the sum of squared relative errors of the real and imaginary part of each phasor separately. Thus, the optimisation task is defined as

$$\min_{f_{\mathrm{OBJ}}\in[0,\infty)} \sum_{i=1}^{N_{\mathrm{MEA}}} \left[K_{\mathrm{W}i} \cdot \left(\left(\frac{\mathrm{Re}(y_i)-\mathrm{Re}(y_{\mathrm{m}i})}{|y_i|}\right)^2 + \left(\frac{(\mathrm{Im}(y_i)-\mathrm{Im}(y_{\mathrm{m}i}))}{|y_i|}\right)^2\right)\right], \tag{3}$$

where $K_{\mathrm{W}i}$ – the weight coefficient of the i-th measured parameter; N_{MEA} – the number of measurements used for the estimation process; y_i – the phasor value of the i-th measured parameter; $y_{\mathrm{m}i}$ – the phasor of the corresponding model output of the i-th parameter.

If the modulus of a phasor obtained from measurements is $|y_i| = 0$, the relative difference is determined by using $|y_{mi}|$ as a base in (3). Optimisation as shown in (3) is applied for both estimation stages with decision variables being $|Z_{\mathrm{SYS}}^1|$; $X_{\mathrm{SYS}}^1/R_{\mathrm{SYS}}^1$ for the first stage and α; R_{F}; $|\dot{Z}_{\mathrm{SYS}}^2|$; $X_{\mathrm{SYS}}^2/R_{\mathrm{SYS}}^2$; $|\dot{Z}_{\mathrm{SYS}}^0|$; $X_{\mathrm{SYS}}^0/R_{\mathrm{SYS}}^0$ for the second stage, respectively. During the first estimation stage, the optimisation has to adhere to the following limits:

$$0.5|\dot{Z}_{\mathrm{SYS\,N}}^1| \le |\dot{Z}_{\mathrm{SYS}}^1| \le 2|\dot{Z}_{\mathrm{SYS\,N}}^1|, \tag{4}$$

$$6 \le X_{\mathrm{SYS}}^1/R_{\mathrm{SYS}}^1 \le 40 \text{ p.u.}, \tag{5}$$

$$0.8U_{\mathrm{N}j} \le |\dot{U}_j| \le 1.5U_{\mathrm{N}j},\ j = 1, \dots, N_{\mathrm{NODES}}, \tag{6}$$

and during the second stage, the limits applied are as follows:

$$0.001 \leq \alpha \leq 0.999 \text{ p.u.}, \tag{7}$$

$$0.1 \leq R_{\mathrm{F}} \leq 200\ \Omega, \tag{8}$$

$$0.5\left|\dot{Z}^{2}_{\mathrm{SYS\ N}}\right| \leq \left|\dot{Z}^{2}_{\mathrm{SYS}}\right| \leq 2\left|\dot{Z}^{2}_{\mathrm{SYS\ N}}\right|, \tag{9}$$

$$3 \leq X^{2}_{\mathrm{SYS}}/R^{2}_{\mathrm{SYS}} \leq 30 \text{ p.u.}, \tag{10}$$

$$0.5\left|\dot{Z}^{0}_{\mathrm{SYS\ N}}\right| \leq \left|\dot{Z}^{0}_{\mathrm{SYS}}\right| \leq 2\left|\dot{Z}^{0}_{\mathrm{SYS\ N}}\right|, \tag{11}$$

$$3 \leq X^{0}_{\mathrm{SYS}}/R^{0}_{\mathrm{SYS}} \leq 30 \text{ p.u.}, \tag{12}$$

where $\dot{Z}^{1}_{\mathrm{SYS\ N}}$, $\dot{Z}^{2}_{\mathrm{SYS\ N}}$ and $\dot{Z}^{0}_{\mathrm{SYS\ N}}$ – the PS, NS and ZS impedances of an equivalent power system at nominal operation conditions, Ω; $\dot{U}_j$ – the steady-state voltage calculated at node *j* of the pre-fault model, kV; $U_{\mathrm{N}j}$ – the nominal voltage at node *j* of the pre-fault model, kV; N_{NODES} – the number of nodes in the pre-fault model.

Limits (4), (9) and (11) are chosen assuming that the most notable possible changes in these impedance values, besides the loss of a link with an equivalent power system, will be due to connection or disconnection of one of two parallel elements. The loose limit (6) is adopted so that testing of the developed method may include even hardly possible post-contingency operation conditions.

Minimisation (3) is achieved with the help of a version of the genetic algorithm (GA). The GA is a versatile optimisation tool and it has been shown to be useful in similar technical tasks with several different types of GA operators and GA algorithm structures known [7], [23]–[25]. This study uses a modified version of the GA applied in [13]; therefore, only the differences introduced with these modifications will be discussed here. The most notable changes to the GA used are to be found in the convergence criteria. In addition to a base requirement of minimum generation count $minN_{\mathrm{GEN}}$ there are now three convergence criteria combinations that lead to the end of the main GA cycle. The first one remains as in [13] and requires the relative difference between the mean and minimum values of fitness or objective function *EPS* and the maximum Hamming distance to fall below certain thresholds *TH1* and *TH2* (20 % and 5 % for the first stage). The second option requires a number of stagnating generations to reach a set limit. The stagnation is recorded when the change in *EPS* between generations is smaller than *TH2* and the change in a minimum value of fitness between generations is smaller than a different stagnation upper limit. Thus, if no progress is achieved, the GA cycle is stopped to save computation time. The third group of criteria requires for the mean and minimum values of the last population fitness to be equal and lower than the minimum fitness value obtained from the initial group of solutions generated randomly before the beginning of the main GA cycle. The first estimation stage testing showed high tolerance, therefore, most of the performance balancing for it is aimed at computation time reduction as indicated by the addition of the second and third convergence criteria groups. Furthermore, the population size and the number of population members chosen via the elite selection approach [13] for this stage have been reduced to 16 and increased to 75 %, respectively. The step values for the estimation of unknown parameters are set to 0.01 Ω for $|\dot{Z}^1_{\mathrm{SYS}}|$ and 0.1 p.u. for the $X^1_{\mathrm{SYS}}/R^1_{\mathrm{SYS}}$ ratio, respectively.

Due to the accuracy observed, a relatively simple cross-check is applied for this stage to balance any unlikely errors incurred by a FL device at one of the line ends. After exchanging only the single best solution variants and the corresponding values of the objective function, each FL device calculates the value of the objective function for a solution provided by the other device. The relative total objective function (fitness) value is then calculated for each solution:

$$f_{\mathrm{OBJtotal}} = \left(f_{\mathrm{OBJ1}}/f_{\mathrm{OBJbest1}}\right) + \left(f_{\mathrm{OBJ2}}/f_{\mathrm{OBJbest2}}\right), \tag{13}$$

where f_{OBJtotal} – the relative total fitness value of a particular solution variant; f_{OBJ1} and f_{OBJ2} – the fitness values calculated by the first and second FL device using the particular solution variant; f_{OBJbest1} and f_{OBJbest2} – the fitness values for the best solutions in the last population of the GA from the first and the second FL device, respectively.

The solution variant with the lowest f_{OBJtotal} value is chosen or mean values from both solution variants are calculated if both decision variable vectors (solutions) have identical f_{OBJtotal} values.

The second estimation stage utilises the same GA version, but with more stringent settings for convergence criteria. The balancing towards higher accuracy at the expense of an additional computational burden is chosen due to the importance of correct distance estimation and other factors. The stagnating generation is registered if the change in the *EPS* between generations is lower than one-tenth of *TH2*. Additionally, here the third group of criteria is applied if the mean and minimum fitness values are less than one-tenth of the smallest fitness value calculated for the initial randomly generated solution group. The accuracy is further increased by using 20 population members and elite selection of only 50 % of new members. The maximum threshold value of the *EPS* for the first group of convergence criteria is set to 0.5 % and the maximum Hamming distance to 5 %. At the same time, the size of the initially generated group of random solutions is set to 5000 in contrast to 1000 for the first stage.

The step values used for the estimation of unknown fault-state model parameters are 0.001 p.u. and 0.1 p.u. for α and $X^2_{\mathrm{SYS}}/R^2_{\mathrm{SYS}}$, $X^0_{\mathrm{SYS}}/R^0_{\mathrm{SYS}}$ ratios, and 0.01 Ω for R_{F}, $|\dot{Z}^2_{\mathrm{SYS}}|$, $|\dot{Z}^0_{\mathrm{SYS}}|$, respectively. When the GA has converged for both FL devices, they exchange their last populations (solution groups). The maximum and minimum values for each decision variable are determined from all of these solutions. Next, a test group of solution variants is generated by combining pairs of α and R_{F} values with groups of $|\dot{Z}^2_{\mathrm{SYS}}|$, $X^2_{\mathrm{SYS}}/R^2_{\mathrm{SYS}}$, $|\dot{Z}^0_{\mathrm{SYS}}|$, $X^0_{\mathrm{SYS}}/R^0_{\mathrm{SYS}}$ values from the top 10 solutions provided by each FL device. Then, the test group is extended with a large number of randomly generated solutions within the previously determined minimum and maximum values. The resulting test group is then sent to both FL devices, which calculate their objective function values. The final solution is the one with the lowest total relative objective function value calculated according to (13).

As shown by Section 2, the developed method can be described as an optimisation-based recognition of the most likely model parameters utilising measurement data. However, in contrast to other recognition-based methods [15]–[19], the reference used is an adaptive mathematical model rather than a set of prior measurement data or simulation results. Furthermore, in contrast to OTMB methods, be they analytical [2] or probabilistic [20], the developed method models a wider extent of the neighbouring network and utilises measurements from all the branches connected to the substation. These differences together with the cross-checks introduced in the developed method reduce the risk of FL errors due to errors or insensitivity of measurements at any of the two substations.

3. THE CASE STUDY

3.1. The Case Study Power System

The power system used for studying the operation of the developed FL is presented in Fig. 2. Network sections controlled by relay terminals with the developed FL are shown in blue rectangles. Designations for the modelled OHTL faults are included as well. Detailed information about the network elements is provided in [13]. Four base scenario groups will be analysed with and without utilisation of the additional measurements of apparent power from the equivalent power system S and one scenario group, where the power system is disconnected from the analysed network.

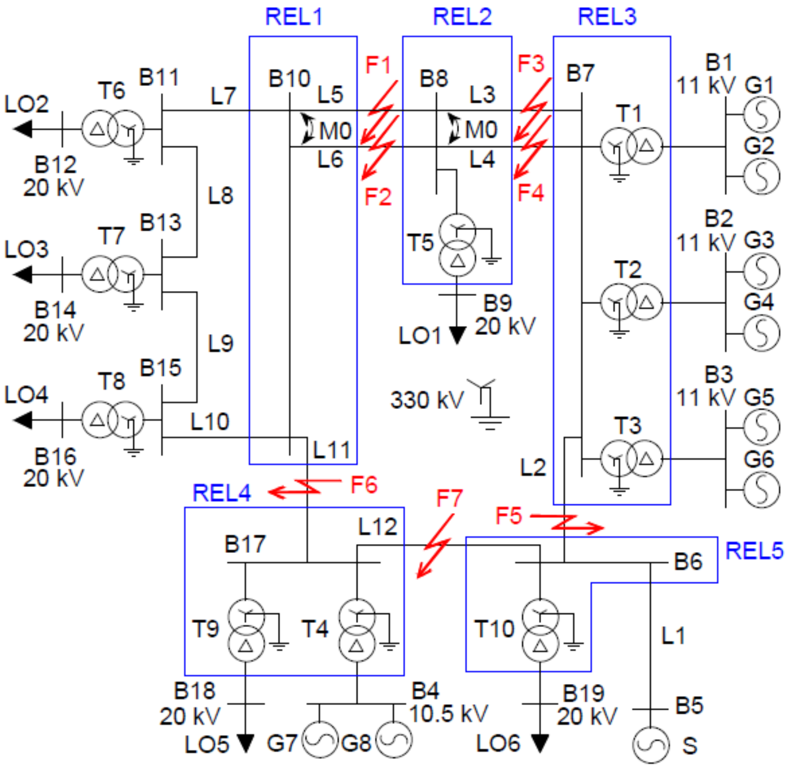

Fig. 2. The case study network.

The scenario groups consider phase-to-earth faults in an OHTL occurring while one or two other lines are out of service (Table 11). The scenario IDs consist of, first, the fault ID and then, the IDs of the lines (according to Fig. 2.) considered offline before the fault. The table also shows the maximum number of measurement phasors available for the developed FL from both ends of the line, if the additional apparent power measurements are not used.

Table 1. Scenarios Modelled in the Case Study

Scenario ID	F1L3	F6L5L6	F5L3L4	F7L2	F7L1
ID of the faulted line	L5	L11	L2	L12	L12
IDs of the disconnected lines	L3	L5 and L6	L3 and L4	L2	L1
Available measurement phasors during the pre-fault state	11	9	9	9	9
Available measurement phasors during the fault state	52	43	43	43	43

For each group of scenarios, 1000 randomised scenarios are generated. In these scenarios, the active power is randomly assigned to load and generation nodes within the limits of 0 %–120 %. The limits applied to the assignment of the reactive power are the same in case of loads but for generators it is −120 %–120 %. When generating random pre-fault and fault state scenarios, restrictions (4)–(12) are applied as well. In cases when the connection with the equivalent power system is lost and the analysed network part has a power supply deficit, the upper limits of the randomly assigned active and reactive power of loads are set so that the remaining load together with nominal network losses should constitute 99 % of the power of the remaining source capacity. After a possible pre-fault state has been obtained, α and R_F are randomly selected, and a steady-state simulation of a fault state is performed. The results of the simulations are then utilised for FL by the developed method as well as by one existing OTMB method and one TTMB method [2] for performance comparisons.

3.2. Results and Discussion

The testing results for the defined scenario groups are assembled in Table 2. The table provides both maximum and mean values of the error moduli of estimates of the equivalent power system sequence impedances (moduli and X / R ratios) for each group of scenarios. The same values are provided for the number of generations N_{GEN} necessary for the convergence of the GA during the second stage of parameter identification, as it would determine the FL computation time after a fault is cleared. For fault distance α and equivalent fault path resistance R_F, the value of two standard deviations is calculated from the moduli of the sub-scenario errors as well. Combined with the mean value, it shows the approximate upper limit of errors to be expected in 95 % of cases. "α REDI1" and "α REDI2" in Table 2 stand for the fault distances calculated by OTMB and TTMB FL algorithms implemented in an existing relay terminal [2].

The results in Table 2 demonstrate the high tolerance of the first estimation stage with only a few cases where the X^1 / R^1 ratio estimation errors approached or exceeded 10 % and show that utilisation of additional measurements would yield little improvement in accuracy for this estimation stage. The observed accuracy can be explained by a low number of decision variables and a sufficient sensitivity of measurement groups to changes in the system PS impedance values. The results for the second estimation stage show larger errors for estimates of NS and even larger ones for ZS impedances with occasional maximum errors exceeding 20 % and 50 % for $|Z^0_S|$ and X^0 / R^0. However, the mean errors of the moduli of both impedances remain within 5 % for almost all the scenario groups. Furthermore, X / R ratio estimation errors have a noteworthy impact on impedance only when an actual X / R ratio value is small due to the use of the tangent function with limited accuracy. The lower tolerance in the NS and ZS impedance estimates can be attributed to a three times larger number of decision variables compared to the first stage and a higher sensitivity of measurements to α and R_F compared to the system sequence impedances. The fact that NS impedance estimates are more accurate than ZS ones indicates the positive impact of the search space limitation introduced based on the similarities between NS and PS networks. A comparison between the results with and without utilisation of the additional power flow measurements shows the ability of these measurements to increase estimation accuracy for the system sequence impedances by offsetting the relative lack of sensitivity of the measurement sets, especially to the ZS impedance.

The results of estimating fault path resistance R_F demonstrate that this parameter can be estimated with sufficient accuracy (maximum error 1.79 % when the additional power measurements are used and 4.78 % when they are not). It can also be noted that for R_F, the use of the additional power flow measurements may result in a slightly lower estimation tolerance (F1_L3). However, for the more difficult scenario groups F6_L5_L6, F5_L3_L4 and F7_L2, the additional measurements provided an increase of the average accuracy by 34.8 %–43 %.

Table 2. Case Study Results with Errors for Obtained Parameter Estimates

		Scenario ID								
	F1_L3		F6_L5_L6		F5_L3_L4		F7_L2		F7_L1	
Additional measurements from the power system used		No	Yes	No	Yes	No	Yes	No	Yes	No
$\|Z^1_S\|$	maximum error, %	0.42	0.41	0.35	0.46	0.67	0.69	0.71	0.55	–
	mean error, %	0.022	0.021	0.023	0.024	0.022	0.027	0.029	0.032	–
X^1 / R^1	maximum error, %	8.93	7.07	9.63	7.42	6.35	9.08	8.07	11.97	–
	mean error, %	0.390	0.357	0.381	0.374	0.445	0.427	0.517	0.555	–
$\|Z^2_S\|$	maximum error, %	5.26	4.75	11.64	4.85	5.92	4.96	8.54	6.25	–
	mean error, %	0.404	0.347	0.593	0.299	0.589	0.381	0.839	0.519	–
X^2 / R^2	maximum error, %	34.56	35.00	39.73	29.17	41.50	21.83	40.37	25.92	–
	mean error, %	2.293	1.177	2.675	0.299	2.964	1.540	3.319	1.538	–
$\|Z^0_S\|$	maximum error, %	55.66	18.14	51.26	13.54	27.23	10.58	27.49	9.56	–
	mean error, %	7.237	1.506	3.088	1.073	1.739	0.971	1.368	0.957	–

X^0 / R^0	maximum error, %	86.50	42.40	83.67	46.30	68.17	40.57	68.63	39.17	–
	mean error, %	22.643	4.087	12.978	4.498	8.062	4.529	5.854	3.772	–
N_{GEN}	maximum error, %	708	845	958	915	1059	936	1111	1120	796
	mean error, %	427.4	445.0	511.8	489.0	546.9	513.3	575.8	536.4	451.0
R_F	maximum error, %	0.87	0.49	1.51	0.75	4.78	1.19	3.53	1.79	1.24
	mean error, %	0.045	0.052	0.093	0.061	0.169	0.104	0.251	0.143	0.016
	two standard deviations of error, %	0.145	0.161	0.347	0.201	0.709	0.328	0.939	0.474	0.160
α New FL	maximum error, % error, %	0.20	0.41	3.04	2.16	3.50	2.25	4.64	2.93	1.45
	mean error, %	0.030	0.043	0.212	0.159	0.240	0.174	0.469	0.278	0.031
	two standard deviations of error, %	0.078	0.123	0.687	0.472	0.799	0.542	1.517	0.811	0.199
α REDI1	maximum error, %	51.67	56.79	69.74	78.43	96.39	102.12	112.67	121.34	94.08
	mean error, %	7.475	7.784	14.848	15.14	7.182	7.440	9.743	10.290	7.837
	two standard deviations of error, %	17.15	18.04	39.11	39.29	21.36	24.47	28.38	30.10	28.49
α REDI2	maximum error, %	0.20	0.20	0.23	0.23	0.30	0.28	0.19	0.19	0.96
	mean error, %	0.087	0.088	0.103	0.103	0.120	0.121	0.077	0.077	0.431
	two standard deviations of error, %	0.102	0.101	0.115	0.114	0.165	0.147	0.108	0.110	0.491

Overall, the episodically significant errors for estimates of the PS, NS and ZS impedances of the power system and R_F did not critically affect the accuracy of the developed FL. This is shown by α estimation errors remaining within the 4.64 % margin, if additional measurements are not used, and 2.93 %, when they are. The scenario group F1_L3 indicates that for "easier" scenarios, where the measurements used are more sensitive to changes in α, extension of the measurement group with the measurements from the equivalent power system can be slightly counterproductive. However, in "difficult" scenarios, the additional measurements provided a reduction in the maximum error by 0.88 %–1.71 % of faulted line length and narrowed the range of most FL errors as shown by the drop of the error standard deviation value, which was 0.108 %–0.353 %. Data for scenario group F1_L3 in Table 1 and Table 2 indicate that after a sufficient number of available measurements is reached, a further increase of the measurement set provides little positive impact on the overall accuracy of the developed FL method, matching the observation made in the previous study [13]. Instead, the number of parallel links and the position of the faulted line within the network seem to have a higher importance.

The obtained results (Table 2) also show that the developed FL is significantly more accurate than the existing apparent-reactance-measurement-based FL (REDI1). A comparison with the existing TTMB FL (REDI2) shows that in easier scenarios (F1_L3, F7_L1), the developed FL algorithm is more accurate on average and has a smaller error dispersion as shown by the cumulative distribution functions (CDFs) obtained from scenario results (Fig. 3). However, in the more difficult scenarios, the existing TTMB method outperforms the developed method but only by 0.11 %–0.39 % of faulted line length, if the additional apparent power measurements are disregarded, and by 0.06 %–0.20 % when they are utilised.

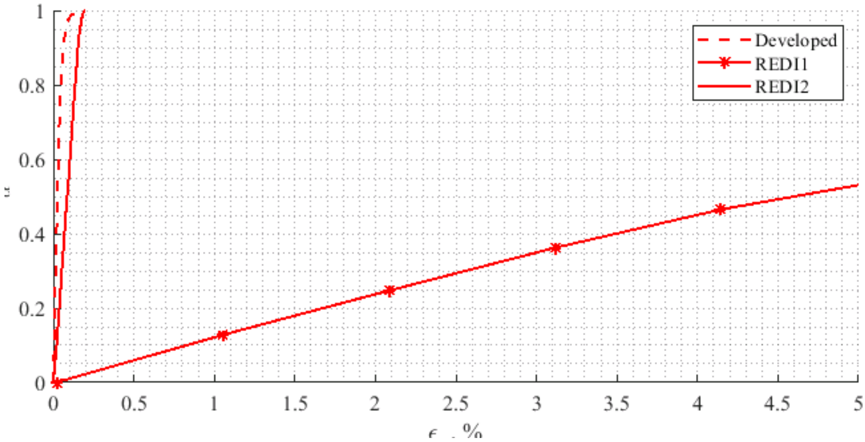

Fig. 3. The CDFs of fault distance estimate error absolute values for scenario F1_L3 without additional apparent power measurements.

4. CONCLUSIONS

The developed method ensures adaptiveness, accuracy, and robustness with a combination of several different approaches. First, models of an analysed network part are made up to date and the PS sequence impedance of an equivalent power system is estimated before fault occurrence. This reduces potential causes for errors, the number of decision variables, and the search space for the optimisation operating after a fault is cleared, thus increasing both the feasibility and accuracy of FL. The updates are performed by utilising information from a SCADA system without strict requirements for data synchronisation; limited data such as the state of CBs and power generation and demand at the main "border" nodes are fetched. Second, the utilised measurement group is extended from just the faulted line to all branches within a particular substation, which has the added benefit of reducing the potential impact of measurement errors. Third, the indirect utilisation of measurement data from the other end of the line is integrated without a data synchronisation requirement by means of result cross-checks. These allow the FL devices to operate semi-independently and to compensate for the potential lack of sensitivity of a measurement group available at one of the line ends.

The case study results show that the PS impedance of an equivalent power system can be determined with a very good tolerance, allowing the use of its estimate to define the possible interval of NS impedance values with only slightly extended margins. Estimates of the NS impedances are less accurate, but on average, their moduli are determined with a 1 % error margin. The ZS impedance estimates were the least accurate ones due to both a larger search space and a lower sensitivity of measurements to this parameter. When considering X / R ratio estimates, a similar situation is observed, but their inaccuracy often has a limited impact on the sequence impedances due to the use of the tangent function. The use of the additional power flow measurements is most useful for estimation of NS and ZS impedances as they offset the sensitivity of measurement groups towards fault distance and equivalent resistance. The episodically significant errors of estimates of system sequence impedances do not critically affect the accuracy of the developed FL, which remains within the defined 5 % limit. Utilisation of the additional apparent power measurements notably increases the accuracy of the developed FL for relatively difficult scenarios while having little effect for less problematic scenarios. A comparison with two existing FL algorithms demonstrates that developed method outperforms an existing reactance-measurement-based method. Considering simpler scenarios, it also outperforms a TTMB method in all terms but maximum error, however, in more complex scenarios the existing TTMB algorithm has a slightly higher accuracy than the developed FL method.

The future work related to the developed method could entail development and integration of universal models applicable for different fault types occurring in any of OHTLs within an analysed network part. Another research direction could be sensitivity analysis for evaluating and mitigating the impact of measurement errors or changes in the parameters of transmission lines.

ACKNOWLEDGEMENTS

The research has been funded by the Ministry of Economics of the Republic of Latvia, project “Innovative Smart Grid Technologies and their Optimization (INGRIDO)”, project No. VPP-EM-INFRA-2018/1-0006.

REFERENCES

1. Takagi, T., Yamakoshi, Y., Yamaura, M., Kondow, R., & Matsushima, T. (1982). Development of a New Type Fault Locator Using the One-Terminal Voltage and Current Data. *IEEE Transactions on Power Apparatus and Systems*, *PAS-101*(8), 2892–2898. DOI: 10.1109/TPAS.1982.317615.
2. Silarajs, M., Utans, A., Leite, L., & Sauhats, A. (2007). Multifunction relay protection device for power transmission lines LIDA. In *Proceedings of the 2nd International Conference on Electrical and Control Technologies*, (pp.120–125). 3–4 May 2007, Kaunas, Lithuania.

3. Blackburn, J.L., & Domin, T.J. (2006). *Protective Relaying Principles and Applications* (3rd ed.). New York: CRC Press.
4. Xu, Z., & Zhang, Z. (2015). What accuracy can we expect from the single-ended fault locator? In *2015 68th Annual Conference for Protective Relay Engineers*, (pp. 690–716). 30 March–2 April, 2015, Texas, USA. DOI: 10.1109/CPRE.2015.7102204.
5. Reddy, C.P., Sarma, D.V.S.S.S., & Varaprasad, O.V.S.R. (2017). A novel fault classifier and locator using one-end current spectrum and minimal synchronized symmetrical components for transmission lines. In *2016 IEEE Annual India Conference*, (pp. 1–6). 16–18 December 2016, Bangalore, Inida. DOI: 10.1109/INDICON.2016.7839128.
6. Davoudi, M.G., Sadeh, J., & Kamyab, K. (2012). Time domain fault location on transmission lines using genetic algorithm. In *2012 11th International Conference on Environment and Electrical Engineering*, (pp. 1087–1092). 18–25 May 2012, Venice, Italy. DOI: 10.1109/EEEIC.2012.6221542.
7. Ahmed, A.S., Attia, M.A., Hamed, N.M., & Abdelaziz, A.Y. (2018). Comparison between genetic algorithm and whale optimization algorithm in fault location estimation in power systems. In *2017 Nineteenth International Middle East Power Systems Conference*, (pp. 631–637). 19–21 December 2017, Cairo, Egypt. DOI: 10.1109/MEPCON.2017.8301247.
8. Pereira, C.E.M., & Zanetta, L.C. (2005). Optimization Algorithm for Fault Location in Transmission Lines Considering Current Transformer Saturation. *IEEE Transactions on Power Delivery*, *20*(2), 603–608. DOI: 10.1109/TPWRD.2004.838521.
9. Jian, Z., HongJun, Z., & JiangFeng, Q. (2012). A two-terminal fault location algorithm using asynchronous sampling based on genetic algorithm. In *2011 International Conference on Advanced Power System Automation and Protection*, (pp. 1513–1516). 16–20 October 2011, Beijing, China. DOI: 10.1109/APAP.2011.6180605.
10. Abedini, M., Hasani, A., Hajbabaie, A. H., & Khaligh, V. (2013). A new traveling wave fault location algorithm in series compensated transmission line. In *2013 21st Iranian Conference on Electrical Engineering*, (pp. 1–6). 14–16 May 2013, Mashhad, Iran. DOI: 10.1109/IranianCEE.2013.6599888.
11. Xun, L., Shungui, L., Ronghui, H., Jingwen, A., Yunzhu, A., Ping, C., & Zhengxiang, X. (2018). Study on accuracy traveling wave fault location method of overhead line–cable hybrid line and its influencing factors. In *2017 Chinese Automation Congress,* (pp. 4593–4597). 20–22 October 2017, Jinan, China. DOI: 10.1109/CAC.2017.8243590.
12. Birjadar, A., & Tajane, S. (2017). Modelling and simulation of transmission line to detect single line to ground fault location. In *2016 IEEE 1st International Conference on Power Electronics, Intelligent Control and Energy Systems*, (pp. 1–4). 4–6 July 2016, Delhi, India. DOI: 10.1109/ICPEICES.2016.7853231.
13. Zālītis, I. (2020). *Application of Estimation of Model Parameters for Protective Automation of Transmission Lines*. PhD Thesis. Riga: RTU.
14. Feng, Z., Jun, L., Li, Z., & Zhihao, Y. (2008). A new fault location method avoiding wave speed and based on traveling waves for EHV transmission line. In *2008 Third International Conference on Electric Utility Deregulation and Restructuring and Power Technologies*, (pp. 1753–1757). 6–9 April 2008, Nanjing, China. DOI: 10.1109/DRPT.2008.4523690.
15. Altaie, A.S., & Asumandu, J. (2017). Fault location using a new control technique, multiple classifier, and artificial neural network. In *2017 IEEE Texas Power and Energy Conference*, (pp. 1–6). 9–10 February 2017, Texas, USA. DOI: 10.1109/TPEC.2017.7868267.
16. Ayyagari, S.B. (2011). *Artificial Neural Network Based Fault Location for Transmission Lines*. M.S. Thesis. Lexington: UKnowledge. URL: https://uknowledge.uky.edu/gradschool_theses/657.

17. Kezunovic, M., & Knezev, M. (2008). Selection of optimal fault location algorithm. In *2008 IEEE Power and Energy Society General Meeting – Conversion and Delivery of Electrical Energy in the 21st Century*, (pp. 1–5). 20–24 July 2008, Pittsburgh, Pennsylvania. DOI: 10.1109/PES.2008.4596775.
18. Keshri, J.P., & Tiwari, H. (2017). Parameter-less fault locator using synchronized/un-synchronized data for overhead transmission line. In *2017 International Conference on Computer, Communications and Electronics*, (pp. 260–264). 1–2 July 2017, Jaipur, India. DOI: 10.1109/COMPTELIX.2017.8003975.
19. Farshad, M., & Sadeh, J. (2012). Transmission Lines Based on k-Nearest Neighbour Algorithm Using One-End Voltage. *IEEE Transactions on Power Delivery*, *27*(4), 2360–2367. DOI: 10.1109/TPWRD.2012.2211898.
20. Bockarjova, M., Dolgicers, A., & Sauhats, A. (2008). Enhancing fault location performance on power transmission lines. In 2007 IEEE Lausanne Power Tech, (pp. 1123–1128). 1–5 July 2007, Lausanne, Switzerland. DOI: 10.1109/PCT.2007.4538473.
21. Voldek, A.I., & Popov, V.V. (2007). *Electrical Machines*. *Alternating Current Machines*. St. Petersburg: Peter Press. ISBN: 978-5-469-01381-5 (in Russian).
22. Chen, C.S., Liu, C.W., & Jiang, J.A. (2006). Application of Combined Adaptive Fourier Filtering Technique and Fault Detector to Fast Distance Protection. *IEEE Transactions on Power Delivery*, *21*(2), 619–626. DOI: 10.1109/TPWRD.2005.858808.
23. Geramian, S.S., Abyane, H.A., & Mazlumi, K. (2008). Determination of optimal PMU placement for fault location using genetic algorithm. In *2008 13th International Conference on Harmonics and Quality of Power*, (pp. 1–5). 28 September–1 October 2008. DOI: 10.1109/ICHQP.2008.4668810.
24. He, L., Jia, K., & Fan, Z. (2010). The immune genetic algorithm in fault diagnosis of modern power system. In *2010 2nd International Conference on Education Technology and Computer,* (pp. 26–29). 22–24 June 2010, Shanghai, China. DOI: 10.1109/ICETC.2010.5529742.
25. Cruz, H.O., & Leão, F.B. (2018). Optimal placement of fault indicators using adaptive genetic algorithm. In *2017 IEEE Power & Energy Society General Meeting*, (pp. 1–5). 16–20 July 2017, Chicago, Illinois, USA. DOI: 10.1109/PESGM.2017.8273897.

LATVIAN JOURNAL OF PHYSICS
AND TECHNICAL SCIENCES
2023, N 4

DOI: 10.2478/lpts-2023-0022

R&D OF A HYDRAULIC HYDROGEN COMPRESSION SYSTEM FOR REFUELLING STATIONS

V. Bezrukovs[1], Vl. Bezrukovs[1,2], M. Konuhova[1],
D. Bezrukovs[1], I. Kaldre[3], A. Berzins[1]

[1] Engineering Research Institute "Ventspils International Radio Astronomy Centre" (ERI VIRAC) of Ventspils University of Applied Sciences,
101 A Inzenieru Str., Ventspils, LV-3601, LATVIA
[2] Ventspils University of Applied Sciences Development Fund,
101 A Inzenieru Str., Ventspils, LV-3601, LATVIA
[3] Faculty of Physics, Mathematics and Optometry, University of Latvia,
25 Zellu Str., Riga, LV-1002, LATVIA

The article presents a hydraulic hydrogen compression solution designed to serve as a booster compressor. It can be adapted to changing parameters of the inlet pressure of hydrogen and allows stabilising the hydrogen accumulation process in the high-pressure storage.

The main results of this study were obtained using a numerical model developed to explore the thermodynamic processes that occur during the hydraulic compression of hydrogen. The modelling was carried out using COMSOL Multiphysics® 6.0 software with the CFD and heat transfer modules. The compression chamber in the form of a cylinder with a volume of 1.14 *l* and wall thickness of 5 mm was used in the computational model. The aim of these simulations was to investigate the temperature change limits of hydrogen, cylinder walls and working fluid, as well as to estimate the actual value of pressure inside the cylinder. The considered process of pressure increase in the cylinder chamber was modelled as a continuous change of volume filled with working fluid with discrete time step of 0.01 *s*, taking into account the increase of temperature inside the cylinder. The derived modelling results for different durations of compression stroke t_s from 0.5 to 20.0 *s* were presented. The curves of energy consumption and temperature rise during the compression process were calculated for initial hydrogen pressures P_1 = 3.0, 10.0, 15.0 and 20.0 *MPa* and compression ratio K_c = 5.0.

The results of simulation of thermodynamic processes and their analysis allowed estimating energy consumption in the system of hydraulic compression and determining conditions which would lead to the increase in efficiency of hydrogen compression operation systems under consideration.

Keywords: *Heat transfer, high pressure, hydrogen, hydraulic compressors, numerical simulations, refuelling stations.*

1. INTRODUCTION

A growing number of countries and companies are engaged in intense competition for leadership in clean hydrogen technologies. Today, more than 30 countries have developed or are preparing hydrogen strategies, indicating growing interest in developing hydrogen value chains [1]. It is apparent that hydrogen has the potential to make a significant contribution to three of the most important tasks concerning energy use: sustainable economic development of the European Union, reducing greenhouse gas emissions and curbing air pollution [2], [3].

In recent years, the use of hydrogen energy in transport and the concept of a hydrogen economy have benefited from a fresh wave of strong political support. At the same time, rapidly evolving technologies have raised the possibility of using hydrogen as a driver for a future carbon-neutral energy system. At the heart of this initiative, there is the desire for energy security and independence. The European Union has set an ambitious goal to become the first climate neutral continent by 2050, which is in line with the guidelines of the European Commission [4].

Depending on the production method, hydrogen is conventionally labelled green, blue, pink and grey, and specialised terms like – safe, sustainable, low-carbon and pure – are also used [5]. Utilisation of the renewable energy sources, which are practically inexhaustible, for hydrogen generation allows establishing continuous, sustainable, ecologically clean energy production cycle. Thus, "green" hydrogen is one of the most promising approaches for future energy storage infrastructure development projects.

Green hydrogen is considered to be one of the most environmentally friendly energy carriers and will be an important part of the future 100% sustainable energy system [6].

In the production of green hydrogen, the main emphasis is on the use of wind and solar energy. Current level of technological processes ensures the production of hydrogen by electrolysis of water without emission of carbon dioxide into the atmosphere. Thus, the entire process of water electrolysis and hydrogen generation can potentially be carbon free if renewable or nuclear electricity is used [7], [8].

On the consumption side, the conversion of hydrogen energy into electric current bypassing combustion process makes it possible to use this energy source to power electric vehicles. Currently, there are plenty of examples of successful implementation of hydrogen technology for cars and trucks [9], [10].

A schematic diagram of a refuelling station using hydrogen at inlet pressure from 0.6 up to 25.0 *MPa*, either brought by trailer or generated by electrolysis at the station itself, is shown in Fig. 1. The proposed concept is especially attractive when combined with the use of green hydrogen produced by electrolysis, fed from wind turbines, solar panels or the electricity grid [11]. Using the booster hydraulic compressor, the low-pressure hydrogen is raised to the required 70.0 *MPa* for cars and 35.0 *MPa* for trucks and pumped into the storage tanks. The high-pressure hydrogen is then filled into the vehicle fuel tanks via a dispenser.

In articles [8], [12] currently existing technologies of hydrogen compression, their working principles, advantages and limitations are reviewed and discussed. It should be noted that, from a wide variety of compressors, the compressors with a liquid piston have the lowest energy consumption, as only this technology is able to provide a quasi-isothermal compression process.

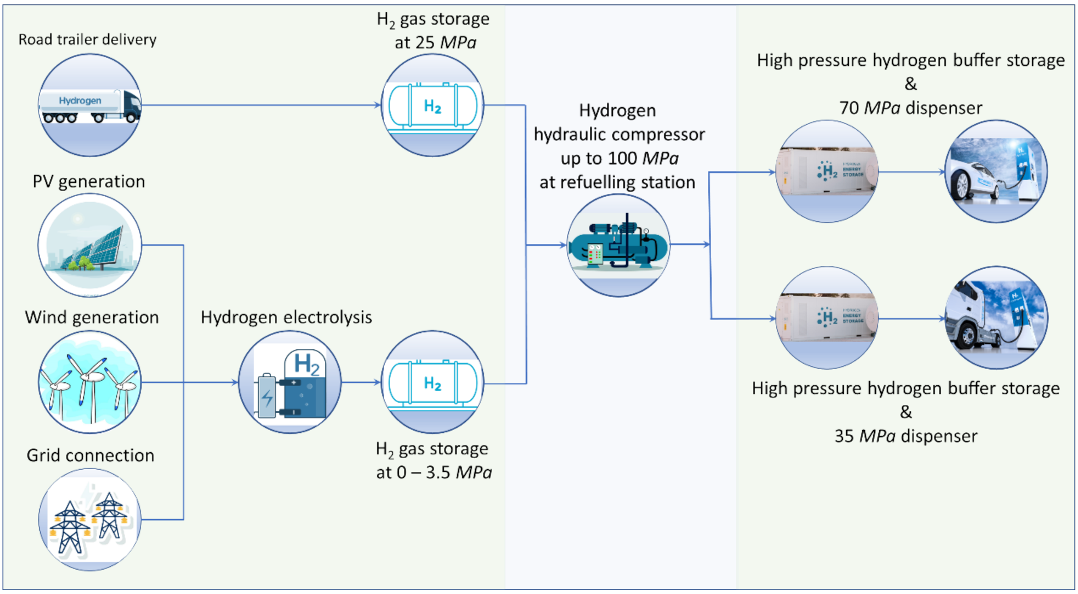

Fig. 1. Schematic diagram of the delivery, storage and preparation of compressed high-pressure hydrogen for use at refuelling stations.

The liquid piston is not a new concept, as the earliest known application dates back to 1906. This solution was used in an internal combustion engine for pumping water, known as the Humphrey pump [13]. The Humphrey pump followed the Atkinson cycle and demonstrated efficiencies of between 5 % and 10 % [14].

The liquid piston gas compression concept uses a column of liquid to directly compress gas in a fixed volume chamber. The use of a liquid piston eliminates gas leakage from the compression chamber and eliminates the friction of the mechanical sliding seals present in the cylinders of mechanical compressors and allows increasing the efficiency of gas compression. Using a simplified model, it has been demonstrated that this concept can increase the compression efficiency from 70 % to over 83 % [15].

It should be noted that the gas compression process is accompanied by high heat generation and the temperature of the gas has an effect on the working fluid. In fact, the fluid and the gas are compressed together, but since the fluid has a higher density and a higher heat capacity, the heat generated during compression is effectively absorbed by the fluid and the surrounding walls of the compression chamber.

Once the compression stroke is complete, the heated fluid is channelled from the compression chamber into the heat exchanger, where it is cooled. As a result, hydraulic compressors have an advantage over reciprocating compressors in terms of cooling, as there is no need for external heat exchangers on the compression chambers. This reduces the weight of the compressor and the cost of the entire system [8].

Nowadays, when deploying hydrogen infrastructure for vehicle refuelling, it is essential to take advantage of simple and affordable devices for hydrogen compression tasks.

Research performed by the authors in this direction has led to the development of a number of technical solutions [16]–[18] which are aimed at increasing the efficiency of hydrogen hydraulic compression systems.

The study of thermodynamic processes in the hydrogen hydraulic compression system performed by the means of numerical simulation and analysis of the results allow estimating energy consumption and determining conditions which would lead to the increase in the efficiency of operation of the considered hydrogen hydraulic compression system.

2. SIMULATION OF THE HYDRAULIC COMPRESSION PROCESS

The process of hydraulic gas compression can be represented by simplified diagrams in Fig. 2. Figure 2a shows the state of the system at the beginning of the process when gas with pressure $P_1 = 3.0\ MPa$ from the low-pressure tank through open valves fills the compression chamber with volume V_1 and the high-pressure storage with volume V_2. The compressor is then filled with working fluid via flow rate meter *S*, causing the gas to be compressed to volume V_3 with pressure P_3. Once the compression process is complete, the compressed hydrogen is injected through the open valve to the high-pressure storage.

To estimate the rate of pressure rise in high-pressure storage, with some assumptions, one can use relations derived from Boyle-Marriott's law. In this case, we assume that in the physical system under consideration the gas temperature at the beginning and at the end of the compression process remains constant.

Figure 2b shows the state of the system at the end of the compression process, when the high-pressure storage is filled with gas up to a target pressure $P_c = 15.0\ MPa$.

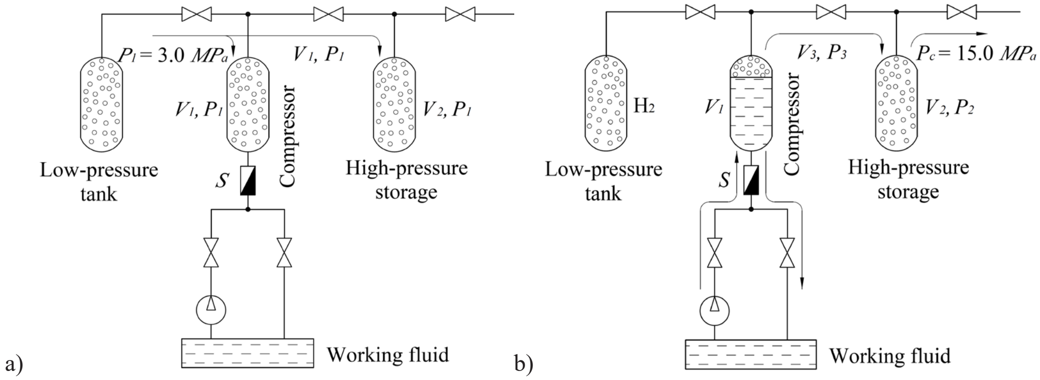

Fig. 2a. A simplified scheme of the hydrogen hydraulic compression system at the start and *2b* – at the end of the compression process, where the compressor, using a working fluid, compresses hydrogen to volume V_3 with pressure P_3.

During the cyclical repetition of the compression process the pressure in high-pressure storage increases stepwise. Thus, gas pressure P_{2i} originating at the end of each compression stroke *i* after opening of the valve and combining gas volumes V_2 and V_3 with corresponding pressure values P_2, P_3, is determined by the following relations:

$$P_{2i} = \frac{P_3 V_3 + P_{2(i-1)} V_2}{V_3 + V_2}\ , \qquad (1)$$

where

$$P_3 = \frac{P_1 V_1}{V_3} = const. \qquad (2)$$

In Eq. (2), the ratio of volumes corresponds to the compression ratio of hydrogen in compressor and can be expressed as follows:

$$K_c = \frac{V_1}{V_3}. \tag{3}$$

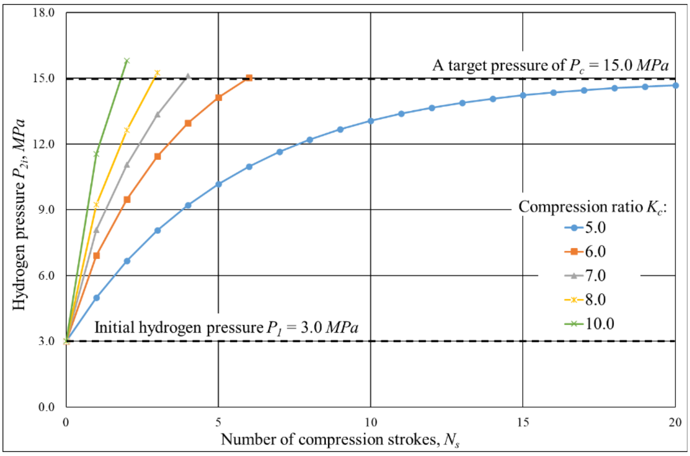

Fig. 3. Increase of cumulative hydrogen pressure P_{2i} in the high-pressure storage V_2 for corresponding number of strokes N_s at inlet hydrogen pressure P_1 = 3.0 *MPa*, for different compression ratios K_c = 5.0, 6.0, 7.0, 8.0 and 10.0.

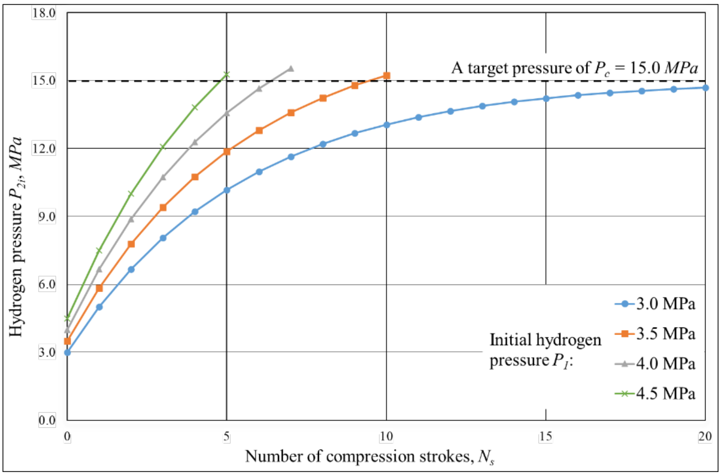

Fig. 4. Increase of cumulative hydrogen pressure P_{2i} in the high-pressure storage V_2, for hydrogen inlet pressure P_1, varying from 3.0 to 4.5 *MPa* at a constant compression ratio K_c = 5.0 for corresponding number of strokes N_s.

The results of the calculations of pressure change P_{2i} in high-pressure storage after every compression stroke $i = 1, 2, 3\ldots N_s$ for compression ratios K_c = 5.0, 6.0, 7.0, 8.0, 10.0 are shown as curves in Fig. 3, where it is seen that the curves have an exponential dependence and pressure growth rate in high-pressure storage decreases with every compression stroke.

As can be seen on the curves of Fig. 3, at high values of compression ratio K_c, the number of compression strokes N_s required for achieving the target pressure in the high-pressure storage (P_c = 15.0 *MPa*) decreases.

For example, an increase of compression ratio K_c from 5.0 to 6.0 leads to an increase of pressure P_3 by 20 %, but the number of compression strokes N_s decreases from 21 to 7. However, in real conditions, the increase of the compression ratio K_c is limited by technical characteristics of liquid pump, valves and fittings used in the system design.

The acceleration of the compression process can also be achieved by increasing the inlet pressure P_1 in the system. Figure 4 shows an example of how a change in inlet pressure P_1 (varying from 3.0 to 4.5 *MPa*) at a constant compression ratio K_c = 5.0 affects the number of strokes required to achieve a target pressure of P_c = 15.0 *MPa*.

3. DESIGN OF THE HYDRAULIC COMPRESSION SYSTEM

The device proposed in Fig. 5 is designed for use as a booster compressor in a refuelling station system that uses hydrogen brought in by truck in tubes with a pressure of up to 25.0 *MPa* or produced locally by electrolysis of water in limited quantities with a pressure of up to 4.5 *MPa*. For example, an Enapter electrolyser can produce up to 500 *l/h* or 1.0785 *kg/h* H_2 at 20 °C and 3.5 *MPa* [19]. For the production of “green” hydrogen, wind and solar energy can be used, converted into electrical power utilising, for example, wind turbines and photovoltaic panels.

The proposed device operates on the principle of hydraulic compression of hydrogen in closed chambers filled with a working fluid suitable for the compression of hydrogen. The cycling of the processes of compression and filling with a new portion of low-pressure hydrogen occurs in accordance with a certain valve switching algorithm. All valves in the device circuit are controllable and connected to the control unit, which is not shown in the diagram.

The operation algorithm provides for the joint operation of all stages of hydrogen compression, and this leads to a gradual increase in pressure of hydrogen in the high-pressure storage C_4. In the first embodiment of the device in the initial state, the tank T_1 is filled with hydrogen obtained from the source with an initial pressure, and working fluid F is poured into the reservoir T_2.

At the same time, after switching on the control unit, the controlled valves S_1 - S_5, S_6, S_{16}, S_{17} in the device are opened, the valve S_{15} closed, and the hydraulic pump K_1 does not create pressure in the pipelines. In the meantime, the compression chambers C_1, C_2, C_3, the high-pressure storage C_4 and the buffer storage C_5 are filled with the hydrogen from the tank T_1 with the corresponding pressure. After that the valves S_1 - S_5, S_6, S_7, S_{17} are closing.

The next step is to switch on the hydraulic pump K_1 and open the valve S_{10} through which the working fluid F from the reservoir T_2 is supplied to the compression chamber C_2 of the first compression stage through the pipeline and through the flow meter L_2. Filling the compression chamber of the first compression stage with working fluid F leads to a decrease in the volume of hydrogen, and its pressure increases proportionally.

The amount of working fluid F entering the compression chamber C_2 is measured by the flow meter L_2. When the predetermined degree of hydrogen compression in the compression chamber C_2 is reached, the valve S_{10} is closed and the valve S_5 is opened.

Through the valve S_5, compressed

hydrogen enters the compression chamber C_3 of the second compression stage and simultaneously through the valve S_8 and the flow meter L_1, working fluid F enters the compression chamber C_1, where hydrogen is compressed. At the same time, the transfer of compressed hydrogen from the compression chamber C_2 to the chamber C_3 of the second compression stage is completed, and then the valve S_5 is closed.

Further, the valve S_3 and the valve S_{13} are opened, as a result of which hydrogen from the tank T_1 through the open valve S_1 extrudes working fluid *F* from the compression chamber C_2 into the reservoir T_2 through the flow meter L_2 and the optical sensor L_6 to control the fluid flow. The direction of the fluid flow through the flow meter L_2 changes the direction; therefore, the said flow meter L_2 operates in the reverse counting mode and issues a signal to close the valve S_3, when the measured volumes of fluid pumped in one and the other direction are equalised.

In this state, the chamber C_2 is filled with hydrogen and prepared for a new compression cycle, and hydrogen in the chamber C_1 is in a compressed state. At this moment, valve S_4 is opened, and compressed hydrogen from the chamber C_1 enters the chamber C_3. An additional volume of compressed hydrogen from the chamber C_1 increases the level of hydrogen pressure in the chamber C_3, after which the valve S_4 is closed. At the same time, the valve S_{10} is opened, and the chamber C_2 is filled with fluid *F*, which leads to the compression of a new portion of hydrogen.

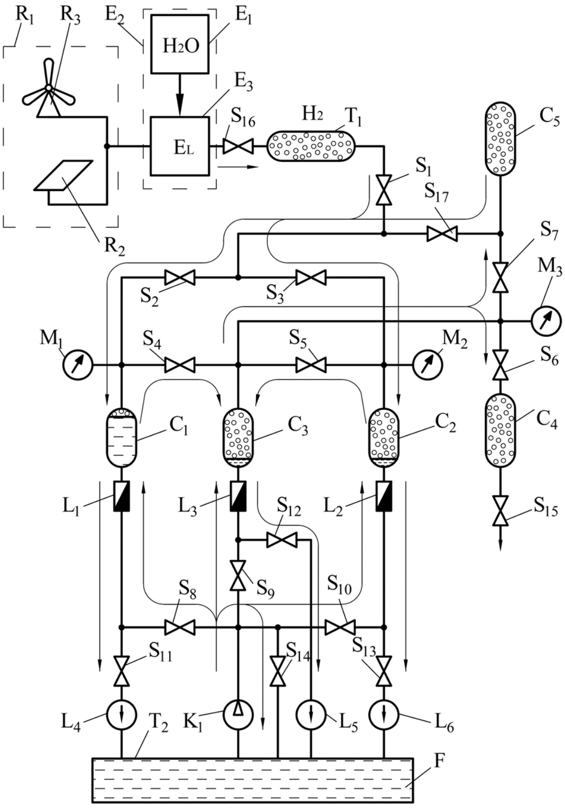

Fig. 5. Schematic view of a hydraulic hydrogen compression system for refuelling stations, using flow rate meters and an additional booster storage for raising the pressure in the high-pressure storage.

After closing the S_4 valve, the valve S_2 and the valve S_{11} are opened, and hydrogen from the tank T_1 extrudes fluid F from the first chamber C_1 into the reservoir T_2 through the flow meter L_1 and the optical sensor L_4. The flow meter L_1 also operates in reverse counting mode and issues a signal to close the valve S_2 and S_{11}, when the measured volumes of fluid pumped in one and the other direction are equalised.

Hydrogen pressure in the chamber C_3 through several repeated cycles reaches its maximum and becomes equal to pressure in the chamber C_1 and C_2. After that, the valves S_4 and S_5 of the second group are closed, and the valve S_9 is opened, through which fluid F is supplied to the chamber C_3.

After the completion of the hydrogen compression cycle in the chamber C_3, the valve S_9 is closed, and the valves S_6, S_7 are opened. Compressed hydrogen enters the high-pressure storage C_4 and the buffer storage C_5.

After the removal of the compressed hydrogen from the chamber C_3, the valves S_6, S_7 are closed and the valve S_{12} is opened, as a result of which fluid F flows through the flow meter L_3 and the optical sensor L_5. The flow meter L_3 also operates in reverse counting mode and issues a signal to close the valve S_{12}, when the measured volumes of fluid pumped in one and

the other direction are equalised. Thus, the process of accumulation of high-pressure hydrogen in the high-pressure storage C_4 and in the buffer storage C_5 is completed.

Optical sensors of fluid flow control L_4 - L_6 duplicate operation of fluid flow meters L_1 - L_3 to exclude ingress of hydrogen into the reservoir T_2 in the case of rupture of fluid flow F.

In the process of cyclic switching of valves, a situation may arise when valves S_8 - S_{10} of the fourth group can simultaneously receive a command to close, since the control of these processes depends on signals from the output of flow meters L_1 - L_3 and optical sensors L_4 - L_6. As a result, simultaneous closing of valves S_8 - S_{10} is possible, which will lead to a sharp increase in pressure at the outlet of the high-pressure hydraulic pump K_1. Switching on the safety valve S_{14} serves to bypass the fluid flow F from the outlet of the hydraulic pump K_1 and reduces the pressure in the pipelines in this case.

Limited hydrogen reserves in the tank T_1 lead to a decrease in the hydrogen inlet pressure during the operation of the device, which is supplied to the chambers C_1 and C_2. This raises the question how to maintain the high pressure of the hydrogen that fills the high-pressure storage C_4 when the pressure in tank T_1 is low. To compensate this effect, the device provides the ability to refill chambers C_1 and C_2 of the first compression stage with hydrogen accumulated in the buffer storage C_5. In this case, after hydrogen is compressed in the chambers C_1, C_2 and after that in chamber C_3, hydrogen is supplied only to the high-pressure storage C_4 through the valve S.

This feature also makes it possible to maintain a high pressure in the high-pressure storage C_4 during the intermittent supply of hydrogen produced by the electrolyser E_2 from renewable energy sources such as the wind turbine R_3 or the photovoltaic panel R_2. In this way, the operation of the device can be adapted to varying pressure settings at the inlet of the T_1 tank, thus accelerating the refuelling speed of the vehicles.

4. THE NUMERICAL MODEL OF HYDROGEN HYDRAULIC COMPRESSION

An increase in pressure in the closed chambers of the hydrogen hydraulic compression device leads to an increase in the temperature of the compressed gas and working fluid. This effect must be respected in order to assess the possible influence of temperature on the properties of the working fluid and to determine the energy consumption for the compression process.

The thermodynamic processes associated with hydrogen compression were investigated using COMSOL Multiphysics® 6.0 software with the CFD and heat transfer modules. The compression chamber used in the calculation model is a cylinder shown in Fig. 6, with height h = 145 *mm*, an inner diameter d = 100 *mm* with a volume of *l*, the chamber walls are made of stainless-steel with thickness of 5 *mm*.

In the numerical model, the thermodynamic process is implemented, which takes into account heat exchange between the gas, working fluid and the cylinder walls and the model also reflects the process of convective heat transfer into the surrounding space.

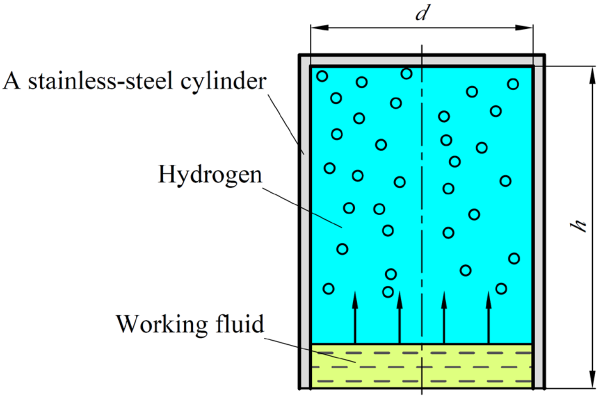

Fig 6. A model of a steel cylinder shaped chamber where hydrogen is compressed by the working fluid coming from below in the direction of the arrow.

The aim of the simulation is to investigate the temperature change limits of hydrogen, cylinder walls and working fluid, as well as to estimate the actual pressure inside the cylinder. The process of increasing pressure in the cylinder chamber is considered as a result of discrete changes of volume, which is filled with working fluid, taking into account the increase of gas temperature.

Each step of the discrete volume change increases the height of the fluid by a certain amount, determined by a given stroke time t_s and a given compression ratio K_c. In this case, we assume that at each time step of hydraulic compression of hydrogen in the model, properties of working fluid and gas are uniformly distributed. Time of discrete change of working fluid volume used in calculations is constant and set equal to Δt_s = 0.01 *s*.

The physical properties of hydrogen, working fluid and stainless-steel cylinder used in the model are shown in Table 1.

Table 1. Initial Parameters and Physical Properties of Hydrogen, Liquid Piston and Cylinder Used in the Model

Initial parameters used in the simulation	Temperature of gas, working fluid, cylinder and surrounding air $Ti = 300.0\ K$ Pressure $P_1 = 3.0\ MPa$ Volume $V = 1.14$ *litres* Gas mass in the cylinder = 2.74 *g* Cylinder – air heat transfer coefficient h = 20.0 $W/(K\cdot m^2)$ The mass of the cylinder is – 2400 g Wall thickness of the cylinder – 5 *mm* The calculations use a compressible liquid with a Mach number < 0.3		
	Property and its variable used in COMSOL	*Value*	*Unit*
Properties of hydrogen	Molar mass (*M*)	2.016	*g/mol*
	Degrees of freedom (*f*)	5.0	
	Ratio of specific heat (*γ*)	1.4	
	Heat capacity at constant volume (*cv*)	10307.5	*J/kg·K*
	Heat capacity at constant pressure (*cp*)	14429.6	*J/kg·K*
Properties of the liquid piston	Thermal conductivity (*k_iso*)	0.4	*W/(m·K)*
	Density (*rho*)	918.0	kg/m^3
	Heat capacity at constant pressure (*cp*)	2060.0	*J/(kg·K)*
	Dynamic viscosity (*mu*)	130.6	*Pa·s*
	Ratio of specific heats (*gamma*)	1.0	
Properties of the stainless-steel cylinder	Thermal conductivity (*k_iso*)	45.0	*W/(m·K)*
	Density (*rho*)	7700.0	kg/m^3
	Heat capacity at constant pressure (*cp*)	800.0	*J/(kg·K)*

The volume of working fluid V_{Fj} in the compression chamber after each step is determined by the expression:

$$V_{Fj} = \Delta V_F\, j, \tag{4}$$

$$\Delta V_F = \frac{V\left(1 - \frac{1}{K_c}\right)}{t_s} \Delta t_s, \tag{5}$$

where V – entire volume of the compression chamber;
ΔV_F – the value of the discrete increase in volume of the working fluid;
$j = 1, 2, 3 \ldots n$ – the number of the step of the discrete increase of the working fluid volume;
$n = t_s / \Delta t_s$ – count of steps in the one compression stroke.

The developed numerical model of gas compression considering thermal losses has been successfully implemented and tested in the COMSOL Multiphysics® 6.0 software environment. The calculation results were analysed and compared with the calculations based on the analytical model and the results of the adiabatic model.

Thus, the use of numerical simulations made it possible to investigate and study the thermodynamic processes occurring in the cylinder of the device during hydraulic compression of hydrogen with varying degrees of initial pressure.

5. THERMODYNAMIC MODELLING OF THE HYDROGEN COMPRESSION PROCESS

The investigation of different modes of hydrogen compression depending on the of compression process t_s, initial hydrogen pressure P_1 and compression ratio K_c allow estimating the influence of these parameters on temperature change inside the cylinder and the value of energy consumption which is spent for the execution of a compression cycle.

Figures 7 and 8 show temperature distribution models derived from numerical simulations for fluid and gas confined inside the cylinder body for a single 20-second stroke ($t_s = 20\ s$) for time intervals: 0, 10, 15 and 20 *s*. For better representation of material temperatures with respect to their different heating levels, colour palettes with scale corresponding to the limits of 300–305 *K* for working fluid and 300–550 *K* for gas are used. Initial temperature of hydrogen, working fluid and compression cylinder body is $T_i = 300\ K$, initial gas pressure $P_1 = 3.0\ MPa$, compression coefficient $K_c = 5.0$.

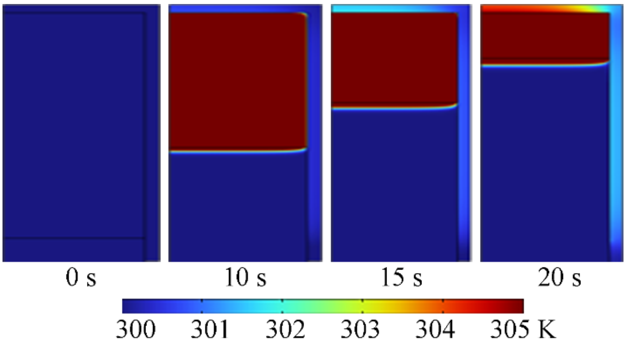

Fig. 7. Distribution of the temperature of working fluid and steel of the compression cylinder during a single 20-second compression stroke. The average fluid temperature rises by $\Delta T_F = 1.52\ K$, at initial pressure $P_1 = 3.0\ MPa$ and compression ratio $K_c = 5.0$.

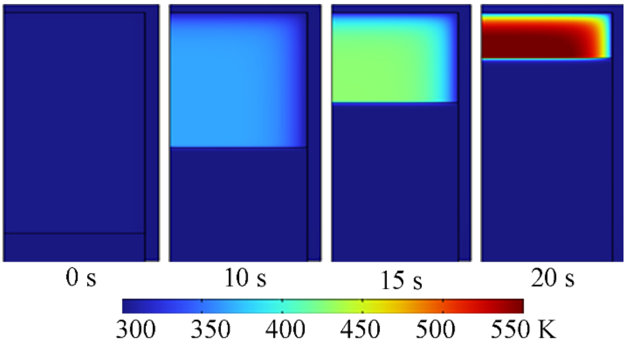

Fig. 8. Distribution of the temperature of hydrogen in the compression cylinder during a single 20-second compression stroke. The average gas temperature rises by $\Delta T_H = 188.6\ K$, at initial pressure $P_1 = 3.0\ MPa$ and compression ratio $K_c = 5.0$.

In this study, the superposition method is used, and it is assumed that the compression process takes place without mixing of media, which on the figures are separated by a symbolic black line. Heat exchange between hydrogen, working fluid and vessel takes place only as a result of thermal conductivity of these materials. For the considered example, calculations show that the integral temperatures of gas and working fluid at the end of the compression process increase accordingly by $\Delta T_H = 1.52$ *K* and $\Delta T_F = 188.6$ *K*.

The results of the simulation of the compression process make it possible to estimate the temperature rise in the gas and working fluid and consequently to determine the energy that is expended performing the hydraulic compression process. In this context, it is of interest to consider the changes that occur in the compression process when varying duration of the compression stroke t_s and initial pressures of hydrogen P_1. Figures 9–11 show how average temperatures of hydrogen ΔT_H, working fluid ΔT_F and steel cylinder ΔT_C change during a single compression stroke, the time t_s of which ranges from 0.5 to 20.0 *s* depending on initial pressure P_1 = 3.0, 10.0, 15.0 and 20.0 *MPa*.

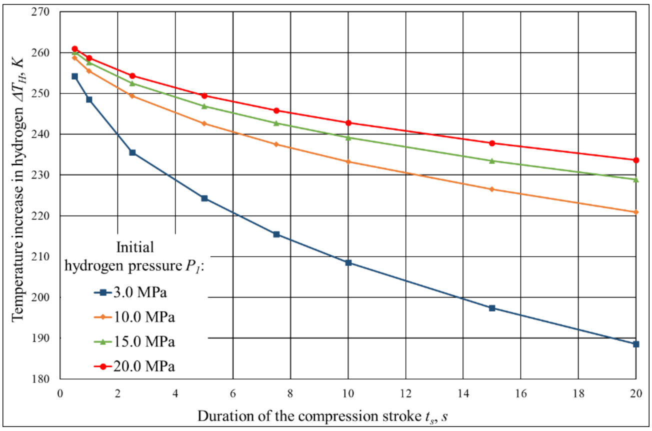

Fig. 9. Average temperature increase in hydrogen ΔT_H for different durations of the compression stroke t_s, at initial pressures P_1 = 3.0, 10.0, 15.0 and 20.0 *MPa* and compression ratio K_c = 5.0.

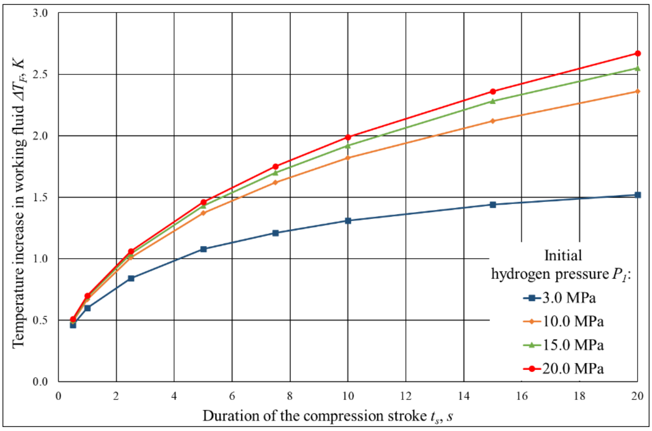

Fig. 10. Average temperature increase in working fluid ΔT_F for different durations of the compression stroke t_s, at initial pressures P_1 = 3.0, 10.0, 15.0 and 20.0 *MPa* and compression ratio K_c = 5.0.

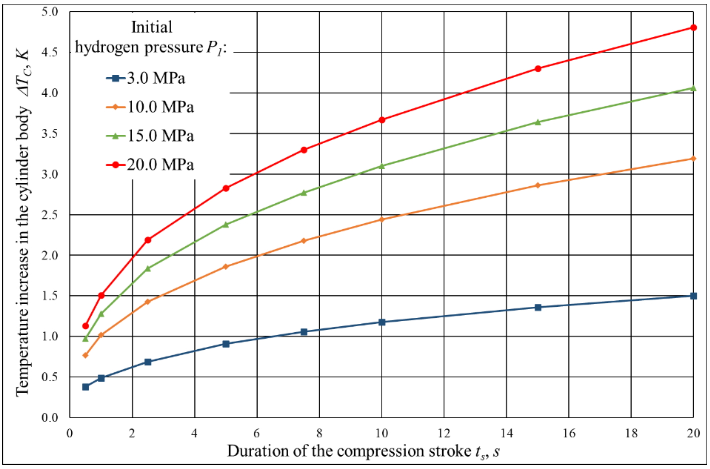

Fig. 11. Average temperature increase in the cylinder body ΔT_C for different durations of the compression stroke t_s, at initial pressures P_1 = 3.0, 10.0, 15.0 and 20.0 *MPa* and compression ratio K_c = 5.0.

The increase in temperature values, previously determined in the model, corresponds to the energy involved in the process of hydraulic compression of hydrogen and accumulated in hydrogen volume, working fluid and cylinder body. The amount of energy deposited in the compressed hydrogen, working fluid and in the stainless-steel walls of the cylinder is determined by an equation according to the laws of thermodynamics:

$$Q = m\, c\, \Delta T, \tag{6}$$

where m – the mass, *kg*;
c – heat capacity, *J/Kg*K*;
ΔT – the integral temperature increase in the medium at the end of the compression stroke, *K*.

The heat capacity values for hydrogen, working fluid and stainless-steel cylinder are provided in Table 1. The model takes into account the change in mass of hydrogen with increasing initial pressure.

In order to estimate the total energy Q_T required to compress hydrogen, at different duration of compression stroke t_s, at initial pressures P_1 = 3.0, 10.0, 15.0, 20.0 *MPa*, the graphs shown in Fig. 12 have been constructed. As can be seen, the curves of energy consumption for hydrogen compression are slightly dependent on the rate of filling of the cylinder volume with working fluid. The energy consumption tends to stabilise as the stroke time increases.

To estimate the dynamic changes of energy consumption as a function of the stroke duration, calculations are shown in relative units where the whole compression cycle is taken as 100 %. Figure 13 shows the energy consumption during compression for stroke durations t_s = 2.5, 5.0 and 10.0 *s*. In this model, initial pressure P_1 = 3.0 *MPa* and the compression ratio K_c = 5.0.

The modelling of the compression process with the use of a superposition method allows representing temperature and volumes of energy separately for each medium. Thus, the distribution of the amount of energy Q_T, which is spent for compression process without taking into account losses on convection, between working fluid Q_F, hydrogen Q_H and steel of cylinder body Q_C depending on duration of compression cycle t_s can be presented in the form of a graph shown in Fig. 14. The structure of energy distribution for initial pressures P_1 = 3.0 and 20.0 *MPa* and the compression ratio K_c= 5.0 shows that most of the energy is concentrated in hydrogen.

In real conditions, hydrogen and working fluid inside the cylinder are constantly being mixed and exchanging energy. In this case, it is fair to assume that once hydrogen and working fluid are mixed, the temperature of the medium inside the compression chamber averages out, cooling the gas and increasing the temperature of the working fluid.

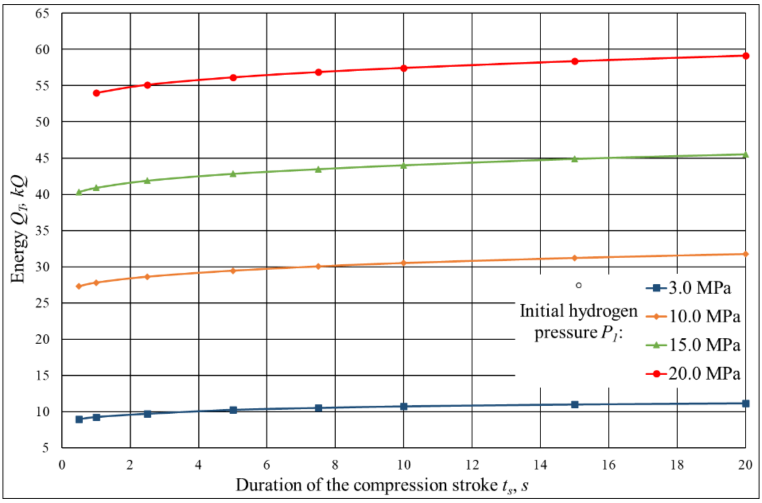

Fig. 12. The energy Q_T consumed for hydrogen compression for different durations of the compression stroke t_s, at initial pressures P_1 = 3.0, 10.0, 15.0 and 20.0 *MPa* and compression ratio K_c = 5.0.

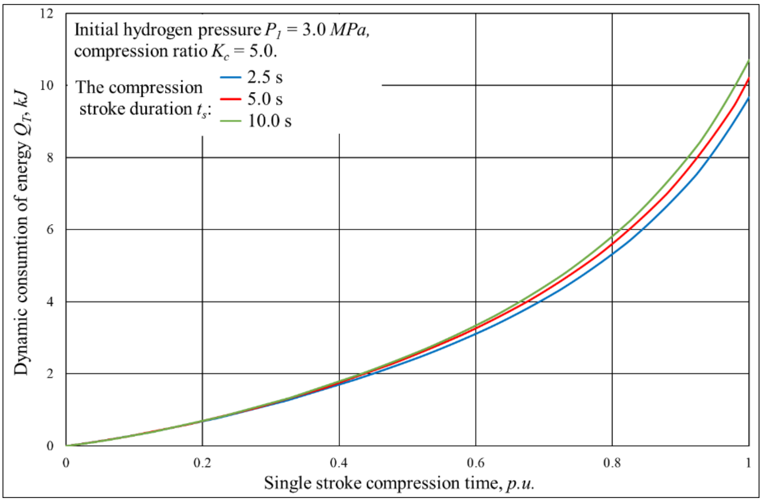

Fig. 13. The dynamic changes of the energy Q_T consumption for compression stroke durations t_s = 2.5, 5.0 and 10.0 *s,* at initial pressure P_1 = 3.0 *MPa* and compression ratio K_c = 5.0.

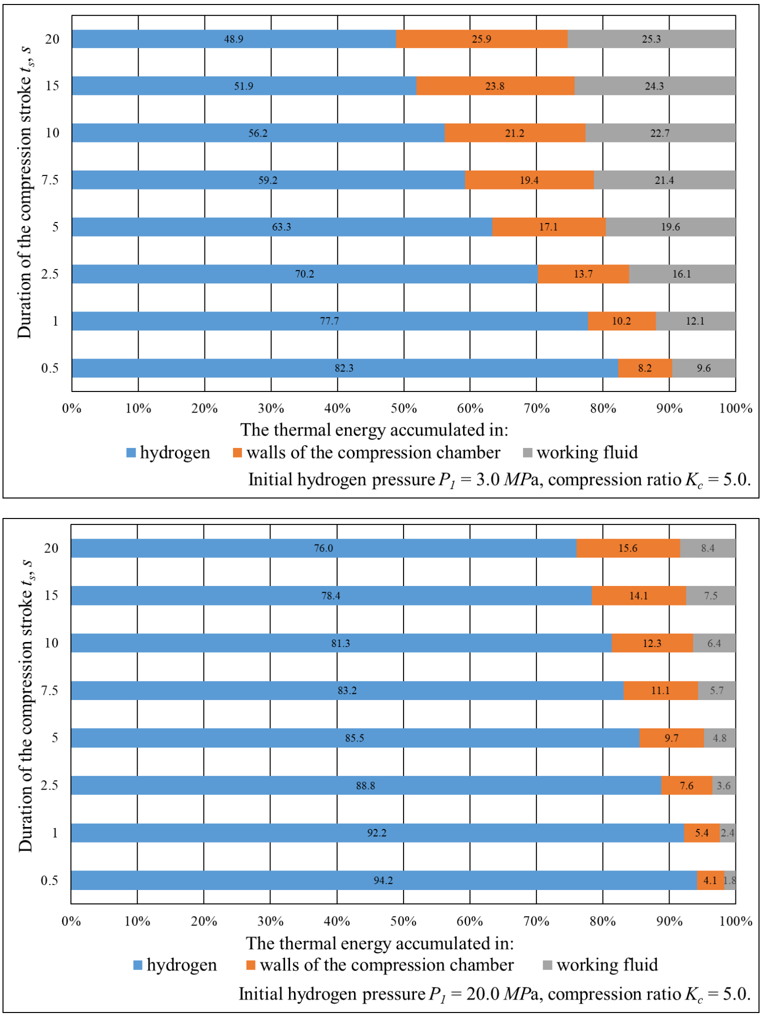

Fig. 14. Diagrams of thermal energy distribution Q_T between energies accumulated in hydrogen Q_H, working fluid Q_F and compression cylinder body Q_C for different durations of the compression stroke t_s at initial pressures $P_1 = 3.0$ *MPa* (top) and 20.0 *MPa* (bottom) and compression ratio $K_c = 5.0$.

To compare different compression scenarios, including stroke duration, initial pressure and cylinder geometry, overall temperature of the system ΔT_O, equivalent to the energy consumed for hydrogen compression, is employed. The overall temperature ΔT_O is defined as follows:

$$\Delta T_O = (Q_F + Q_H + Q_C)/(m_F c_F + m_H c_H + m_C c_C), \tag{7}$$

where Q_F, m_F, c_F; Q_H, m_H, c_H; Q_C, m_C, c_C – the energy, mass, and heat capacity of the work fluid, compressed hydrogen and cylinder steel, respectively.

The changes of the ΔT_O for the different durations of compression stroke t_s at initial pressures $P_1 = 3.0$, 10.0, 15.0 and 20.0 *MPa* and compression ratio $K_c = 5.0$ are shown in Fig. 15. As the pressure in the compression chamber increases, the ΔT_O increases proportionally, as can be seen by comparing the curves for an initial pressure from 3.0 *MPa* to 20.0 *MPa*. The temperature ΔT_O inside the compression chamber slightly increases with increasing compression stroke duration and mainly depends on the initial pressure.

However, for the considered compression pressures overall temperature value is within the range of less than 15.0 *K*. This means that the temperature conditions inside the compression chamber should not exceed the temperature limits defined as rated values for the working fluid.

According to these results, we also can estimate the actual pressure of hydrogen in the compression chamber. When the gas is heated the pressure rises according to Charles's law, and its value will be higher than the one calculated using relations derived from Boyle-Marriott's law according to Eq. (2). Considering overall temperature ΔT_O values, given in Fig. 15, the temperature-adjusted hydrogen pressure P_{3T} can be obtained from Eq. (8):

$$P_{3T} = P_3 (T_i + \Delta T_O)/ T_i , \tag{8}$$

where T_i = 300 *K* – initial temperature before compression;
P_3 – pressure in the compressed volume V_3 (Fig. 2.b), calculated using Eq. (2).

It is reasonable to assume that the actual hydrogen pressure will be 5 to 10 % higher than that obtained by Eq. (2). Bearing in mind the uncertainty of the mixing of liquid and gas inside the compression chamber, the instantaneous temperature of hydrogen and the corresponding pressure can have much higher values at the moment of the compression. Therefore, in order to handle the compression process and control the pressure rise, intensive cooling is required at the top of the cylinder, as this is where the maximum rise in hydrogen temperature is observed, as can be seen in Fig. 8.

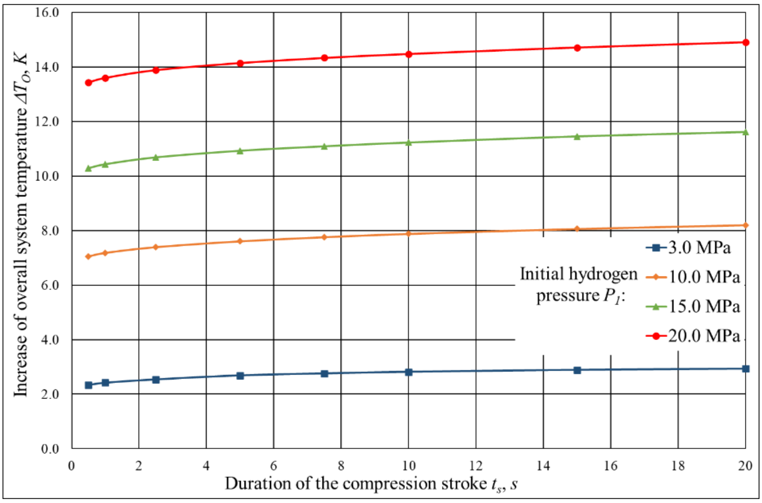

Fig. 15. Increase of overall system temperature ΔT_O for different durations of the compression stroke t_s, at initial pressures P_1 = 3.0, 10.0, 15.0 and 20.0 *MPa* and compression ratio K_c = 5.0.

Analysis of the energy required to perform a hydrogen compression stroke with a given compression ratio makes it possible to estimate the power of the liquid pump drive motor required to perform this work in a given time. As the first approximation, the value of this power can be determined from Eq. (9):

$$W = Q_T / t_s. \quad (9)$$

The curves of total power W for the examined models are presented in Fig. 16, where power is calculated as a function of duration of compression stroke t_s, at initial pressures P_1 = 3.0, 10.0, 15.0 and 20.0 *MPa* and the compression ratio K_c = 5.0.

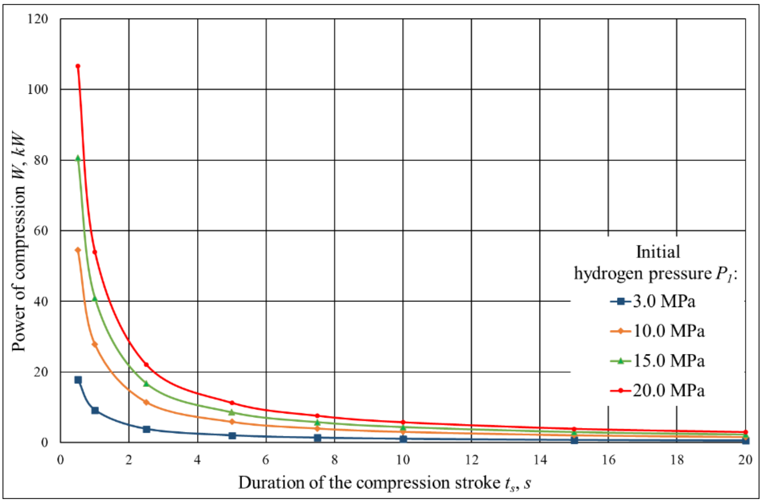

Fig. 16. The power W required for hydrogen compression for different durations of the compression stroke t_s, at initial pressures P_1 = 3.0, 10.0, 15.0 and 20.0 *MPa* and compression ratio K_c = 5.0.

Apparently, increase of compression stroke duration leads to a slight growth of energy consumption Q_T but at the same time the power W_T which is necessary to perform compression work significantly goes down. Consequently, the rated power of the liquid pump drive motor can be reduced, and the weight and dimensions of the pump can be minimized.

6. CONCLUSIONS

A hydraulic hydrogen compression system developed by the authors, employing fluid flow sensors to control the degree of compression, has been discussed.

The distinguishing feature of the considered system is that it can be adapted to changing inlet hydrogen pressure which is supplied from the external source. The proposed design allows widely regulating the speed of filling of high-pressure hydrogen storage with gas and rapidly increasing outlet pressure in the dispenser, performing quick vehicle recharging.

The developed numerical model of gas compression was successfully implemented and tested in the COMSOL Multiphysics® 6.0 software environment. This model can be successfully used for research and parametric studies of processes in hydraulic gas compression systems.

The thermodynamic process, which considers heat exchange between gas, working fluid and cylinder walls, and the process of convective heat transfer into surrounding space is implemented in the model.

The results of the numerical simulation

were verified with an adiabatic case, without heat exchange between gas and cylinder and working fluid.

Results of simulation of thermodynamic processes and their analysis allowed estimating energy consumption and determining conditions which would lead to an increase in the efficiency of operation of the hydrogen compression system under consideration.

ACKNOWLEDGEMENTS

The research has been financed by ERDF project "Experimental Studies and Development of Technology on Hydraulic Compression of Hydrogen" No 1.1.1.1/20/A/185, being implemented at Ventspils University of Applied Sciences. We are grateful to the Process Analysis and Research Centre (PAIC) Ltd.

REFERENCES

1. IRENA. (n.d.). Policies for Green Hydrogen. Available at https://www.irena.org/Energy-Transition/Policy/Policies-for-green-hydrogen
2. Peschel. A. (2020). Industrial Perspective on Hydrogen Purification, Compression, Storage, and Distribution. *Fuel Cells*, *20* (4), 385–393.
3. Fragiacomo, P., & Genovese, M. (2020). Developing a Mathematical Tool for Hydrogen Production, Compression and Storage. *International Journal of Hydrogen Energy*, *45* (35), 7685–7701.
4. European Commission. (2020). Communication from the Commission to the European Parliament, the Council, the European economic and social committee and the committee of the regions. A Hydrogen Strategy for a Climate-Neutral Europe. Brussels, 8.7.2020. COM (2020) 301 final.
5. IEA. (2021). *Global Hydrogen Review 2021*. IEA, Paris. Available at https://www.iea.org/reports/global-hydrogen-review-2021.
6. Yu, M., Wang, K., & Vredenburg, H. (2021). Insights into Low-Carbon Hydrogen Production Methods: Green, Blue and Aqua Hydrogen. *International Journal of Hydrogen Energy*, *46* (41), 21261–21273.
7. Sdanghi, G., Maranzana, G., Celzard, A., & Fierro, V. (2019). Review of the Current Technologies and Performances of Hydrogen Compression for Stationary and Automotive Applications. *Renewable and Sustainable Energy Reviews*, *102*, 150–170.
8. IEA. (2020). *Global Installed Electrolysis Capacity by Region, 2015–2020*. IEA, Paris. Available at https://www.iea.org/data-and-statistics/charts/global-installed-electrolysis-capacity-by-region-2015-2020.
9. Techcrunch. (n.d.). *Volvo AB and Daimler Trucks Team up in a Hydrogen Fuel Cell Joint Venture.* Available at https://techcrunch.com/2021/05/03/volvo-ag-and-daimler-trucks-team-up-in-hydrogen-fuel-cell-joint-venture/
10. Toyota. (nd.). *Toyota Mirai 2022 Edition*. Available at https://www.toyota.com/mirai/
11. Bezrukovs, V., Bezrukovs, Vl., Konuhova, M., Bezrukovs, D., & Berzins, A. (2022). Hydrogen Hydraulic Compression System for Refuelling Stations. *Latvian Journal of Physics and Technical Sciences*, *59* (3), 96–105. DOI: 10.2478/lpts-2022-0028.
12. Zou, J., Han, N., Yan, J., Feng, Q., Wang, Y., Zhao, Z., ...& Wang, H. (2020). Electrochemical Compression Technologies for High-Pressure Hydrogen: Current Status, Challenges and Perspective. *Electrochem. Energ. Rev., 3*, 690–729.

13. Humphrey, H.A. (1909). An Internal-Combustion Pump and Other Applications of a New Principle. *Proc. Inst. Mech. Eng., 1123*.
14. Joyce, N.G. (1984). The Humphrey pump – An internal combustion pump. In *Proceedings of the Conference on Small Engines and their Fuels in Developing Countries*, (pp. 31–44). Reading, Berkshire, England.
15. Van de Ven, J.D., & Li, P.Y. (2009). Liquid Piston Gas Compression. *Applied Energy*, *86* (10), 2183–2191. doi:10.1016/j.apenergy.2008.12.001
16. Bezrukovs, V., Bezrukovs, Vl., Bezrukovs, D., Orlova, S., Konuhova, M., Berzins, A., ... & Pranskus P. (2021). *Hydrogen Hydraulic Compression Device*. WO2023017306, 16.03.2023.
17. Bezrukovs, V., Bezrukovs, Vl., Bezrukovs, D., Konuhova, M., & Berzins, A. (2022). *Hydrogen Hydraulic Compression Device*. LVP2022000071, 31 August 2022.
18. Bezrukovs, V., Bezrukovs, Vl., Bezrukovs, D., Konuhova, M., & Berzins, A. (2022). *Hydrogen Hydraulic Compression Device*. PCT/IB2022/058904, 21 September 2022.
19. Enapter. (n.d.). *AEM Electrolyser EL 4.0, Datasheet*. Available at https://handbook.enapter.com/electrolyser/el40/downloads/Enapter_Datasheet_EL40_EN.pdf

LATVIAN JOURNAL OF PHYSICS
AND TECHNICAL SCIENCES
2023, N 4

DOI: 10.2478/lpts-2023-0023

ACOUSTIC EMISSION METHOD AS A MEANS OF QUALITY CONTROL IN MULTILAYER WELDING OF THICK-WALLED WELDED JOINTS

K. Carjova*, M. Banov, L. Vinogradov, S. Kravchenko, G. Strautmanis

Riga Technical University, Latvian Maritime Academy,
12 Flotes Str., LV – 1016, Riga, LATVIA
*e-mail: Kristine.Carjova@rtu.lv

The article reviews the capacities of the acoustic emission method usage to assess the technical condition and integrity of thick-walled welded structures, the quality control of welded joints in multilayer welding. As a result of the analysis of AE control data, the authors propose a set of informative parameters of the AE method, which form a criterion space for separating the reflected signals from defects and signals from interference.

Keywords: *Acoustic emission control, seam welding, welding process*.

1. INTRODUCTION

The welded seam area is usually the most probable epicentre for the occurrence of fracture of the object due to various factors that reduce the efficiency of welded joints. Timely detection of a defect and reliability of measurement results using methods of non-destructive testing (NDT) are the most important tasks in the inspection of welded joints [1], [2].

Traditional testing methods such as magnetic particle (MT), ultrasonic (UT) and radiographic testing (RT) [2] are mainly used for the inspection of welded joints. These methods mainly aim at evaluating the degree of hazard of a defect, according to the equivalence of the area or the size of the imprint on the image. However, they do not take into account the level of stress concentration generated by the defect, which leads to an increase in the local operating pressure system that actually determine the degree of defect hazard.

The structural complexity of the object, the laboriousness of performing a full-fledged inspection by traditional NDT types, even with complex application of different inspection methods, do not guarantee the complete absence of potentially dangerous defects in the product. This leads to the assertion that the task of improving NDT technologies, especially in the production of large-sized welded structures, is urgent. Based on the experience of NDT specialists, it can be concluded that it is necessary to include the method of acoustic emission (AE) together with other methods in the technological process of production control [2], [3]. Moreover, this method should be considered as equivalent and independent, complementary to traditional methods [2]. The AE method has a number of distinguishing features and is based on the registration of elastic energy waves generated by local destruction of the material during its deformation.

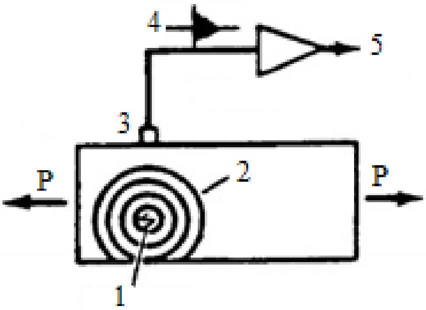

The AE method by its physical nature is able to detect only developing defects, which are therefore the most dangerous [2]. Figure 1 illustrates the principle of recording an acoustic signal from a defect under the action of a load on the structure. In this case, it is not a question of determining the location and magnitude of the defect, but only its presence or absence.

Fig. 1. Acoustic signal stimulation, 1 – defect; 2 – stress wave; 3 – sensor; 4 – AE signal; 5 – registration.

The most promising application of the AE method is the control of the welding process. Here, the deformed state of the material is realized in a natural way by the tensile stresses generated during the cooling of the weld pool. At the same time, in contrast to other NDT methods, which can only be performed fragmentarily during the welding process, the AE method is able to detect inadmissible defects during the welding process as the weld passes through. As a result, it is possible to reduce the labour intensity of the process of defect correction, as well as to reduce the negative consequences for the strength properties of the weld sections, which occur in the case of deep scanning of the defect and subsequent welding [2], [4], [5], [9], [10].

The disadvantage of the AE method is the lack of information about the size of the defect, about its geometrical parameters and the depth of occurrence. However, other acoustic testing methods are unable to measure the actual dimensions of the defect. The shock pulse method makes it possible to judge the presence of a defect from the sound of the stimulated sound wave, but it is impossible to determine the size of the defect using this method. The ultrasonic method allows determining the size of the defect along the length, but this causes difficulties in determining the size of the defect in depth. At the same time, information about the geometry of the defect they portray allows for the establishment of overestimated exclusion criteria that provide a margin of safety [2].

For a substantiated and reliable conclusion about the pre-hazardous condition of a welded object, it is necessary to apply various NDT methods, including the AE method [4], [6], [8]. In this article, a practical example is used to study the possibility of using the AE method as one of the main methods of monitoring the presence of various types of defects in the manufacture of thick-walled welded structures. This will make it possible to reasonably include this control method in the technological process of industrial control. All measurements described in the article were performed by using portable AE Pocket equipment.

2. CONTROL CONDITIONS AND USED EQUIPMENT

The assessment of the object condition by the method of acoustic emission was carried out with a portable two-channel device Physical Acoustics Pocket AE (Fig. 2), a piezoacoustic sensor and an external preamplifier Physical Acoustics Corporation IL -LP-WS with a bandwidth of 100–1000 KHz. The control used a channel with a discrimination level of +23 dB, at a speed of 1MSPS.

The technical assessment of the object was carried out at a temperature of +17 °C. The temperature of the product was adjusted to the ambient temperature to exclude the occurrence of acoustic emissions due to thermal deformation of the product. The thermal state of the object was monitored by an IR-891 thermal camera and confirmed by a snapshot (see Fig. 3).

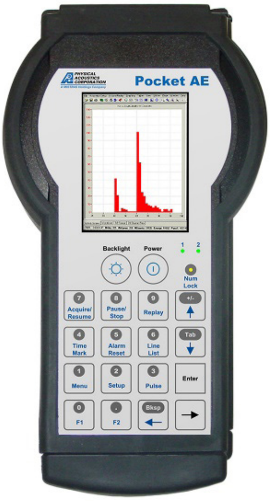

Fig. 2. Pocket AE-2 Kit Inventory No.8520232001 made in the USA.

3. THE OBJECT AND TESTING PROGRAM

A multilayer weld of a cylindrical steel bushing made of steel grade S355J2 was considered as the object of investigation for quality control and evaluation using the AE method. The geometrical dimensions of the cylindrical bushing were: Outer diameter D = 800 mm, inner diameter d = 720 mm, length *l* = 1000 mm. The tested object was installed horizontally on the test bench at all stages of the study. The position of the weld during the study varied from top to side. A hydraulic jack, located inside the object, provided a mechanical tensile load in the vertical direction. When the jack was outside the object, a compressive force was applied to the side surface of the sleeve. The object testing program was developed taking into account the recommendations [6], [7] and the maximum permissible elastic deformation of 1.7 mm at the point of force application under the load applied in the direction of the bushing diameter (see Fig. 4).

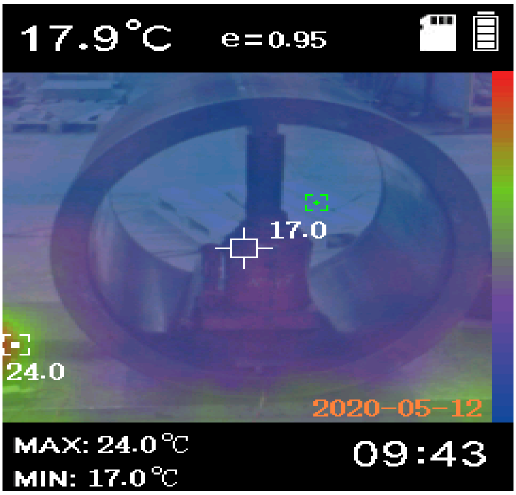

Fig. 3. Thermal image of the object during the AE test.

Testing program No. 1 (Fig. 4):

1. Vertical tensile load within the elastic deformation of the object with a movement of +1.0 mm from the original dimension at the jack attachment point;
2. Exposure under load for 5 minutes;
3. Increasing the vertical tensile load within the elastic deformation of the object with the provision of the movement of +1.5 mm from the original size at the jack attachment point;
4. Exposure under load for 5 minutes;
5. Increasing the vertical tensile load within the elastic deformation of the object with the provision of movement of +1.7 mm from the original size at the jack attachment point;
6. Exposure under load for 5 minutes;
7. Unloading the object.

Fig. 4. Installation diagram of the tensile loading device.

In the second test, the object was rotated 900 about its axis so that the weld was located in the horizontal plane on the lateral surface of the cylinder.

A piezo-acoustic sensor, which detects the acoustic emission signal, was placed near the weld seam at a distance of 10 mm from the centre of the weld seam during the test. The acoustic contact between the object and the sensor was established and mechanically fixed by the grease CIATIM-221CF (Fig. 5).

Fig. 5. AE sensor installation method.

Testing program No. 2 (Fig. 4):

1. Vertical tensile load within the elastic deformation of the object with a movement of +1.0 mm from the original dimension at the jack attachment point;
2. Exposure under load for 5 minutes;
3. Increase in the vertical tensile load within the elastic deformation of the object with a movement of +1.5 mm from the original dimension at the jack attachment point;
4. Exposure under load for 5 minutes;
5. Increase in the vertical tensile load within the elastic deformation of the object with the provision of movement of +1.7 mm from the original size at the jack attachment point;
6. Exposure under load for 5 minutes;
7. Unloading the object.

In the third experiment, the tensile load was replaced by a compressive load (see Fig. 5). In this case, the weld was located on the side, in the same way as in the second experiment. The experiment did not consist of three stages, as before, but of two.

Testing program No. 3 (see Fig. 6):

1. Vertical compressive load within the elastic deformation of the object with the provision of displacement –0.7 mm from the original dimension at the jack attachment point;

2. Exposure under load for 5 minutes;
3. Increase in the vertical compressive load within the elastic deformation of the object with the provision of displacement –1.0 mm from the original size at the jack attachment point;
4. Exposure under load for 5 minutes;
5. Unloading the object.

In this case, the hydraulic press provided a compressive load on the upper surface of the sleeve in the vertical direction.

Fig. 6. Installation diagram of the compressive loading device.

4. CONTROL RESULTS

TEST No. 1 contains a characteristic acoustic emission pattern for a "defect-free" object. An increase in emission intensity with increasing load is a typical pattern that corresponds to a normal structural pattern that is in line with normal structural changes in microdislocations of the weld material. There is an insignificant spontaneous emission at the stages of exposure (second $t_1 = 390$, second $t_2 = 650$) (Fig. 7).

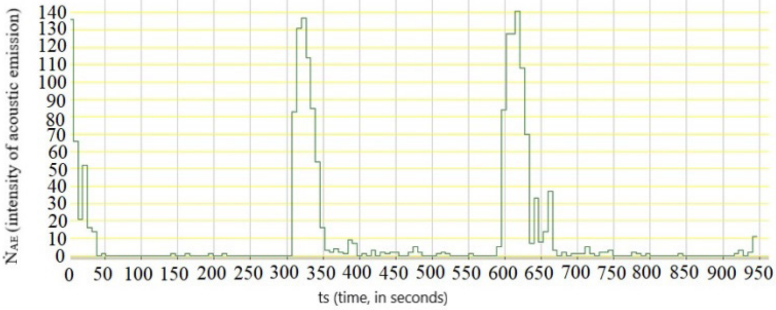

Fig. 7. AE Intensity in the first test.

At the same time, the energy of the AE events is predominantly low, 90 % of the events have an amplitude below 60 dB and most of the emission pulses are not indicators of the presence of dangerous cracks (Fig. 8).

Spectral analysis of the AE signals shows the presence of resonance in the 110–130 KHz zone, which corresponds to the spectral character of dislocations of subcritical size in steel. Based on the analysis of the spectrum, it can be concluded that there is no significant number of large-sized destructible cavities in the weld (Figs. 8 and 9).

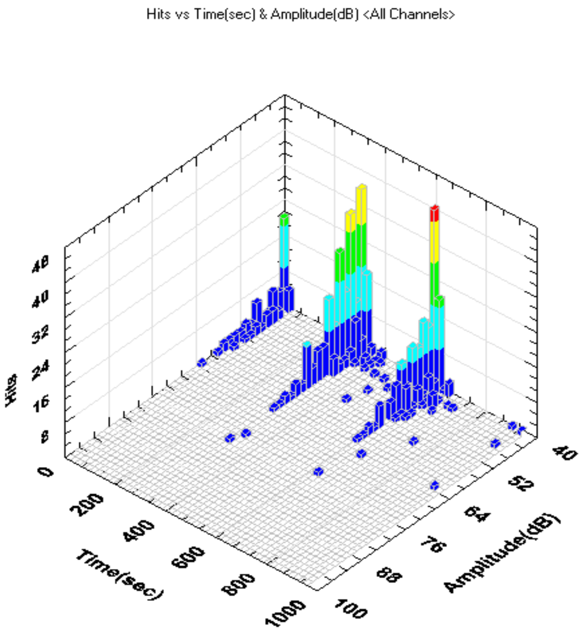

Fig. 8. Energy and intensity of AE in the first test.

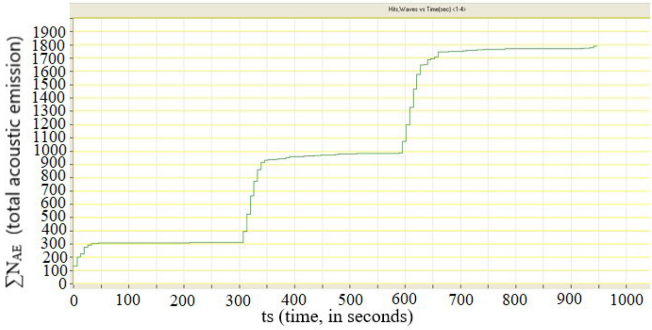

Fig. 9. Cumulative emission of AE during the first test.

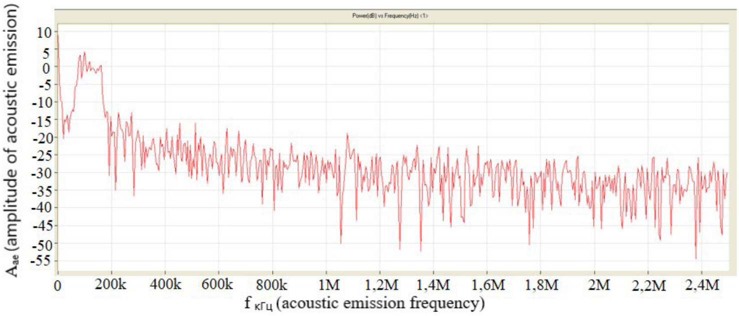

Fig. 10. Spectral analysis of AE of the first test.

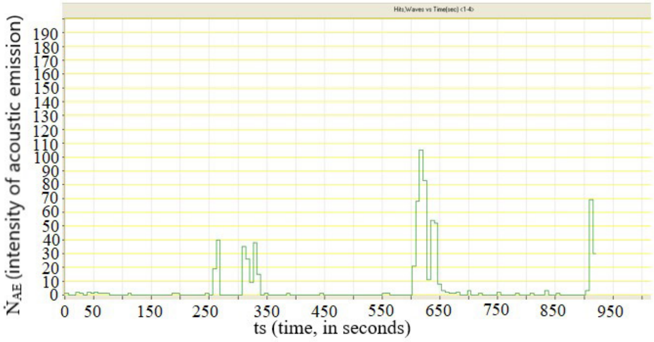

Fig. 11. AE intensity during the second test.

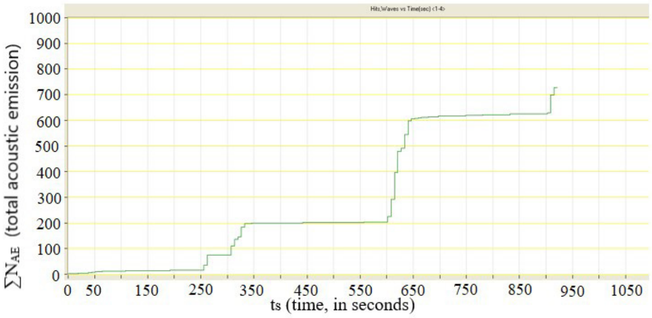

Fig. 12. AE intensity and amplitude during the second test.

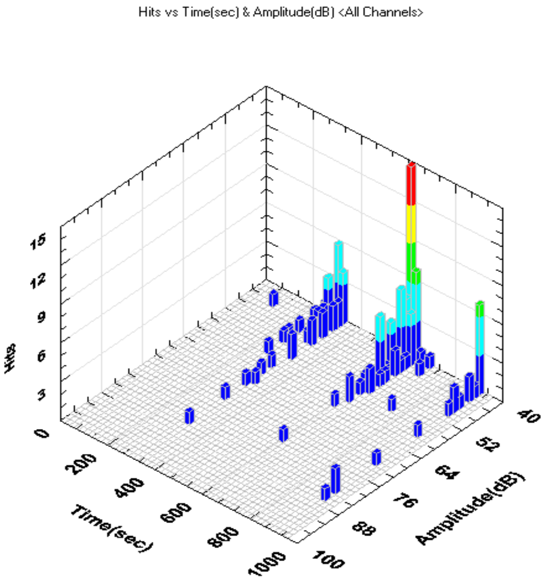

Fig. 13. Cumulative AE emission during the second test.

In TEST No. 3 (compression) the picture is similar to the first two tests (Figs. 14–16) and its parameters are determined by the following:

1. Moderate emission at the time of change; mechanical stress dominated by low-amplitude events;
2. Absence of significant spontaneous emission during the static part of the experiment;
3. Spectral resonance corresponds to microdislocations typical of a satisfactory weld condition.

The results of the product compression test are shown in Figs. 14–16.

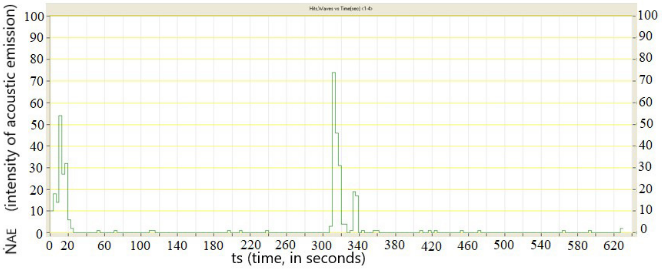

Fig. 14. Compressive loading. AE intensity.

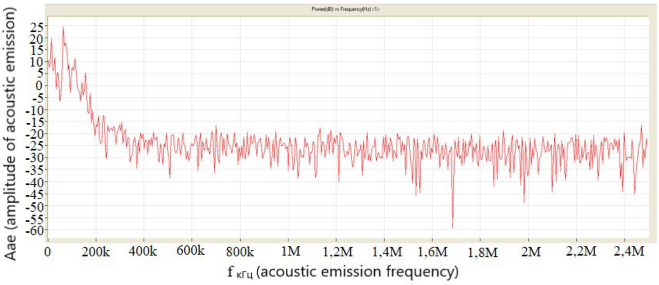

Fig. 15. Compressive loading. AE intensity and amplitude.

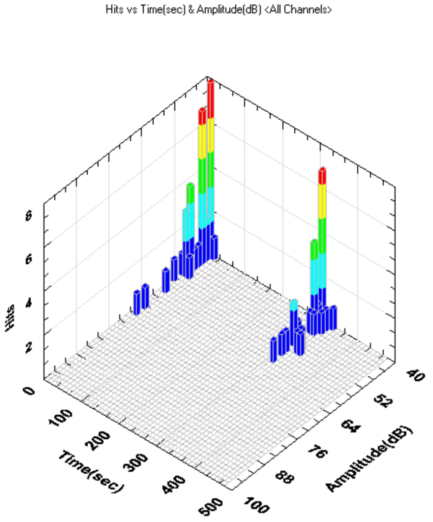

Fig. 16. Spectral analysis of AE under compressive load.

As the first example confirming the effectiveness of the method AE, this paper presents the results of quality control of butt welding of rails under static load during the test. In Fig. 17, the fractures of the rails at the welding point are shown. As can be seen in Fig. 17, the defects were found in samples No. 2 and No. 3, while in sample No. 1, no defects were observed.

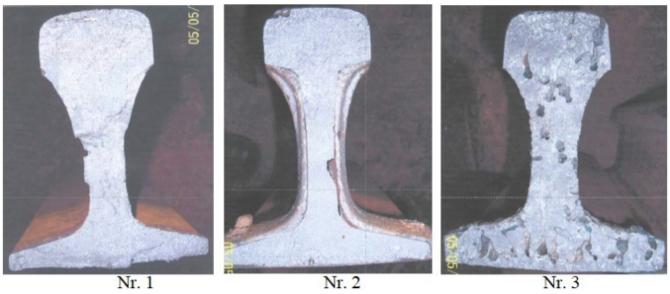

Fig. 17. Samples of welded rail joints. No. 1 – no defects were found; No. 2 – the defect is fixed (inclusions); No. 3 – the defect is fixed (pores).

Prior to the destruction of the rails at the location of the weld, tests were conducted to determine defects using the AE method. The results of the study are presented in Fig. 18, which shows diagrams of the dependence of the total amount AE on time.

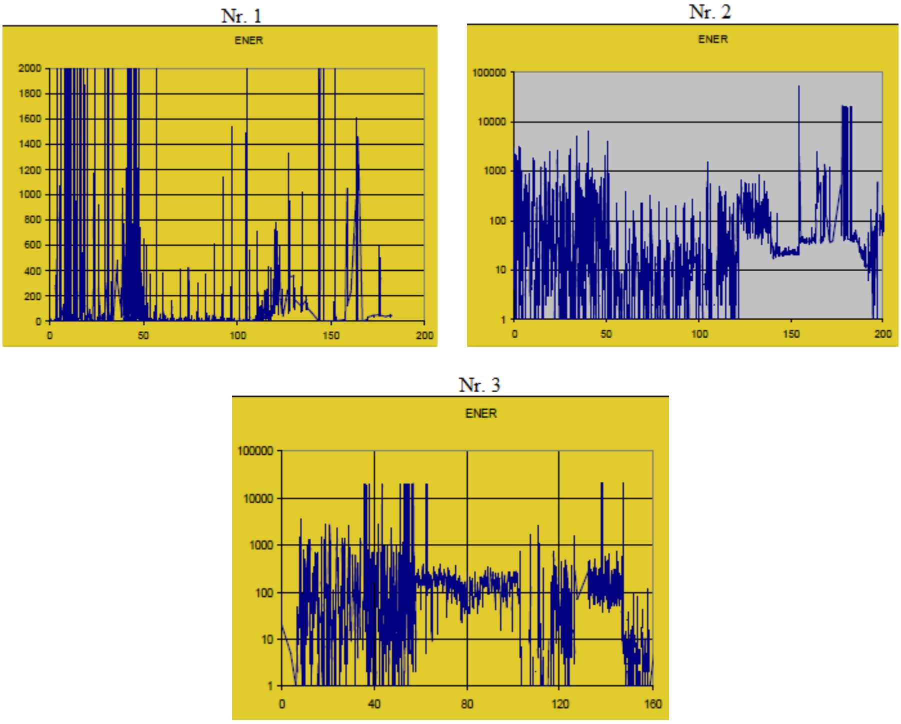

Fig. 18. Diagrams of dependence of the total amount AE in rail welding on time. No.1 – no defects were found; No.2 and No.3 – the defect was fixed.

As can be seen in Fig. 18, in the presence of defects in the weld, the total number of AE increases, which makes it possible to control the quality of welds in thick-walled products.

The AE method is also effective in controlling the welding process of thick-walled products, which is confirmed in the second example, which involves electrical resistance welding of rails.

The welding process consists of four main steps:

- I – heating (the ends of the rails are heated by an arc with a gap between them);
- II – resistance heating (the ends of the rails are joined together and then intensively heated due to the resistance of the circuit between the rails);
- III – the welding process itself (melting the metal in the seam);
- IV – the pressing together of the joints and the spreading of the materials of the parts to be joined (while the current is switched off).

The AE signals recorded by the sensors installed on the rail show that the intensity of AE is different in each phase (Fig. 19). Thus, significant sporadic emissions of AE intensity are observed in the first phase; in the next phase, the AE level is significantly reduced; an increased intensity level is observed during the welding process, which decreases again in the last phase. Therefore, if the welding technique is followed, it is possible to clearly identify and highlight all phases of welding [7], [8].

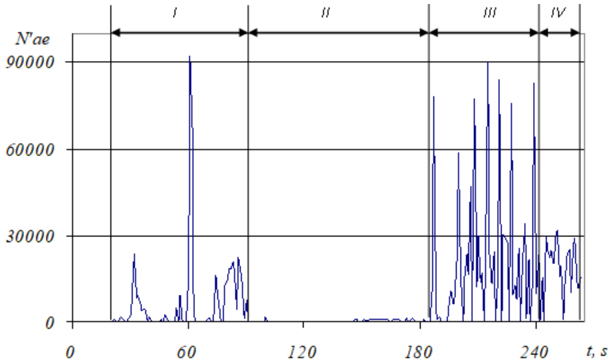

Fig. 19. AE intensity N'_{ae} versus welding time.

When deviating from the standard welding method, the type of change in AE intensity differs significantly at one or more stages (Fig. 20).

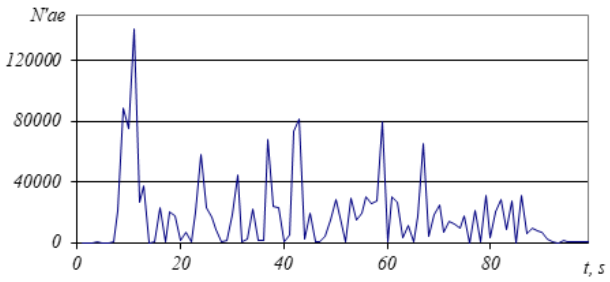

Fig. 20. AE intensity N'_{ae} versus welding time.

5. CONCLUSION

1. The welded seam of the tested object is in a satisfactory condition and does not contain defects with critical parameters that could be detected by the AE method.
2. The welding condition of the controlled object under cyclic loading is characterised by a low level of signal sources and does not contain defects with critical parameters.
3. Evaluation of the basic possibility of detection of welding defects is possible by the AE method in the manufacture of welded joints.
4. The development of AE technologies for quality control of welded joints and the application of AE method will increase the operational safety of welded structures for various purposes.
5. The results of the research allow recommending the AE method as a routine method in the technical process of quality control of welds.

Under test conditions, it is necessary to minimize mechanical, electrical sparks, and electromagnetic interference both from the sources of the test setup and from extraneous sources. To assess the impact on the polycrystalline structure, it is necessary to find out the manufacturing technology of the object to determine the maximum voltage zones.

ACKNOWLEDGEMENTS

The research has been supported by the Latvian Science Council, project “Development of Smart Technologies for Efficient and Well-thought-out Water Operations (STEEWO)” (No. Lzp-2019 / 1-0478).

REFERENCES

1. Greshnikov, V.A. (1976). *Acoustic Emissions. Application for Testing Materials and Products* / V.A. Greshnikov, Yu.B. Drobot. M.: Publishing House of Standards.
2. Karlov, S.A., Sulzhenko, V.A., & Yakovlev, A.V. (2019). Acoustic Emission Control of the Quality of Welded Joints in Marine Engineering Facilities. *Proceedings of the Krylov State Scientific Center, 1,* 130–136.
3. Gumenyuk, V.A., Yakovlev, A.V., & Sulzhenko V.A. (2018). Acoustic Emission Control of Assembly Welding of Ship Pipeline Systems. M.: Mechanical Engineering.
4. Ivanov, V.I. (1981). *Acoustic Emission Control of Welding and Welded Joints* / V.I. Ivanov, V.M. Belov. M.: Mechanical Engineering.
5. Quality control of welded joints in the welding process using the method of acoustic emission / Barinov A.V., Fedorov, A. V., Kinzhagulov, I. Y., Sergeev, D. S., A. Dorenskaya // Scientific and technical journal ITMO. - 2013.No. 5 (87) - p. 144 - 148.
6. Elchaninov, G.S., & Nosov. V.V. (2011). Methodology for assessing the resource of complexly loaded welded joints. *Science and Education: Materials of the*

1st International Scientific-Practical Conference. SPb.: Publishing House of Polytechnic University, pp. 212–218.

7. Urbahs, A., Banovs, M., Doroško, S., Turko, V., & Feshchuk, Y. (2010). Acoustic Emission Checking of Welded Rail Joints. In *Mechatronic System and Materials: Abstracts*, (p. 209). 5–8 July 2010, Opole, Poland.
8. Evseev, D., Medvedev, B., Medvedev, P., Strautmanis, G., & Samoshkin, S. (2019). Acoustic Emission Approach to Determining Survivability in Fatigue Tests. In *Procedia Computer Science. Vol.149: ICTE in Transportation and Logistics 2018 (ICTE 2018)*, (pp. 282–287). 1 January 2019. Lithuania, Klaipeda.

LATVIAN JOURNAL OF PHYSICS
AND TECHNICAL SCIENCES
2023, N 4

DOI: 10.2478/lpts-2023-0024

THE INFLUENCE OF THE THERMAL EFFECT ON THE STRESS-STRAIN STATE OF THE SOIL

N. Remez[1], A. Dychko[1], A. Kraychuk[2], S. Kraychuk[2], N. Ostapchuk[2]

[1] National Technical Universty of Ukraine
“Igor Sikorsky Kyiv Polytechnic Institute”
37 Peremohy Ave., Kyiv, 03056, UKRAINE
[2]Rivne State University of Humanities
12 Stepana Bandery Str., Rivne, 33028, UKRAINE
E-mail: aodi@ukr.net

The present paper provides the dependence of the temperature change on time and the depth of the soil massif based on numerical calculations. Mathematical modelling of the one-dimensional soil temperature field via an algorithm and a PC program is carried out without taking into account the influence of the phase transition of moisture in the soil pores during seasonal freezing and thawing using the finite difference method. The amplitude of fluctuations in the temperature regime is obtained as that decreases with depth from the soil surface. It is established that over time heat spreads from the pipeline to the surface of the soil, and over time more intense heating occurs both near the pipeline and in the body of the soil massif.

Keywords: *Heat transfer, mathematical modelling, soil, stress-strain state.*

1. INTRODUCTION

The temperature field of the soil and the influence of the thermal effect on its stressed and deformed state are quite important factors that must be taken into account when erecting structures and buildings on these soils. If one of these factors is completely or partially neglected in the designing of structures, unacceptable deformations occur, which complicate their operation and lead to partial or complete destruction [1], [2].

If the sediments that occur during the thawing of frozen soils around the foundations of buildings are not foreseen by the project, and their value is greater than the limit values for this building, then unacceptable deformations and destruction of the foundations and super-foundation structures occur inevitably.

The simultaneous influence of static load and thermal effect on the stress-strain state of the soil massif is one of the key issues in the design and operation of any buildings or structures. Therefore, the definition and justification of this factor is relevant.

In recent decades, interest in understanding the thermomechanical behaviour of soil has increased significantly, which is explained by many reasons, the main ones of which are: 1) deep burial of waste, which is a source of heat, in geological formations; 2) carrying out drilling operations; 3) laying of high-voltage cables in the soil; 4) seasonal and daily temperature fluctuations, which significantly affect road surfaces and building foundations [3]–[5].

Sources of heat release that heat groundwater can be conventionally divided into two types. The first includes natural underground sources of heat release. The second one – heat-releasing structures erected on the surface of the earth or near it.

In [6], [7] it is stated that the influence of temperature on the physical state of porous sedimentary rocks is manifested in the form of changes in the characteristics of rock-forming minerals, as well as structural changes of rocks due to thermal expansion of minerals: additional compaction of rocks under the action of mechanical stresses due to an increase in the plasticity of some minerals (for example, calcite) with increasing temperature; other minerals, on the contrary, lose plasticity and become brittle as the temperature increases. At the same time, the compressive strength of these minerals decreases, which leads to the formation of microcracks in the rock. Thermal stresses lead to the fact that micro-destructions occur in various parts of the rock, which are reflected in the rock structure.

Thus, the physical properties of rocks change as the temperature increases not only due to the change in the characteristics of individual rock phases, but also due to the deformation of the skeleton and the reduction of the pore volume [8].

The aim of the research is to predict changes in the stress-strain state of the soil as a result of the thermal effect of natural and man-made factors.

2. THERMAL EFFECT ON THE STRESS-STRAIN STATE OF THE SOIL SIMULATION

At the first stage, the problem of the non-stationary annual thermal regime of the soil is considered. The differential equation of thermal conductivity through the soil has the form

$$c\rho\frac{\partial t}{\partial z}=\frac{\partial}{\partial x}\left[\lambda\frac{\partial t}{\partial x}\right],\quad z>0. \tag{1}$$

Equation (1) of each homogeneous layer of the soil can be rewritten as follows:

$$\frac{\partial t}{\partial z}=a\frac{\partial^2 t}{\partial^2 x},\quad z>0, \tag{2}$$

where c – specific heat capacity of the soil, J/(kg °C); ρ – density of the soil, kg/m^3; λ – coefficient of thermal conductivity of the soil, W/(m °C); a – coefficient of thermal conductivity of the soil, $a=\frac{\lambda}{c\rho}$, m^2/c; x – distance along the coordinate deep into the soil, starting from its surface, m; $t(x,z)$ – temperature, °C, at any point x in the depth of the soil and at any moment of time z from the beginning of the countdown.

The initial temperature distribution in the soil layer is known (for example, it can be assumed to be constant in depth and equal to the average multi-year, average annual temperature of the surrounding air):

$$t(x,0) = \; t^0(x) = idem, \;\; 0 \le x \le H, \;\; z = 0; \tag{3}$$

$$t(x,z) = g(x,z), \;\; 0 \le x \le H, \;\; z = 0, \tag{4}$$

where H – depth of the considered soil massif, m.

As limit conditions on the surface of the earth, the heat exchange of the outer surface with the outer air, absorption of heat from solar radiation falling on the horizontal surface, and long-wave radiation into the Earth's atmosphere are taken into account:

$$\lambda \frac{\partial t}{\partial x}\Big|_{x=0} = a_h(t_c - t_s\big|_{x=0}) + Pq_{tr} - \varepsilon \cdot q_{lr}; \;\; \mathrm{x} = 0; \;\; z > 0. \tag{5}$$

The condition can be written more simply by entering the conditional temperature of the environment:

$$t_c = t_o + q_{tr} \cdot \frac{P}{a_h} - \frac{\varepsilon \cdot q_{lr}}{a_h}, \tag{6}$$

i.e., on the Earth's surface, heat exchange takes place with the environment, which has a temperature equal to the conventional one:

$$-\lambda \frac{\partial t}{\partial x}\Big|_{x=0} = a_h(t_c - t_s\big|_{x=0}), \;\; \mathrm{x} = 0; \;\; z > 0. \tag{7}$$

Since the heat flow from the centre of the Earth [9] is 0.06–0.10 W/m^2, which is on average equal to 0.03 % of the flow of solar radiation absorbed by the Earth's surface, then the condition of heat flow at the lower boundary of the soil massif is assumed as

$$-\lambda \frac{\partial t}{\partial x}\Big|_{x=\mathrm{H}} = 0, \quad \mathrm{x} = \mathrm{H}, \;\; z > 0, \tag{8}$$

where t_o, t_c – known variable throughout the year temperatures of outdoor air and conditional of environment, °C; t_s – unknown variable throughout the year temperature of the soil surface, °C; a_h – known coefficient of heat exchange on the soil surface, W/(m^2 °C), can be variable over time depending on the wind speed; $q_{t.}$ – intensity of total solar radiation falling on the soil surface, W/m^2; P – coefficient of absorption of solar radiation by the soil surface; q_{lr} – heat flow of long-wave radiation from the soil surface to the Earth's atmosphere; ε – degree of blackness of the radiating body. For soil, according to recommendations [9], the value is taken as equal to 0.96.

According to ASHRAE recommendations, the value of heat flux for horizontal surfaces should be taken as 63 W/m^2. Research on the transfer of long-wave radiation in the atmosphere [10] indicates the possibility of calculating the heat flow using the sky temperature, which is equal to the temperature of the surface of the clouds, component – 12 °C. Calculating the heat flow according to the Stefan-Boltzmann law, we will get 80.4 W/m^2 for the conditions of Kyiv. The heat transfer coefficient of the Earth's surface (a_h, W/m^2 °C), is calculated as follows:

$$a_h = 1{,}16\,(5 + \sqrt{v}), \tag{9}$$

where v – wind speed at the moment of time under consideration, m/s.

The solution of the problem is carried out by the method of finite differences using an implicit difference scheme with a lead, which has an approximation error of the order of $O(\Delta z + \Delta x^2)$ [11], an algorithm and a program for a PC in the Pascal are developed.

Figures 1–4 present the results of numerical calculations for a soil massif with a depth of 20 m with thermophysical parameters c=840 J/(kg ·K); ρ=1800 kg/m^3; λ=1.2 W/(m·K) in the form of graphical dependences of temperature on time (month) at different depths of the soil. Different colours indicate different distances from the free surface of the soil.

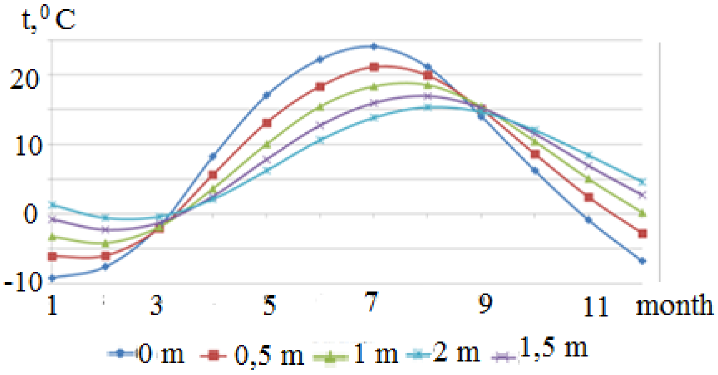

Fig. 1. Distribution of temperature over time at a soil depth of up to 2 m.

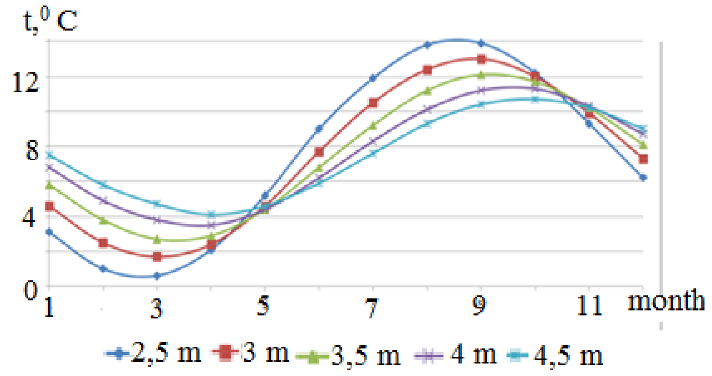

Fig. 2. Distribution of temperature over time at a soil depth of 2.5 up to 4.5 m.

The obtained dependences indicate the delay of the temperature maximum and temperature minimum relative to the fluctuation of the annual conditional temperature of the atmospheric air; the more the temperature, the deeper the calculated soil mark. The resulting effect occurs due to the thermal inertia of the soil and depends on its type and properties.

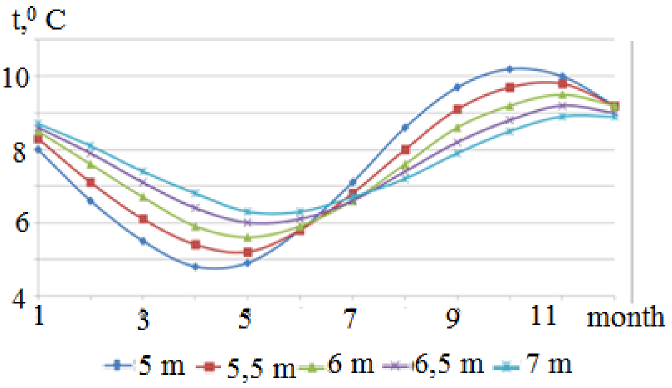

Fig. 3. Distribution of temperature over time at a soil depth of 5 up to 7 m.

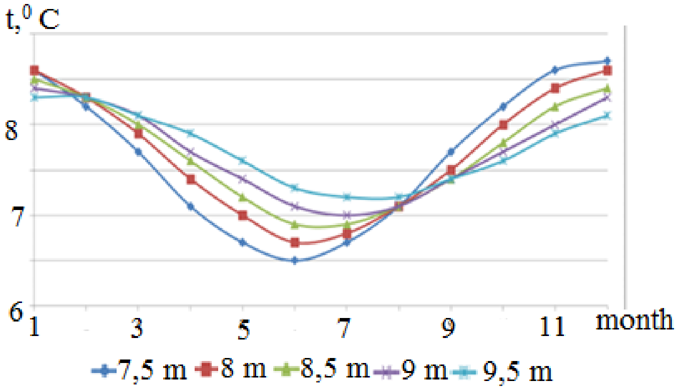

Fig. 4. Distribution of temperature over time at a soil depth of 7.5 up to 9.5 m.

Based on the obtained data, a graph of the range of values of the annual temperature amplitude in the depth of the soil massif is constructed (Fig. 5).

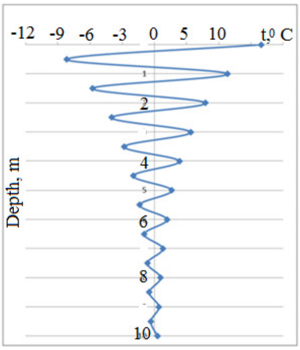

Fig. 5. Range of the annual temperature amplitude deep into the soil massif.

From the analysis of this dependence, it is worth noting that the nature of the attenuation of the temperature amplitude deep into the soil massif has a smaller scope due to the fact that the processes of seasonal freezing and thawing of the soil and the influence of snow cover are not taken into account. However, it should be noted that the influence of these factors decreases with depth, and minor temperature fluctuations remain at significant depths throughout the year. This gives grounds for using the soil massif as a working fluid in heat pumps.

At the second stage, the process of interaction between the thermal fields of the soil and the underground pipeline is considered.

The process of heat transfer in the soil layer is analysed, on one boundary of which there is heat exchange with the environment, and on the other – with the hot water supply pipeline. Heat transfer is considered based on the Stefan-Boltzmann law.

The mathematical formulation of the problem is based on the Fourier-Kirghoff equation, which establishes the relationship between temporal and spatial changes in temperature at any point of the area under consideration, and has the form

$$\rho c\frac{\partial T}{\partial t} = \lambda\left(\frac{\partial^2 T}{\partial x^2} + \frac{\partial^2 T}{\partial y^2}\right), \quad \left|\begin{matrix} 0 < x < L \\ 0 < y < H \end{matrix}\right., \tag{10}$$

where ρ – soil density, kg/m^3; c – specific heat capacity of the soil, W/m °C; λ – coefficient of thermal conductivity, W/m °C; L – length of the soil open-cast, m; H – depth of the soil open-cast, m.

The initial and limit conditions are written as follows:

$$\begin{aligned}
&t = 0: && T = T_0, \quad 0 \le x \le L, \quad 0 \le y \le H;\\
&x = 0: && -\lambda\frac{\partial T}{\partial x} = \chi_1(T^{e1} - T) + \varepsilon\sigma((T^{e1})^4 - T^4), \quad t > 0, \ \chi_1 > 0;\\
&x = L: && \lambda\frac{\partial T}{\partial x} = \chi_2(T^{e2} - T) + \varepsilon\sigma((T^{e2})^4 - T^4), \quad t > 0, \ \chi_2 > 0;\\
&y = 0: && -\lambda\frac{\partial T}{\partial y} = \chi_2(T^{e2} - T) + \varepsilon\sigma((T^{e2})^4 - T^4), \quad t > 0, \ \chi_2 > 0;\\
&y = H: && \lambda\frac{\partial T}{\partial y} = \chi_3(T^{e3} - T) + \varepsilon\sigma((T^{e3})^4 - T^4), \quad t > 0, \ \chi_3 > 0;
\end{aligned} \tag{11}$$

where ε – given degree of blackness; σ = 5,669W/(m^2 K^4) – Stefan-Boltzmann constant.

To approximate the differential level (10), a locally one-dimensional scheme [11] is used, which is absolutely stable and has the property of total approximation. To calculate the temperature field, an algorithm and a PC program in Pascal are developed.

The heat transfer process in the soil massif is analysed, on one boundary of which there is heat exchange with the environment, and on the other – with the hot water supply pipeline.

To solve the problem, an open-cast of the soil with a length L = 30 m and a depth H = 5 m is considered, on which the hot water pipeline is located. Thermophysical parameters of the solution area of the problem and soil properties are given in Tables 1 and 2.

Table 1. Parameters of the Problem Solution Area

Parameter	Designation	Value	Dimensionality
Coefficient of heat exchange at the soil-soil border	χ_1	25	W/m^2°C
Coefficient of heat exchange at the soil-environment border	χ_2	50	W/m^2°C
Coefficient of heat exchange at the soil-pipe border	χ_3	100	W/m^2°C
Initial temperature of the junction area	T_0	3	°C
Temperature at the soil-soil boundary	T^{e1}	3	°C
Temperature at the soil-environment boundary	T^{e2}	5	°C
Temperature at the pipe boundary	T^{e3}	80	°C
Given degree of blackness	ε	0.76	-

Table 2. Thermophysical Properties of the Soil

Properties	Designation	Value	Dimensionality
Coefficient of thermal conductivity	λ	1.6735	W/m °C
Density	ρ	1950	kg/m^3
Heat capacity	c	833.76	J/kg °C

As a result of numerical calculations, the distribution of temperatures and isotherms of the soil under the thermal influence of the pipe for different periods of time is obtained. The dependence of the distribution of the soil temperature field on the spatial coordinates is shown in Figs. 6 and 7.

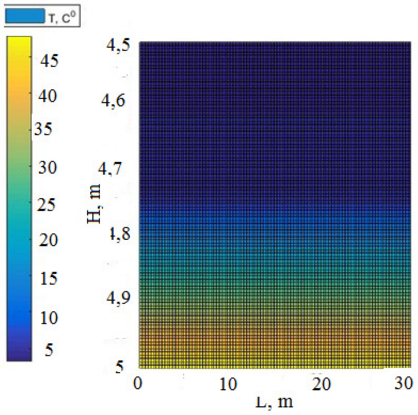

Fig. 6. Dependence of temperature distribution on spatial coordinates during the thermal influence of the pipe per hour.

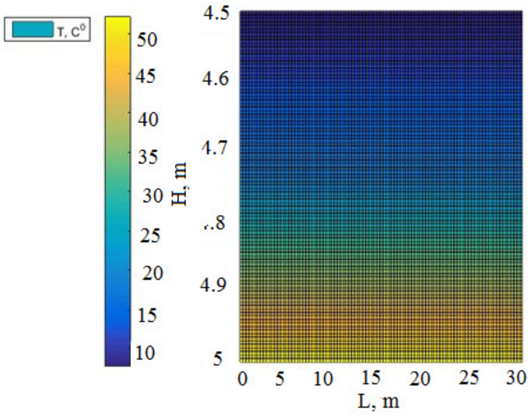

Fig. 7. Dependence of temperature distribution on spatial coordinates during the thermal influence of the pipe per 10 hours.

The analysis of the drawings demonstrates that heat spreads from the pipeline to the soil surface over time, and more intense heating is observed both near the pipeline and in the body of the soil massif.

3. CONCLUSIONS

1. An algorithm and a PC program for calculating the one-dimensional soil temperature field without taking into account the influence of the phase transition of moisture in the soil pores during seasonal freezing and thawing using the finite difference method have been developed.
2. On the basis of numerical calculations, the dependence of the temperature change on time and on the depth of the soil massif has been obtained. It has been established that the amplitude of fluctuations in the temperature regime decreases with depth from the soil surface.
3. It has been established that the delay of the temperature maximum and temperature minimum relative to the fluctuation of the annual conditional temperature of the atmospheric air is greater, the deeper the calculated soil mark is. The resulting effect occurs due to the thermal inertia of the soil and depends on its type and properties.
4. Mathematical modelling of the heat transfer process in the soil layer, on one boundary of which heat exchange occurs with the environment, and on the other with the hot water pipeline, has been carried out. An algorithm and a PC program have been developed to calculate the temperature field of the soil.
5. As a result of numerical calculations, the dependence of the distribution of the temperature field of the soil on spatial coordinates has been established, the analysis of which demonstrates that over time heat spreads from the pipeline to the surface of the soil, and over time more intense heating occurs both near the pipeline and in the body of the soil massif.

REFERENCES

1. Plum, R.L., & Esrig, M. J. (1969). Some Temperature Effects on Soil Compressibility and Porewater Pressure. *Highway Research Board*. *SpRpt, 103*, 213–242.
2. Campanella, R.G., & Mitchell, J.K. (1968). Influence of Temperature Variations on Soil Behavior. *J. Soil Mechanics and Foundations Division*, *94*, 709–734.
3. Laloui, L. (2001).Thermo-Mechanical Behavior of Soils. *Revue Francaisedegenie Civil, 5*, 809–843.
4. Ivanik, O.M., & Lavrenyuk, M.V. (2008). Factors Provoking Strained and Deformed State in the System of Geological Medium-Pipeline in Cryolithozone and their Quantitative Assessment (Numerical Data Based on Computer Modeling). *Geoinformatika, Ukraine, 1*, 53 –59.
5. Kovalchuk, V., Hnativ, Y., Luchko, J., & Sysyn, M. (2020). Study of the Temperature Field and the Thermo-elastic State of the Multilayer Soil-Steel Structure. *Roads and Bridges – Drogi i Mosty, 19* (1), 65–78.
6. Chornyi, S.G. (2018). *Assessment of Soil Quality: Study Guide*. Mykolaiv, Ukraine: MNAU.
7. Shutenko, L.M., Rud, O.G., Kichaeva, O.V. (2017). *Soil mechanics and Foundations: A Textbook.* Kharkiv, Ukraine: O.M. Beketov KhNUMG.
8. Remez, N., Dychko, A., Kraychuk, S., Ostapchuk, N., Yevtieieva, L., & Bronitskiy, V. (2018). Simulation of Seismic Explosion Waves with Underground Pipe Interaction. *Latvian Journal of Physics and Technical Sciences*, *55* (3), 27–33. DOI: 10.2478/lpts-2018-0018.

9. Tolstoy, M.I., Gozyk, A.P., Reva M.V. (2006). *Fundamentals of Geophysics*. Kyiv, Ukraine: KNU.
10. Shkolny, E.P. (1997). *Physics of the Atmosphere.* Odesa, Ukraine: Vipol.
11. Remez, N.S., Kiselyov, V.B., Dychko, A.O., & Minaieva, Y.Y. (2022). *Numerical Methods of Solving Technical Problems.* Odesa, Ukraine: "Helvetika" Publishing House.

LATVIAN JOURNAL OF PHYSICS
AND TECHNICAL SCIENCES
2023, N 4

DOI: 10.2478/lpts-2023-0025

APPLICATION OF FWM-BASED OFC FOR DWDM OPTICAL COMMUNICATION SYSTEM WITH EMBEDDED FBG SENSOR NETWORK

J. Braunfelds[1,2*], K. Zvirbule[1], U. Senkans[1], R. Murnieks[1,2],
I. Lyashuk[1], J. Porins[1], S. Spolitis[1,2], V. Bobrovs[1]

[1]Institute of Telecommunications,
Riga Technical University,
12 Azenes Str., LV-1048, Riga, LATVIA
[2]Communication Technologies Research Centre,
Riga Technical University,
12 Azenes Str., LV-1048, Riga, LATVIA
*e-mail: janis.braunfelds@rtu.lv

Four-wave mixing optical frequency comb fibre-based setups (FWM-OFCs) have the potential to improve the combined dense wavelength division multiplexed passive optical network (DWDM-PON) and fibre Bragg grating (FBG) temperature sensors network providing easier application, broader technological opportunities for network development, and energy efficiency by substituting a power-demanding laser array.

In this research, OFCs are generated for the purpose of combined network application of DWDM-PON and FBG optical sensors. The paper also investigates compatibility scenarios with OFCs in such systems. The mathematical simulation model has been developed and the performance of FWM-OFC based 8-channel 50 GHz spaced non-return-to-zero on-off keying (NRZ-OOK) modulated DWDM-PON transmission system, operating at 50 km single-mode fibre (SMF) with a bit rate of at least 10 Gbps embedded with 7 FBG optical temperature sensors, has been studied. As it is shown, FWM application results in OFC source that has fluctuations of the individual comb tones of less than 3 dB in power, and with an extinction ratio of about 33 dB for operation range of 192.9–193.25 THz, acting as a unified light source for all the data transmission channels. Embedded FBG optical sensors network causes negligible 0.3 dB power penalty.

Keywords: *Dense wavelength division multiplexed passive optical network (DWDM-PON), fibre Bragg grating (FBG) optical sensors, four-wave mixing (FWM), highly nonlinear optical fibre (HNLF), optical frequency combs (OFC), non-return-to-zero on-off keying (NRZ-OOK).*

1. INTRODUCTION

Nowadays, multichannel fibre optical data transmission systems have become the standard of the Internet, e-commerce, multimedia, and data operation. Systems of this type encounter channel crosstalk and their performance degrades by the effect of four-wave mixing (FWM), where non-linear interactions between channels are observed [1]–[4]. FWM is an effect when two or more different signals with different frequencies propagate next to each other, and due to this reason, new carriers are generated. However, solutions for the useful application of the FWM effect are being studied, for instance, the generation of optical frequency combs [1], [5], [6].

OFC generators based on FWM have the potential to improve the energy efficiency of wavelength division multiplexed (WDM) fibre optical transmission systems. One of the main reasons for this is that one OFC light source can provide multiple data transmission carriers substituting a power-demanding laser array that also requires synchronization among the lasers. OFC generators can also be used in spectroscopy [7]–[9], radio-frequency photonics [7], [10], quantum optics [7], [11], optical clocks, and microwave systems [12], [13]. Spatial microresonators (crystalline, microsphere, microrod, microbubble), microresonators on a chip (toroidal, disk, ring, etc.) [14]–[16], and fibre-based setups [17]–[19] might be used to generate OFC. Even though spatial microresonators and integrated microresonators have been widely studied as WDM-PON light source, fibre-based setups (e.g., our demonstrated FWM-based OFC) have the advantage to provide spectrally flat comb and narrow channel spacings or so-called free spectral range (FSR) [20] (based on 10–100 GHz corresponding to ITU-T G.694.1 dense WDM passive optical network (DWDM-PON) frequency grid [21]), which is more difficult to obtain, for example, with microspherical resonators.

Fibre Bragg grating (FBG) sensors are one of the most promising fibre optical sensors for different environmental measurements. FBG sensors have multiple advantages that can be applied in different areas. Some of these advantages are small size and weight [22], corrosion resistance [23], immunity to electromagnetic interference (EMI) [23], [24], the possibility to withstand direct embedment into the composite material, together with rein-forced fibres, as well as the potential to multiplex several optical sensors within the same optical fibre [23], [25], [26]. FBGs are applied for vast solutions, for instance, in offshore platforms – to monitor ship collisions and ocean wave loads, while providing lasting performance without significant reduction, as do conventional strain gauges [27], [28]. Also, FBGs are highly topical for structural health monitoring (SHM) applications, such as civil engineering (e.g., roads [29], bridges [30], dams, tunnels and roads [31]), aerospace, energy applications [25], [27], [32], [33], oil and gas industry [34], biomedicine [35], [36], etc. Fibre optic sensors can be used to measure, for example, temperature [37]–[39], strain [37], [40], [41], pressure [41], [42], vibration velocity [43], and displacement [43]. Single-mode fibre (SMF) and multimode fibre (MMF) can be used for fibre optic sensor construction. Yet single-mode fibres have a smaller core (approximately 10 μm in diameter) and they are more strain sensitive than multimode optical fibres [25].

FBG working principle can be described with a mathematical equation:

$$\lambda_B=2\times n_{eff}\times\Lambda, \quad (1)$$

where λ_B is Bragg wavelength, n_{eff} is effective refractive index of the optical fibre in the region of the Bragg grating and Λ is grating period [28].

FBG optical sensors are typically used when strain, pressure and temperature sensing is necessary, for instance, in hostile environments with temperatures exceeding 250 °C (thermal well applications). Bragg grating-based sensing systems are typically used in WDM transmission systems, when wavelength multiplexing of various sensors on single optical line might be required [34], [36], [37]. All of the information mentioned above shows the topicality of the FBG optical sensors and their integration with WDM data transmission systems.

Considering that fibre optical data transmission system like DWDM-PON interconnection with optical sensor system is topical [26], [44], [45] and the search for new improvements and solutions continues, the authors propose the application of FWM-OFC [1], [5], [6] as a light source to provide power efficiency to such a system. To the best of authors' knowledge, studies on FWM-OFC implementation as a light source in collaboration with FBG optical sensor network and DWDM-PON system have not been performed. This article shows that such realization can provide more straightforward application, broader technological opportunities for network development, and greater energy efficiency with a reduced light source amount required.

The remainder of the manuscript is structured as follows: Section II describes the construction and analysis of the simulation model where FWC-OFC is developed and integrated into the DWDM-PON system in collaboration with the FBG optical sensor network. Section III discusses the simulation results of the OFC application in fibre optical communication systems, showing received signal waveforms, reflected signal of the FBG optical sensors, eye diagrams and BER versus received optical power chart. More specifically, this section shows negligible power penalty at the BER threshold level of 1×10^{-12} (only 0.3 dB) between B2B and 50 km long transmission line on the received optical power and BER comparison. Finally, section IV gives a brief summary of the simulative results and concludes the article, stating that the BER of the worst-performing channel in the 8-channel DWDM-PON system is 9.4×10^{37}.

2. CONSTRUCTION AND ANALYSIS OF THE SIMULATION MODEL

The simulation model aims to evaluate the developed comb source and the performance of the FWM-OFC based DWDM transmission system with an integrated FBG sensor network. The proposed system includes the following main blocks – optical line terminal (OLT), optical distribution network (ODN), optical network units (ONUs).

2.1. FWM-OFC Generation for the Requirements of the DWDM-PON Data Transmission Channels

We have created the simulation setup of the combined system using Synopsys OptSim optical system design tool. Application framework allows generating coherent optical communication systems (Polarization multiplexed-quadrature phase shift keying, Polarization multiplexed-binary phase-shift keying, etc.), using advanced modulation for-mats (Differential Quadrature Phase-Shift Keying, Doubinary, etc.), ensuring optical amplification (Erbium Doped Fibre Amplifier, Raman, Semiconductor Optical Amplifier, etc.), different passive optical network configurations and so on. Time and frequency domain split-step configurations with an extensive library of predefined as well as authors' defined components are necessary to develop and generate complex optical systems as described in the following paragraphs [46]. From the simulation perspective, the time domain split-step (TDSS) algorithm was used to simulate the signal propagation in optical elements, especially fibre. The principle of this algorithm has been already well explained in our previous research [50].

Two continuous-wave (CW) pump laser sources with +20 dBm output power and 50 GHz channel spacing according to the ITU-T G.694.1 recommendation [21], optical power coupler (PC), and 2 km long highly nonlinear optical fibre (HNLF) are used to develop an OFC source (see Fig. 1).

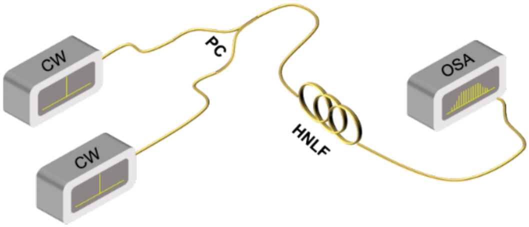

Fig. 1. FWM-OFC generation setup.

We have set HNLF fibre parameters like the attenuation coefficient, dispersion coefficient, effective area, nonlinear index and others based on the datasheet from real commercial OFS HNLF Standard fibre (please see Table 1).

Table 1. The Main Parameters of the Chosen Fibre Types at 1550 nm Reference Wavelength

Parameters	Fibre types	
	OFS Standard HNLF	Corning SMF-28 (ITU-T G.652D)
Attenuation (dB/km)	0.8	0.18
Dispersion (ps/(nm·km))	-0.027	16
Dispersion slope (ps/(nm^2·km))	0.019	0.092
PMD (ps/√km)	0.20	0.04
Effective area (μm^2)	11.6	85
Nonlinear index (W×km)$^{-1}$	11.5	1.27

The first and second pump laser source (depicted in Fig. 1 as CW_1 and CW_2) are anchored to central frequencies of 193.1 and 193.15 THz, respectively. Pump laser parameters that can affect the generation of OFC carriers are signal phase, which was set to random, and realistic noise parameters as relaxation oscillation peak frequency and peak overshoot. The number of comb carriers and their peak power are varying depending on the output power of CW pump lasers and the length of HNLF fibre. For instance, as it was observed, if the output power of pump CW lasers is too low (e.g., 0 dBm) and HNLF fibre length is too short (e.g., 0.5 km), the number of newly generated optical carriers is limited. However, if the output power of the CW is too high (e.g., 25 dBm) and HNLF fibre is too long (e.g., 2.5 km), the carriers are not formed evenly. HNLF fibre length has an important role in OFC generation based on the FWM effect. The nonlinear length of the fibre is smaller than the dispersion length by orders of magnitude, and this fact is important from the FWM point of view – for smaller fibre lengths nonlinear effects dominate over the dispersion effects, which is an advantage for FWM. It is an advantage in terms of dispersion – more dispersion means less efficiency of the FWM effect. Additionally, high CW pump power leads to unwanted broadband noise via Raman scattering and parametric vacuum noise amplification [17]–[19]. Therefore, it is vital to determine and evaluate the optimal parameters for the FWM-based OFC comb light source to ensure the stable operation of the system. Optimal parameters (pump laser output power and HNLF length) are those, which provide the smallest power variation range among peaks of OFC carriers. It is essential to have the lowest possible OFC fluctuation value for a couple of reasons. The fluctuations of the OFC source directly affect the performance of separate data channels, for instance, if the peak power of a particular channel is lower, then the resulting performance indicator as BER can have higher values compared to neighbouring channels and ultimately be higher than the chosen BER threshold. On the other hand, looking at the WDM-PON network as a whole, then channels with higher power may induce more crosstalk into neighbouring channels. However, for the data transmission, we have chosen eight optical carriers in that frequency range, where the average optical power of the peaks is the highest, also having the smallest fluctuations of optical peak power. It is important to have a peak power of OFC carriers as high as possible to achieve better performance of individual channels and the network as whole. As shown in Fig. 2, optical power fluctuations between all OFC peaks are observed, and extinction ratios depend on the CWs laser output power as well as the length of the HNLF.

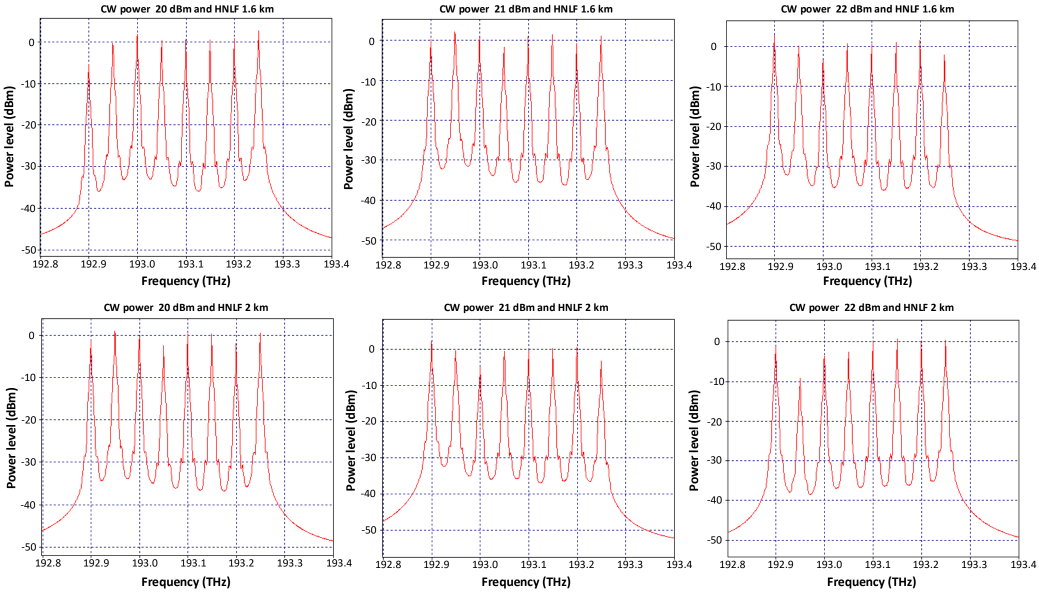

Fig. 2. Measured optical spectrum on the AWG MUX output of FWM-based OFC for different CW pump powers and HNLF fibre lengths.

For HNLF fibre with a length of 1.6 km, the fluctuations of optical frequency comb peaks are in the range of -4.5 to 3 dBm, -2 to 2 dBm, and -4 to 3 dBm, where CW power is 20, 21, and 22 dBm, respectively.

For fibre length of 2 km, the fluctuations of optical frequency comb peaks are in the range of -1.5 to 2 dBm, -5 to 2 dBm, and -8.5 to 1 dBm for CW power of 20, 21, and 22 dBm, respectively. All OFCs have the same extinction ratio of 33 dB, the same number of optical carriers, and a free spectral range (FSR) of 50 GHz.

By comparing the scale of fluctuations and average comb peak power, the optimal pumping lasers (CW1 and CW2) output power was chosen as +20 dBm and HNLF fibre length - 2 km, to generate the OFC with the lowest fluctuations of 1.5 dBm and highest average peak power of 2 dBm.

2.2. Development of DWDM-PON System with Integrated FBG Optical Sensor Network

Output of the OFC source is connected to the input of a 50 GHz spaced arrayed waveguide grating multiplexer (depicted in Fig. 3 as AWG MUX). AWG MUX and AWG demultiplexer (DEMUX) with the same optical parameters are used in this setup to separate and combine 8 channels in the frequency band from 192.9 THz to 193.25 THz. The 3-dB bandwidth of each AWG channel is 50 GHz.

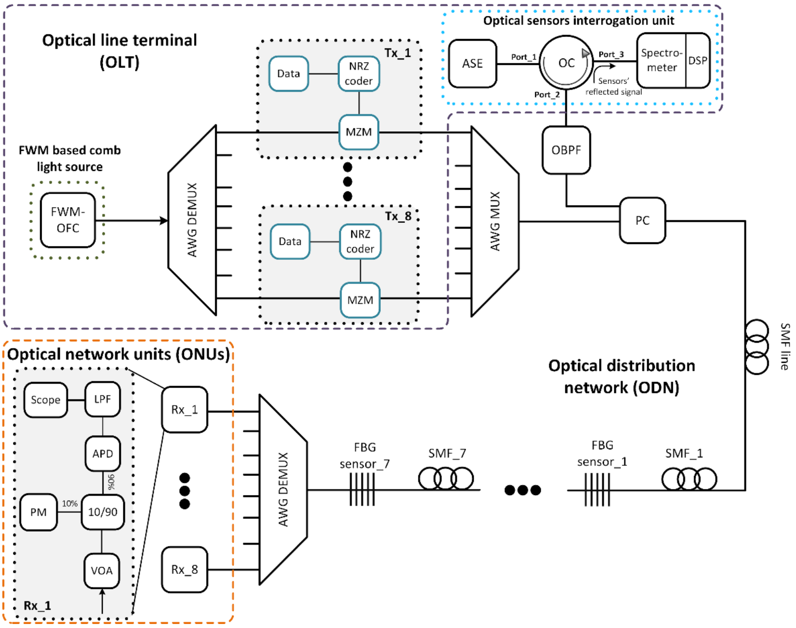

FWM-OFC – Four-wave mixing optical frequency comb; AWG MUX/DEMUX – Arrayed waveguide grating multiplexer/demultiplexer; Tx – Transmitter; NRZ – Non-return-to-zero; MZM – Mach-Zehnder Modulator; OC – Optical circulator; OBPF – Optical band-pass filter; PC – Optical power coupler; ASE – Amplified spontaneous emission source; DSP – Digital signal processor; SMF – Single mode fibre; FBG – Fibre Bragg grating; VOA – Variable optical attenuator; 10/90 - Optical power splitter with ratio 10/90%; APD – Avalanche photodiode; LPF– Low-pass filter; PM – Power meter; Rx – Receiver.

Fig. 3. The simulation model of 8-channel DWDM-PON system based on FWM OFC source, integrated 7 FBG temperature sensor network and FWM multi-wavelength light source.

OLT also includes transmitter blocks (depicted in Fig. 2 as Tx_1 to Tx_8) where each has data generator, non-return-to-zero (NRZ) coder, and Mach-Zehnder modulator (MZM) with 20 dB extinction ratio and insertion loss of 4 dB. An optical power coupler (PC) is used to combine all 8 data transmission channels and the signal for the FBG sensor network. The interrogation unit block transmission part of the optical sensor consists of broadband amplified spontaneous emission (ASE) light source, which has an optical output power of +23 dBm and 20-dB bandwidth of 48.1 nm (5.607 THz). From our test results, this configuration for the ASE source enables acceptable received optical power level from the reflected signal of the FBG sensors network where quasi-distributed optical sensor scheme is applied in 50 km optical fibre line.

This is discussed in more detail in next paragraphs of this article. 3-port optical circulator (OC) is used to separate the optical transmission directions – FBG reflected signal from the transmitted data and ASE signal. The optical signal of the ASE broadband light source is transmitted from the OC input port (Port_1) to the common port (Port_2) and then a tunable optical band-pass filter (OBPF) with 800 GHz 3-dB bandwidth (in frequency band of 193.50–194.30 THz). OBPF is used to filter the necessary spectral band for the operation of the FBG sensor network, where such parameters for the OBPF were chosen according to the spectral bandwidth of the ASE light source and FBGs position within the available optical spectrum.

The reflected optical signal from all FBG sensors is sent back through the circulator's common port (Port_2) and forwarded to the output port (Port_3). FBG sensor reflected signal is received at the optical sensor interrogation unit, where optical spectrometer block and digital signal processor (DSP) are used to detect the central frequency of the reflected signal and by knowing the temperature coefficient (frequency or wavelength shift for 1 °C) calculate the temperature variations.

PC coupled signal is transmitted to the 15 km SMF having an attenuation coefficient of 0.18 dB/km and dispersion coefficient of 16 ps/nm/km set based on the datasheet parameters from real commercial Corning SMF-28 fibre corresponding to ITU-T G.652D requirements. The next main part of the transmission scheme is an optical distribution network (ODN) with 7 optical FBG temperature sensors.

These FBG sensors contain the experimentally measured optical and response parameters. Amplitude-frequency response (see Figs. 4 and 5) and technical parameters (central frequency, full-width half-maximum (FWHM)), etc.) of commercial FBG sensor reflected and transmitted signals were measured in the laboratory and implemented within simulation setup. SLED broadband light source, 3-port optical circulator, spectrometer, and FBG sensor components were used for laboratory measurements of these parameters. As for reflected spectrum measurements – the components are connected the same as shown in Fig. 3 (in optical sensor interrogator unit part), but for the transmitted signal spectrum measurements – the spectrometer is connected with the FBG sensor output. Central frequencies and FWHM values of FBG sensor were determined based on the measured spectrum of the FBG reflected signals.

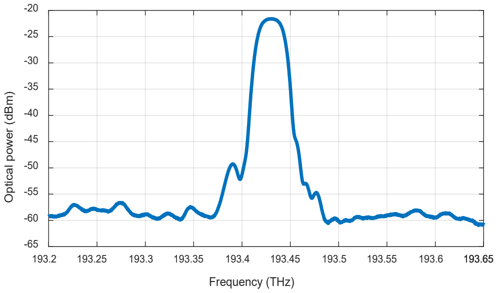

Fig. 4. Reflected signal spectrum of the FBG optical sensor (laboratory temperature 25 °C).

These spectral measurements of the used FBG sensor are shown in Table 2. All 7 implemented FBG sensors have the same (except reference wavelength) optical parameters.

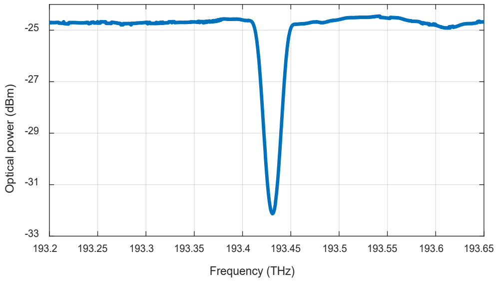

Fig. 5. Transmitted signal spectrum of the FBG optical sensor (laboratory temperature 25 °C).

The developed simulation model can be widely used and particular FBG optical temperature sensors can be substituted with different ones (for example, strain, pressure, displacement, etc. sensors) in a situation where it is necessary. However, the maximum available number of optical sensors available for implementation in such a combined system is limited to the bandwidth of the optical light source – its optical power level, channel spacing between optical sensors as well as the optical bandwidth for each and every sensor channel and the distance from the optical sensor interrogation unit. Also, the WDM-PON system and its configuration – number of data channels, their positioning in the optical spectrum, etc. – limits the integration of the optical sensors. All these parameters have to be calculated and adjusted in order to sustain the proper performance of both systems while providing the necessary application of each of them.

Table 2. The Main Parameters of the Used FBG Temperature Sensor

Parameters	Value	
	Wavelength	Frequency
Operation temperature range	-40 to +150 °C	
Reflectivity	88.73 %	
FWHM	0.22 nm	27.448 GHz
Temperature coefficient (frequency or wavelength shift for 1 °C)	9.6 pm/1 °C	1.198 GHz/1 °C
Reference wavelength or frequency used in the simulation setup	1548.52; 1547.72; 1546.92; 1546.12; 1545.32; 1544.53; 1543.73 nm	193.60; 193.70; 193.80; 193.90; 194.00; 194.10; 194.20 THz

Figure 6 shows the relevance between temperature and frequency curve for the implemented FBG sensor in order to understand the correlation between the temperature and frequency shift. The curve is based on the commercial (Technica T840) FBG sensor calibrated datasheet data. Then a linear approximation method is used for a more precise evaluation of the acquired data. The authors developed the mathematical linear function for this optical FBG temperature sensor, where the correlation of the temperature and frequency can be expressed as follows:

$$T = -764.57 \times F + 1.4791 \cdot 10^{-5}, \qquad (2)$$

where T-measured temperature (°C) and F – measured frequency of the FBG sensor (THz).

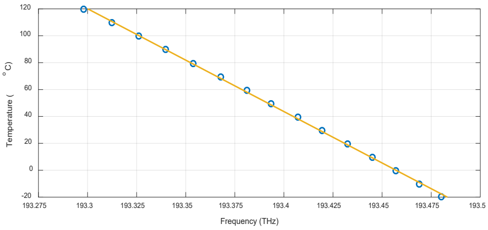

Fig. 6. The correlation of the temperature and frequency shift of the commercial FBG temperature sensor.

The length of 7 SMF spans between each FBG optical sensor is 5 km, whereas FBG sensors are located at 20th, 25th, 30th, 35th, 40th, 45th, and 50th km of the optical distribution network. Such positioning provides quasi-distributed FBG optical sensing applications, where optical sensors are implemented with a certain distance or evenly in the whole transmission media [47]–[49]. It is also important to note that the optical signal necessary for the operation of FBG optical sensors is transmitted twice through the ODN – firstly together with dense WDM-PON data transmission channels and then reflected back, being received at the optical sensor interrogation unit. All the related parameters for the acceptable system setup development can be adjusted and are mentioned in this article. FBG temperature sensors were set in the frequency band between 193.60 THz and 194.20 THz having channel spacing of 100 GHz between each and every one of them. Such channel spacing was chosen considering the measured spectral bandwidth of each FBG (0.22 nm at FWHM) and the potential temperature range variation to avoid spectral overlapping. The output of FBG sensor_7 is connected with the AWG demultiplexer.

The optical network units (ONUs) section is realized as receiver blocks (Rx_1 to Rx_8). The AWG demultiplexed signal is transmitted to a variable optical attenuator (VOA) and optical power splitter with a 10/90 splitting ratio for optical power level monitoring, enabling data transmission system BER curve measurements. The 10 % port of the power splitter is connected with an optical power meter, and 90 % port is connected with an avalanche photodiode (APD), which has a sensitivity of -20 dBm at reference $BER \leq 10^{-12}$. On the output of APD, the received electrical signal is filtered by Bessel low-pass filter (LPF) having a 7.5 GHz 3-dB bandwidth to reduce the noise. The filtered signal is then sent to the electrical scope to evaluate the waveform quality, e.g., to show eye diagrams, electrical spectrum, and estimate BER. Here the BER of the received signal is estimated analytically based on the eye quality.

3. RESULTS

The spectrum of the reflected signal of the 7 FBG sensor network is measured with an optical sensor interrogator unit spectrometer, (see Fig. 7). As one can see in the measured spectrum, the central reflected frequencies of the sensor network are 193.60, 193.70, 193.80, 193.90, 194.00, 194.10, and 194.20 THz. The central frequencies are the same as previously mentioned, considering that all sensors of the simulation model are configured to the reference temperature +25 °C. The main reason for the slanted reflected signal spectrum of the FBG sensor network (Fig. 6) is the attenuation of optical fibre. As we are measuring the reflected FBG signal, it experiences double the attenuation of optical fibre (100 km in total).

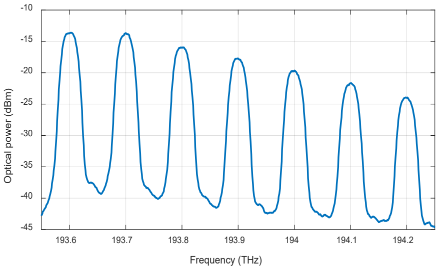

Fig. 7. The reflected signal spectrum of the FBG sensor network.

The optical signal spectrum (measured at the input of AWG DEMUX) of the simulated model where 8 data channels of the

DWDM-PON transmission system (left side) are collaborated with 7 FBG temperature sensor network transmitted signal (right side) is shown in Fig. 8. AWG DEMUX acts as a filter and blocks the signal of the ASE; therefore, it is not received by the ONUs. There is no visual interference, overlapping, and signal degradation between both systems (8channel DWDM-PON and 7 FBG sensors), see Fig. 8.

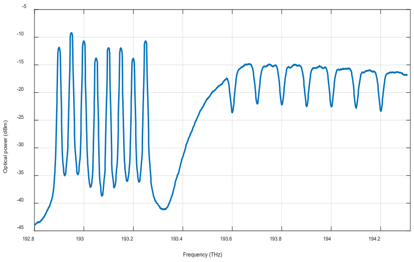

Fig. 8. The optical spectrum at AWG DEMUX input.

We chose the worst-performing data transmission channel (4th) in terms of the BER of an 8-channel DWDM-PON transmission system to analyse the performance of the overall DWDM system. Figure 9 shows a signal waveform of the received 10 Gbps signal after 50 km SMF transmission. As one can see in Figs. 9 and 11, the bit pattern is clearly visible with the impact of chromatic dispersion, leading to a pulse broadening. The time window of 10 ns is chosen to represent the bit sequence in a way understandable to the reader. This signal has passed not only the 50 km of SMF fibre but also 8 FBG sensors, from which no significant signal degradation effects can be observed.

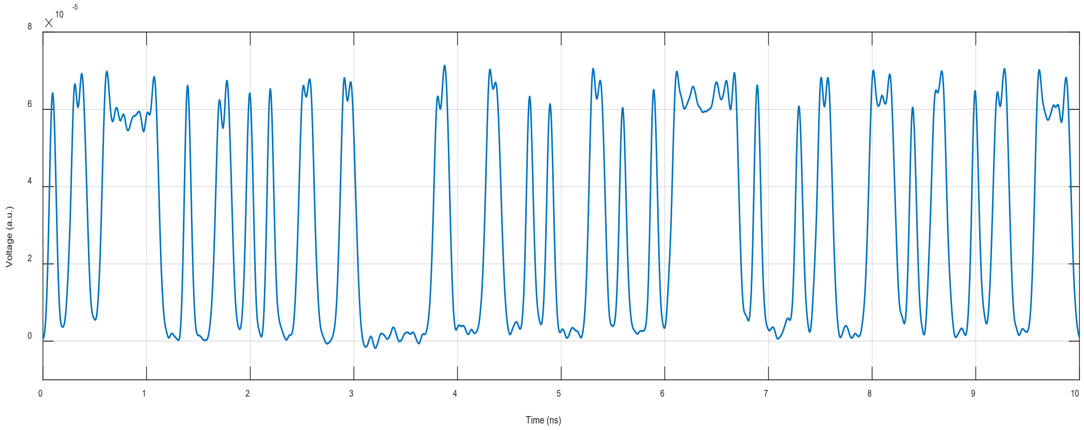

Fig. 9. The received signal 10 Gbps NRZ waveform of the 4th channel after 50 km long SMF transmission.

As shown in Figs. 10 and 11, the eye diagrams of the 4th data transmission channel in the back-to-back (B2B) configuration (Fig. 10) and after 50 km long SMF transmission (Fig. 11) are widely open, and error-free transmission is calculated. The B2B configuration also includes the optical sensor network, but the SMF line and SMF_1SMF_7 are set to 0 km.

For B2B transmission, the obtained BER for the worst-performing channel is 8×10^{-67}, and after 50 km long SMF line the obtained BER is 9.4×10^{-37}.

The eye diagrams are wide open and, therefore, the transmission of 10 Gbps NRZ-OOK signal can be considered as error-free.

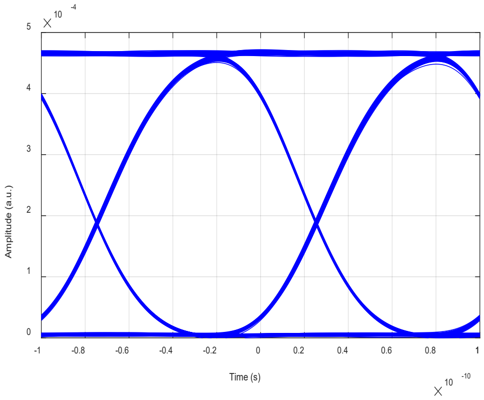

Fig. 10. The eye diagram of the worst-performing data channel in B2B configuration.

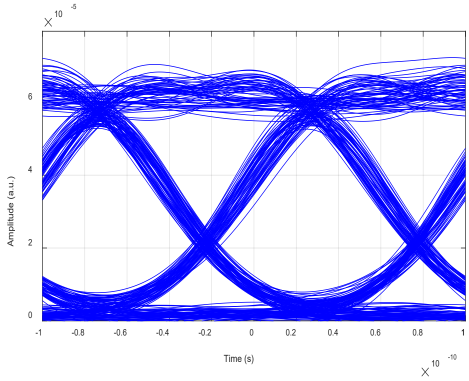

Fig. 11. The eye diagram of the worst-performing data channel after 50 km long transmission line.

We measured the BER versus received optical signal power (see Fig. 12) to understand the impact of a 50 km long SMF transmission line on the created mathematical simulation model.

Typical BER values would vary between the systems due to the differences in configuration, components, parameters, and so on. For such a collaborated system model, where the optical sensor system and dense WDM-PON system are merged, allowed BER should be at least <10^{-9}, which is typically to be considered as a BER threshold for error-free transmission [51]–[53]. In our research, this goal is accomplished and even lower BER values are estimated (for example, 10^{-37}) yet it is not an easy task to calculate precisely such small BER values; thus, the eye diagrams (which are wide open and even in our results) also have to be inspected.

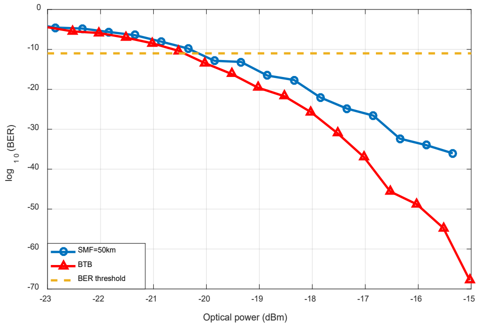

Fig. 12. BER versus the received optical signal power of 10 Gbps 8-channel DWDM PON data transmission system and 7 FBG sensors network, in the case of B2B and 50 km SMF configurations.

Here a strong correlation between B2B and a 50 km long transmission line is observed. The power penalty at the BER threshold level of 1×10^{-12} is negligible (only 0.3 dB). This power penalty introduced is mainly due to the fibre chromatic dispersion.

4. CONCLUSIONS

FWM-OFC can reduce the overall expenses of the proposed combined fibre optical DWDM transmission system and FBG temperature sensor network. The FWM-based OFC source provides an energy-efficient solution due to the fewer light sources required to ensure multiple data transmission channels. Only two CW pump light sources and one NHLF fibre are necessary to power the 8-channel DWDM-PON data transmission system. The OFC generated through FWM exhibits fluctuations of individual comb tones of less than 3 dB in power, the average peak power of 0 dBm, and an extinction ratio of about 33 dB for an operating range of 192.9–193.25 THz. The created shared light source powers all data transmission channels. A spectrally efficient configuration has been applied and calculated, as the minimum channel spacing between the DWDM channels, optical sensor channels, as well as between both systems (DWDM-PON and FBG sensors) has been presented. Thereby, other critical applications (for example, applications in Structural Health Monitoring (SHM)) were positioned in the available frequency spectrum. This research proved a successful realization of the FWM-based OFC source in the simulation model and its implementation in a 10 Gbps 8-channel DWDM-PON optical transmission system with an integrated 7 FBG temperature sensor network. Successful integration of FWM-based OFC source is confirmed by the fact that interference between DWDM-PON and FBG sensor networks is still negligible. The measured BER value of the worst-performing channel in this 8-channel DWDM-PON system is 9.4×10^{-37}, thus demonstrating the stable operation of the system. From the acquired results and all the significant parameters and components discussed, the authors can state that such a configuration and fundamental information can be applied and used to introduce multiple benefits while developing the optical network. Some of such benefits are easier application, broader optical network technological opportunities, and greater energy efficiency (with the reduced light source amount required). The proposed solution ensures collaboration opportunities between the optical sensing applications and data transmission solutions, as well as further research capabilities in the field of the WDM/DWDM-PON and optical sensor collaborated systems that utilize such OFC technologies.

ACKNOLEDGEMENT

The research has been funded by the European Regional Development Fund (ERDF) postdoctoral research project No. 1.1.1.2/VIAA/4/20/659, ERDF project No. 1.1.1.3/18/A/001 (PVS 3912.6.2), and the Doctoral Grant programme of Riga Technical University in Latvia. The funding source did not have any involvement regarding the collection, analysis and interpretation of the data, nor with the writing and publication of the article.

REFERENCES

1. Bhatia, R., & Bhatia, S. (2020). Responsiveness of FWM with Fraction of Planck HOD Parameters in Presence of Intensity Dependent Phase Matching Factor in Optical Transmission. *International Conference on Intelligent Engineering and Management (ICIEM),* 142–147. https://doi.org/10.1109/ICIEM48762.2020.9160075.
2. Olonkins, S., Spolitis, S., Lyashuk, I., & Bobrovs, V. (2014). Cost Effective WDM-AON with Multicarrier Source Based on Dual-Pump FOPA. In 6th International Congress on Ultra Modern Telecommunications and Control Systems and Workshops (ICUMT), (pp. 23–28). October 2014, Russia.
3. Ivaniga, P., & Ivaniga, T. (2020). Mitigation of Non-Linear Four-Wave Mixing Phenomenon in a Fully Optical Communication System. *Telkomnika, 18*, 2878–2885. http://dx.doi.org/10.12928/telkomnika.v18i6.16136.
4. Keiser, G. (2008). Optical Fibre Communications (4th ed.). Tata McGrawHill Publishing Co. Ltd.
5. Sharma, N., Singh, H., & Singh, P. (2020). Mitigation of FWM in the Fibre Optic DWDM System by using Different Modulation Tech-niques and Optical Filters. *5th International Conference on Communication and Electronics Systems (ICCES)*, (pp. 343–348). Coimbatore, India, 2020. https://doi.org/10.1109/ICCES48766.2020.9138080.
6. Selvamani, A., & Sabapathi, T. (2011). Suppression of Four Wave Mixing by Optical Phase Conjugation in DWDM Fibre Optic Link. *Electronics and Control Engineering*, *2011*, 95–99. 10.1109/ICONRAEeCE.2011.6129821.
7. Anashkina, E.A., Marisova, M.P., Andrianov, A.V., Akhmedzhanov, R.A., Murnieks, R., Tokman, M.D., … & Bobrovs, V. (2020). Microsphere-Based Optical Frequency Comb Generator for 200 GHz Spaced WDM Data Transmission System. *Photonics*, *7* (72), 1–16. https://doi.org/10.3390/photonics7030072.
8. Lin, G., Diallo, S., & Chembo Y. K. (2015). Optical Kerr frequency combs: Towards versatile spectral ranges and applications. In *17th International Conference on Transparent Optical Networks (ICTON)*, (pp. 1–4). Budapest, 2015. DOI: 10.1109/ICTON.2015.7193612.
9. Del’Haye, P., Schliesser, A., Arcizet, O., Wilken, T., Holzwarth, R., & Kippenberg, T. J. (2007). Optical Frequency Comb Generation from a Monolithic Microresonator. *Nature*, *450*, 1214– 1217. https://doi.org/10.1038/nature06401.
10. Liopis, O., Merrer, P. H., Bouchier, A., Saleh, K., & Cibiel, G. (2010). High-Q Optical Resonators: Characterization and Application to Stabilization of Lasers and High Spectral Purity Oscillators. *Proceeding of SPIE*, (pp. 10). San Francisco, 2010. https://doi.org/10.1117/12.847164.
11. Liang, W., Savchenkov, A. A., Matsko, A. B., Ilchenko, V. S., Seidel, D., & Maleki, L. (2011). Generation of Near-Infrared Frequency Combs from a MgF2 Whispering Gallery Mode Resonator. *Opt. Lett.*, *36*. https://doi.org/10.1364/OL.36.002290.
12. Savchenkov, A. A., Matsko, A. B., Ilchenko, V. S., Solomatine, I., Seidel, D., & Maleki, L. (2008). Optical Combs with a Crystalline Whispering Gallery Mode Resonator. *Phys. Rev. Lett.*, *101*, 093902. https://doi.org/10.1103/PhysRevLett.101.093902.
13. Savchenkov, A. A., Matsko, A. B., & Maleki, L. (2016). On Frequency Combs in Monolithic Resonators. *Nanophotonics*, *5*, 363–391. https://doi.org/10.1515/nanoph-2016-0031.
14. Braunfelds, J., Murnieks, R., Salgals, T., Brice, I., Sharashidze, T., Lyashuk, I., … & Bobrovs, V. (2020). Frequency Comb Generation in WGM Microsphere Based Generators for Telecommunication Applications. *Quantum Electronics*, *50*, 1043. https://doi.org/10.1070/QEL17409.

15. Anashkina, E.A., & Andrianov, A.V. (2021). Kerr-Raman Optical Frequency Combs in Silica Microsphere Pumped near Zero Disper-sion Wavelength. *IEEE Access*, *9*, 6729–6734. https://doi.org/10.1109/ACCESS.2021.3049183.
16. Andrianov, A.V., & Anashkina, E.A. Single-Mode Silica Microsphere Raman Laser Tunable in the U-Band and beyond. *Results Phys.*, *17*, 103084, 1–5. https://doi.org/10.1016/j.rinp.2020.103084.
17. Antikainen, A., & Agrawal, G. P. (2015). Dual-Pump Frequency Comb Generation in Normally Dispersive Optical Fibres. *J. Opt. Soc. Am. B*, *32*, 1705–1711. https://doi.org/10.1364/JOSAB.32.001705.
18. Myslivets, E., Kuo, B. P., Alic, N., & Radic, S. (2012). Generation of Wideband Frequency Combs by Continuous-Wave Seeding of Multi-Stage Mixers with Synthesized Dispersion. *Opt. Express*, *20*, 3331–3344. https://doi.org/10.1364/OE.20.003331.
19. Hänsel, W., Hoogland, H., Giunta, M., Schmid, S., Steinmetz, T., Doubek, R., … & Holzwarth R. (2017). All Polarization-Maintaining Fibre Laser Architecture for Robust Femtosecond Pulse Generation. *Appl. Phys. B*, *123*, 1–6. https://doi.org/10.1007/s00340-016-6598-2.
20. Ataie, V., Myslivets, E., Kuo, B. P.-P., Alic, N., & Radic, S. (2014). Spectrally Equalized Frequency Comb Generation in Multistage Parametric Mixer with Nonlinear Pulse Shaping. *J. Light. Technol.*, *32*, 840–846. https://doi.org/10.1109/JLT.2013.2287852.
21. ITU-T Recommendation G 694.1. (2002). *Spectral Grids for WDM Applications: DWDM Frequency Grid*. International Telecommunication Union, Telecommunication standardization sector of ITU, pp. 1–7, Geneva, Switzerland,.
22. Bohnert, K., Frank, A., Yang, L., Gu, X., & Müller, G. M. (2019). Polarimetric Fibre-Optic Current Sensor With Integrated-Optic Polarization Splitter. *J. Light. Technol.*, *37*, 3672–3678. https://doi.org/10.1109/JLT.2019.2919387.
23. Giurgiutiu, V. (2018). *Comprehensive Composite Materials*. II Elsevier. ISBN 9780081005347.
24. McKnight, M., Agcayazi, T., Ghosh, T., & Bozkurt, A. (2018). *Wearable Technology in Medicine and Health Care*. Academic Press. ISBN 9780128118108.
25. Giurgiutiu, V. (2020). Composites Science and Engineering, Polymer Composites in the Aerospace Industry (2nd ed.). Woodhead Publishing. ISBN 9780081026793.
26. Senkans, U., Braunfelds, J., Lyashuk, I., Porins, J., Spolitis, S., & Bobrovs, V. (2019). Research on FBG-Based Sensor Networks and Their Coexistence with Fibre Optical Transmission Systems. *Journal of Sensors*, *2019*, 1–13. https://doi.org/10.1155/2019/6459387.
27. Kim, M.H., & Lee, J.M. (2014). Woodhead Publishing Series in Electronic and Optical Materials, Sensor Technologies for Civil Infrastructures. *Woodhead Publishing*, *56*. ISBN 9781782422426.
28. Hayes, S.A., Swait, T.J., & Lafferty, A.D. (2015). *Composites Science and Engineering, Recent Advances in Smart Self-healing Polymers and Composites.* Woodhead Publishing. ISBN 9781782422808.
29. Braunfelds, J., Senkans, U., Skels, P., Janeliukstis, R., Salgals, T., Redka, D., … & Bobrovs, V. (2021). FBG-Based Sensing for Structural Health Monitoring of Road Infrastructure. *Journal of Sensors*, 1–11. https://doi.org/10.1155/2021/8850368.
30. Alamandala, S., Sai Prasad, R.L.N., Pancharathi, R., Pavan, V.D.R., & Kishore, P. (2021). Study on Bridge Weigh in Motion (BWIM) System for Measuring the Vehicle Parameters Based on Strain Measurement Using FBG Sensors. *Opt. Fibre Technol.*, *61*, 102440, 1–9. https://doi.org/10.1016/j.yofte.2020.102440.
31. Taheri, S. (2019). A Review on Five Key Sensors for Monitoring of Concrete Structures. *Construction and Building Materials*, *204*, 492–509. https://doi.org/10.1016/j.conbuildmat.2019.01.172.
32. Peters, K.J., & Inaudi, D. (2014). Electronic and Optical Materials, Sensor Technologies for Civil Infrastructures. *Woodhead Publishing, 55*. ISBN 9780857094322.

33. Ansari, F. (2009). *Civil and Structural Engineering, Structural Health Monitoring of Civil Infrastructure Systems.* Woodhead Publishing, ISBN 9781845693923.
34. Baldwin, C. (2018). *8-Fibre Optic Sensors in the Oil and Gas Industry: Current and Future Applications*. Opto-Mechanical Fibre Optic Sensors, Butterworth-Heinemann. ISBN 9780128031315.
35. Vadgama, P. (2001). Biomedical Sensors: Materials. *Encyclopedia of Materials: Science and Technology, Elsevier.* ISBN 9780080431529.
36. Tosi, D., Poeggel, S., Iordachita, I., & Schena E. (2018). *11-Fibre Optic Sensors for Biomedical Applications.* Opto-Mechanical Fibre Optic Sensors, Butterworth-Heinemann. ISBN 9780128031315.
37. Broughton, W. (2012). *Welding and Other Joining Technologies, Adhesives in Marine Engineering.* Woodhead Publishing. ISBN 9781845694524.
38. Subramanian, R., Zhu, C.L., Zhao, H., & Li, H.P. (2018). Torsion, Strain, and Temperature Sensor Based on Helical Long-Period Fibre Gratings. *IEEE Photonics Technol. Lett., 30*, 327–330. https://doi.org/10.1109/LPT.2017.2787157.
39. Velazquez-Gonzalez, J.S., Monzon-Hernandez, D., Martinez-Pinon, F., & Hernandez-Romano, I. (2017). Simultaneous Measurement of Refractive Index and Temperature Using a SPR-Based Fibre Optic Sensor. *Sens. Actuat. B-Chem.*, *242*, 912–920. https://doi.org/10.1016/j.snb.2016.09.164.
40. Gu, J., Kwon, D., Ahn, J., & Park, I. (2019). Strain sensor based on optical intensity change through the carbon nanotube embedded elastomer. In 20th International Conference on Solid-State Sensors *"Actuators and Microsystems & Eurosensors XXXIII" (TRANSDUCERS & EUROSENSORS XXXIII)*, (pp. 1716–1719). Berlin, Germany, 2019. https://doi.org/10.1109/TRANSDUCERS.2019.8808701.
41. Madan, A., Liu, O., Jiang, W., Wang, Y., Shum, P. P., & Hao, J. (2020). Carbon-steel tube surface mounted FBG sensors under high-temperature environment, part I: Polyimide coated and femtosecond laser written. In *IEEE 5th Optoelectronics Global Conference (OGC)*, (pp. 125–129). Shenzhen, China, 2020. https://doi.org/10.1109/OGC50007.2020.9260462.
42. Ran, Z., Liu, S., Liu, Q., Wang, Y., Bao, H., & Rao, Y. (2015). Novel High-Temperature Fibre-Optic Pressure Sensor Based on Etched PCF F-P Interferometer Micromachined by a 157-nm Laser. *IEEE Sens. J.*, *15*, 3955–3958. https://doi.org/10.1109/JSEN.2014.2371243.
43. Khadour, A., &Waeytens, J. (2018). *Civil and Structural Engineering, Eco-Efficient Repair and Rehabilitation of Concrete Infrastructures.* Woodhead Publishing. ISBN 9780081021811.
44. Mahawar, N., & Khunteta, A. (2019). Design and performance analysis of WDM optical Communication system with EDFA-DCF and FBG for dispersion compensation using 8x5 Gbps data rate. In *International Conference on Communication and Electronics Systems (ICCES)*, (pp. 431–435). Coimbatore, India, 2019. https://doi.org/10.1109/ICCES45898.2019.9002236.
45. Götten, M., Lochmann, S., Ahrens, A., Lindner, E., Vlekken, J., & Van Roosbroeck, J. (2020). 4000 Serial FBG Sensors Interrogated with a Hybrid CDM-WDM System. *IEEE Sens. J.*, *2020*, 1–4. https://doi.org/10.1109/SENSORS47125.2020.9278764.
46. Synopsys. (n.d.). *Synopsys OptSim Product Overview*. Available at https://www.synopsys.com/photonic-solutions/rsoft-system-design-tools/system-network-optsim.html
47. Xia, L., Cheng, R., Li, W., & Liu, D. (2015). Identical FBG-Based Quasi-Distributed Sensing by Monitoring the Microwave Responses. *IEEE Photon. Technol. Lett.*, *27*, 323–325. https://doi.org/10.1109/LPT.2014.2370650.
48. Dwivedi, K. M., Trivedi, G., & Khijwania, S. K. (2020). Theoretical study and optimization of apodized fibre Bragg grating for single and quasi-distributed structural health monitoring applications. In *30th International Conference Radioelektronika (RADIOELEKTRONIKA)*, (pp. 1–6). Bratislava, Slovakia, 2020. https://doi.org/10.1109/RADIOELEKTRONIKA49387.2020.9092399.

49. Moon, H., Kwak, S., Im, K., Kim, J., & Kim, S. (2019). Wavelength Interrogation System for Quasi-Distributed Fibre Bragg Grating Temperature Sensors Based on a 50-GHz Array Waveguide Grating. *IEEE Sens. J.*, *19*, 2598–2604. https://doi.org/10.1109/JSEN.2018.2889853.

50. Bobrovs, V., Spolitis, S., & Ivanovs, G. (2013). Extended Reach Spectrum-Sliced Passive Optical Access Network. *International Journal of Physical Sciences*, *8* (13), 537–548. https://doi.org/10.5897/IJPS2013.3868.

51. Tsai, W-S., Lu, H.H., Li, C.-Y., Lu, T.-C., Liao, C.-H., Chu, C.-A., &Peng, P.-C. (2015). A 20-m/40-Gb/s 1550-nm DFB LD-Based FSO Link. *IEEE Photonics J.*, *2015* (7), 1–7, doi: 10.1109/JPHOT.2015.2506172.

52. Ledentsov, Jr. N., Agustin, M., Chorchos, L., Kropp, J.-R., Shchukin ,V. A., Kalosha, V. P., … & Ledentsov, N. N. (2019). Energy Efficient 850-nm VCSEL Based Optical Transmitter and Receiver Link Capable of 56 Gbit/s NRZ Operation. *Vertical-Cavity Surface-Emitting Lasers XXIII*, 109380J, 1–8. https://doi.org/10.1117/12.2509916.

53. Elayoubi, K., Rissons, A., & Belmonte, A. (2018). Optical Test Bench Experiments for 1-Tb/s Satellite Feeder Uplinks. *Laser Communication and Propagation through the Atmosphere and Oceans VII*, 1077006, 1–11. https://doi.org/10.1117/12.2317728

LATVIAN JOURNAL OF PHYSICS
AND TECHNICAL SCIENCES
2023, N 4

DOI: 10.2478/lpts-2023-0026

CANCER-CAUSING AND NON-CANCER-CAUSING ASSESSMENT OF URANIUM IN GROUND WATER SAMPLES OF KANCHIPURAM DISTRICT, TAMILNADU, INDIA

M. S. Hamideen[1]*, A. Chandrasekaran[2], M. A. Neelakantan[3]

[1]Department of Physics and Basic Sciences,
Faculty of Engineering Technology,
Al-Balqa Applied University,
Amman, JORDAN
[2]Department of Physics,
Sri Sivasubramaniya Nadar College of Engineering,
Chennai -603110, Tamilnadu, INDIA
[3]National Engineering College,
Thoothukudi, Tamil Nadu, INDIA
*e-mail: mhamideen@bau.edu.jo

Uranium is characteristic lithospheric component and is found nearly in all kinds of soils and waters; in any case, its quantity changes from water-to-water contingent on their cause. Subsequently, in the current investigation, the concentration of uranium in groundwater tests was estimated utilizing LED fluorimeter and the related health hazards appraisal was checked. The concentration of uranium ranges from 0.5 to 10.7 μg L^{-1} with average value of 2.76 μg L^{-1}. The excess cancer hazard was seen in the scope of $1.416\times10^{-6} - 30.309\times10^{-6}$ with an average of 7.804×10^{-6}. This mean estimation of the excess cancer risk in the Kanchipuram locale is less than the greatest adequate degree of 1.67×10^{-4} as per AERB (2004). Consequently, there is no hurtful impact to the neighbourhood individuals who are devouring the water in the examination zone. The average cancer mortality and grimness chances were determined to show that the probability of cancer-causing chances related to water test and significant health was evaluated utilizing hazard quotient from chemical harmfulness of uranium. The values watched for hazard quotient in all areas in the examination are beneath the edge estimation of 1, as recommended by USEPA. This shows that there are no unsafe impacts on the nearby individuals in the investigation zone.

Keywords: *Health impact, ground water, LED fluorimeter, natural uranium.*

1. INTRODUCTION

In India, the primary source of drinking water is ground water. Quick industrialization and urbanization taint the ground water. Particularly, the modern exercises, for example, mining and waste water deposition may add to the gathering of radionuclides in ground water. At whatever point, such a tainted ground is devoured by individuals who are living in the region, leading to different health impacts. Uranium is a normally happening radioactive synthetic component. The concentration of uranium further increases because of anthropogenic exercises like arrival of wastage from the atomic enterprises, ignition of coal, bio-energizes and phosphate manures. Uranium is mostly found in the oxidation conditions of trivalent, tetravalent, pentavalent and hexavalent. Specifically, tetravalent uranium is insoluble in ground water and can shape buildings by different inorganic legends, for example, fluoride, chloride, sulfate, and phosphates. As indicated by the United States Environmental Protection Agency (USEPA), uranium as a cancer-causing component and zero concentration of uranium in water, just ought to be safe. Nowadays, the United States Environmental Protection Agency (USEPA) and the World Health Organization (WHO) have suggested a practical guideline reference of 30 ppb. This reference is known as Maximum Contaminant Level (MCL) [1], [2].

A significant wellbeing impacts of uranium is because of its compound poisonousness, instead of its radiological risks [3], [4]. The primary impacts are on kidneys [5]. Subsequently, the main goals of the current study are to (i) determine the concentration of uranium in ground water tests of Kanchipuram district, Tamilnadu; (ii) ascertain the radiation hazards related to concentration of uranium in ground water; (iii) survey the frequency distribution of uranium and related risks in ground water tests by measurable examinations.

2. METHODOLOGY

2.1. Collection and Preparation of Samples

A groundwater tests were gathered from 20 areas in Kanchipuram region, Tamilnadu, from physically worked hand-siphons set up by city organisations in private regions. Before assortment, the water tests were sifted utilizing 0.45 µm Whatman filter paper to eliminate suspended issue/dregs, fermented with supra unadulterated nitric corrosive (HNO_3) for protection and afterward put away in pre-cleaned corrosive washed high thickness polyethylene (HDPE) compartments until investigation. The ground water examining areas are shown in Fig. 1. Also, latitude and longitude lines of each examining area are demonstrated in Table 1.

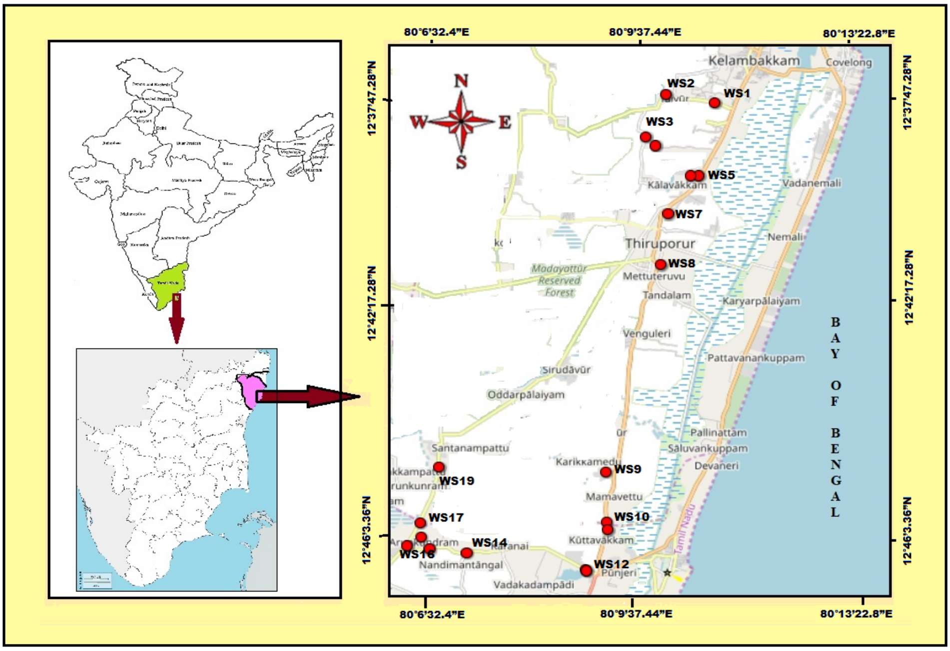

Fig. 1. The ground water sampling locations in the examination area.

Table 1. Geographical Information of Sampling Locations in Kanchipuram District, Tamilnadu

Sample No.	Sample ID	Locations	Latitude	Longitude
1	WS-1	Thaiyur-I	12˚46'22.6776"N	80˚12'25.4988"E
2	WS-2	Thaiyur-II	12˚46'32.736"N	80˚11'29.1084"E
3	WS-3	Koman Nagar-I	12˚45'42.1452"N	80˚11'5.7012"E
4	WS-4	Koman Nagar-II	12˚45'31.41"N	80˚11'16.0944"E
5	WS-5	Kalavakkam-I	12˚44'55.0356"N	80˚12'6.5916"E
6	WS-6	Kalavakkam-II	12˚44'54.924"N	80˚11'56.4144"E
7	WS-7	Kannagapattu	12˚44'8.9448"N	80˚11'31.2144"E
8	WS-8	Tiruporur	12˚43'7.7988"N	80˚11'22.6392"E
9	WS-9	Paiyanoor	12˚38'58.3656"N	80˚10'18.3324"E
10	WS-10	Koothavakkam-I	12˚37'57.0648"N	80˚10'19.9524"E
11	WS-11	Koothavakkam-II	12˚37'48.4176"N	80˚10'20.2332"E
12	WS-12	Poonjeri-I	12˚36'58.7772"N	80˚9'55.2996"E
13	WS-13	Poonjeri-II	12˚36'59.9292"N	80˚9'54.306"E
14	WS-14	Vadakadampadi	12˚37'20.082"N	80˚7'35.832"E
15	WS - 15	Kuzhipanthandalam	12˚37'25.4064"N	80˚6'52.3512"E
16	WS-16	Eitchur	12˚37'28.1676"N	80˚6'27.5328"E
17	WS-17	Azhagunattham-I	12˚37'56.4996"N	80˚6'41.4396"E
18	WS-18	Azhagunattham-II	12˚37'39.376"N	80˚6'43.6032"E
19	WS-19	Amayapattu	12˚39'4.266"N	80˚7'3.9576"E
20	WS-20	Siruthavoor	12˚39'14.292"N	80˚7'4.4184"E

2.2. LED Florimeter Analysis

Ground water tests were tried for uranium content using LED fluorimeter (Quantalase LF-2a). Quality affirmation of the data was made by the assessment of IAEA standard reference materials and by reproducing examination and spike recovery. Fluorescence yield varies in different structures of uranium. Subsequently, an inorganic reagent fluren was added to the example to change all the structures in a solitary structure having the same fluorescence yield. Six millilitres of the sample with 10% fluren was taken in a cuvette created utilizing overly low fluorescence merged silica and a short time later they were researched for uranium in the fluorimeter.

3. RESULTS AND DISCUSSION

3.1. Uranium Activity Concentration in Ground Water

Deliberate tests of 20 areas in Kanchipuram region, Tamilnadu, are provided in Table 2. As can be observed in Table 2, the uranium content differs in the range of 0.50–10.7 µg L^{-1} with an average value of 2.76 µg L^{-1}. This shows that uranium concentration in all the tested areas and the average value do not exceed the permissible limit of 60 µg L^{-1} of uranium in groundwater suggested by AERB (2004), 30 µg L^{-1} by US-EPA (2000), 15 µg L^{-1} by WHO (2011), 9 µg L^{-1} by UNSCEAR (1982), 1.9 ppb by ICRP (1993) [2],[7]–[10]. This shows that uranium concentration in water tests is not sufficient to cause wellbeing impacts.

Table 2. Uranium Concentration and Some Radiation Health Impacts in Ground Water Tests

Sample No.	Sample ID	Locations	Natural Uranium (µg L^{-1})	Excess Cancer Risk (ECR) $\times10^{-6}$	LADD µg Kg^{-1} day^{-1}	Hazard Quotient (HQ)	Annual Effective Dose (AED) $\times10^{-8}$ µSv/Year
1	WS-1	Thaiyur-I	1.5	4.249	0.087	0.019	85.95
2	WS-2	Thaiyur-II	0.8	2.266	0.046	0.010	45.84
3	WS-3	Koman Nagar-I	4.4	12.464	0.255	0.056	252.12
4	WS-4	Koman Nagar-II	10.7	30.310	0.619	0.137	613.11
5	WS-5	Kalavakkam-I	2	5.665	0.116	0.026	114.60
6	WS-6	Kalavakkam-II	1.1	3.116	0.064	0.014	63.03
7	WS-7	Kannagapattu	2.9	8.215	0.168	0.037	166.17
8	WS-8	Tiruporur	6	16.996	0.347	0.077	343.81
9	WS-9	Paiyanoor	7.3	20.679	0.422	0.093	418.30
10	WS-10	Koothavakkam-I	0.7	1.983	0.041	0.009	40.11
11	WS-11	Koothavakkam-II	0.7	1.983	0.041	0.009	40.11
12	WS-12	Poonjeri-I	2.2	6.232	0.127	0.028	126.06
13	WS-13	Poonjeri-II	0.5	1.416	0.029	0.006	28.65
14	WS-14	Vadakadampadi	3	8.498	0.174	0.038	171.90

15	WS - 15	Kuzhipanthan-dalam	3.7	10.481	0.214	0.047	212.01
16	WS-16	Eitchur	0.8	2.266	0.046	0.010	45.84
17	WS-17	Azhagunattham-I	1	2.833	0.058	0.013	57.30
18	WS-18	Azhagunattham-II	1.2	3.399	0.069	0.015	68.76
19	WS-19	Amayapattu	3.7	10.481	0.214	0.047	212.01
20	WS-20	Siruthavoor	0.9	2.549	0.052	0.011	51.57
Average			2.76	7.804	0.159	0.035	157.86

The variety of uranium concentration of ground water tests in Kanchipuram district, Tamilnadu, is demonstrated in Fig. 2. Also, a comparison of uranium content of the present research with other studies carried out in a variety of countries is presented in Table 3. The distribution of uranium contents with water sampling locations in this study is illustrated in Fig. 2.

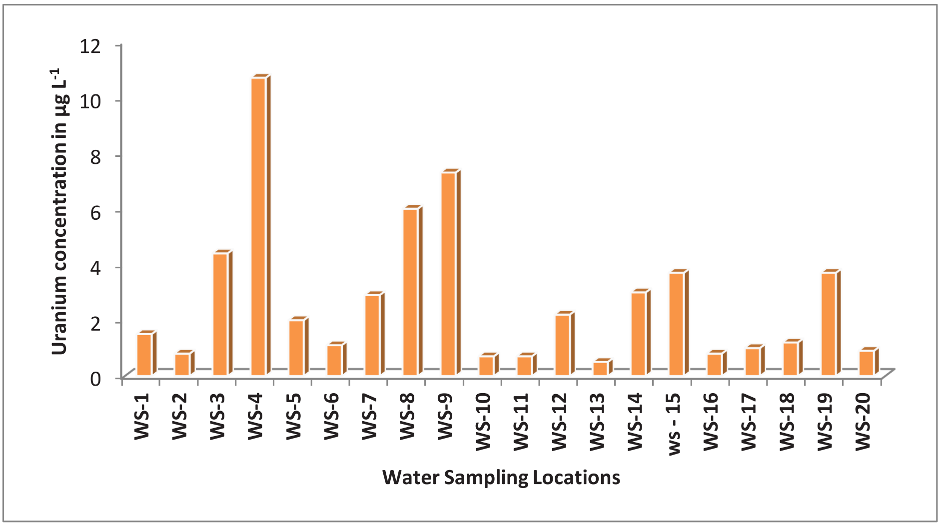

Fig. 2. Uranium concentration in ground water samples in the examination area.

3.2 Cancer-Causing Uranium Assessment

An admission of the uranium through ground water brings about the both cancer-causing and non-cancer-causing dangers. Thus, to survey the health impacts through ground water tests in Kanchipuram district, Tamilnadu, the radiological and chemical hazard appraisal was performed. In the current examination, the excess cancer risk (ECR), lifetime average daily dose (LADD) and hazard quotient were determined to comprehend the health hazard impact.

3.2.1. Excess Cancer Risk (ECR)

An excess cancer risk has been utilized to test the likelihood of radiogenic disease mortality or dismalness per unit admission for a given radionuclide internally or per unit dose externally. Henceforth, excess cancer hazards have been determined utilizing the equation given by the USEPA [1].

$$ECR = U_A \times R_F \times I_W, \qquad (1)$$

where ECR stands for Excess Cancer Risk, U_A is uranium contents (Bq L^{-1}) and R_F is Risk Factor. R_F for uranium is 1.19×10^{-9} for mortality and I_W is per capita action consumption. Here, (I_W) for tested radionuclides is determined as multiply of average life duration (63.7 years), and daily utilization of water as 4.05 L day^{-1}. The determined ECR estimations of ground water tests of Kanchipuram region, Tamilnadu, are provided in Table 2.

Table 3. Uranium Concentration in Other Studies Compared to the Present Researchg

Country	Range of concentration of Uranium (ppb)	References
Hungary	0.08–75.3	[8]
Germany	0.032–48.4	[8]
Switzerland	0.05–92.02	[9]
Aligarh, UP, India	38–471.27	[13]
Punjab, India	1.39–98.25	[14]
Kolar, Karnataka, India	0.3–1442.9	[14]
Hyderabad, India	0.6–82.0	[13]
Jaduguda, India	0.03–11.6	[13]
Kanchipuram, Tamilnadu, India	**0.50–10.70**	**Present Study**

The malignant growth hazard has been seen to be in the scope of $1.416\times10-6$ – $30.309\times10-6$ with a normal of $7.804\times10-6$. This mean estimation of the excess cancer risk in the Kanchipuram region is less than the most extreme satisfactory degree of 1.67×10^{-4} as indicated by AERB (2004). Consequently, there is no hurtful impact on the neighbourhood individuals who are expending the water in the examination zone [7]. The measured values of ECR in each location are shown in Table 2. Also, ECR values of the present research compared to other studies carried out in a variety of countries are demonstrated in Table 4.

3.3. Non-Cancer-Causing Uranium Assessment

Uranium has wellbeing effects on account of its both radioactive and chemical behaviours. If we think about chemical destructiveness of the uranium, the kidney is the most critical target tissue of the human body. The destructiveness of uranium rules over its chemical poisonousness on the kidney even at small amounts. Along these lines, lifetime average daily dose (LADD) and hazard quotient (HQ) were estimated to examine the compound harmfulness [11].

3.3.1. Lifetime Average Daily Dose (LADD)

Lifetime average daily dose (LADD) of a radioactive material in ground water admission is characterised as the amount of the radioactive material swallowed for one kilogram of a person a day and it is determined using the accompanying expression [12].

$$LADD = \frac{U_A \times I_R \times E_D \times E_F}{A_T \times B_w \times 365} \qquad (2)$$

where U_A is radioactive material contents (μg L^{-1}), I_R is utilization rate (4.05 L day^{-1}), E_D is average exposure duration (63.7 years), E_F is average exposure time (365 days y^{-1}), B_W is average person weight (70kg), and A_T is average age (63.7 years). The determined estimations of LADD are provided in Table 2. In the current study, the LADD estimations of all the locations vary from 0.029 to 0.619 μg Kg^{-1} day^{-1} with mean estimation of 0.159 μg Kg^{-1} day^{-1}. The measured values of LADD in each location are shown in Table 2.

3.3.2. Annual Effective Dose (AED)

Annual effective dose (AED) of the uranium through ground water admission is characterised as the amount of the uranium dose ingested by human every year and it is calculated by the next expression.

$$AED = U_A \times D_F \times I_A, \quad (3)$$

where U_A is radioactive material concentration (Bq/L), D_F is effective dose for each swallow (4.5 x 10^{-8} μSv/Year/Bq/L) and I_A is annual swallow quantity (503.7 L=1.38 x 365). As observed in Table 2, annual effective dose was found between 28.65×10^{-8} and 613.11×10^{-8} μSv/Year with the mean estimation of 157.8×10^{-8} μSv/. The mean value is underneath the suggested ones, reaching 0.1 mSv [2]. The measured values of AED in each location are shown in Table 2.

Table 4. ELCR Comparison of the Present Study with Other Works

Country	Range of ELCR ($X10^{-6}$)	References
Vishakhapatnam, India	1.3–4.84	[13]
Bathinda District (S. Punjab), India	0.69–5.29	[14]
Tiruvannamalai, Tamilnadu	0.09–11.16	[14]
Kanchipuram, Tamilnadu, India	**1.416–30.310**	**Present Study**

3.3.3. Hazard Quotient (hq)

A danger of the compound poison might be portrayed by risk quotient [12]. This is the proportion of LADD of a substance to a reference quantity (RfD). Hazard (risk) quotient is underneath unity meaning that antagonistic impacts are probably not going to happen. The RfD of uranium (4.53 μg Kg^{-1} day^{-1}) was considered from USEPA [1].

$$HQ = \frac{LADD}{RfD} \quad (4)$$

If HQ > 1.00, at that point the LADD of a specific metal surpasses the RfD, demonstrating that there is a potential danger related to that metal. The determined ground water hazard quotient estimations of tests are given in Table 2. As observed in Table 2, values in all the examination areas are beneath the limit estimation of 1, as recommended by USEPA [1]. This shows that there is no harmful impact on the nearby individuals in the examination zone. The measured values of HQ in each location are shown in Table 2.

4. CONCLUSIONS

Natural uranium concentration was estimated in ground water tests of Kanchipuram district, Tamilnadu utilizing LED Fluorimeter. The determined mean estimation of radiological boundaries, for example, excess cancer risk, lifetime average daily dose (LADD), annual effective dose and hazard quotient were contrasted with the suggested limit given by WHO and AERB. According to uranium investigation of ground water tests in the Kanchipuram district, the chemical destructiveness of uranium in the zone is immaterial and underneath as far as possible the limit proposed by WHO and AERB. Consequently, ground water tests are reasonable for drinking and farming purposes.

REFERENCES

1. USEPA. (2012). *Drinking Water Standards and Health Advisories*. Washington DC U.S.A., EPA 822-S-12-001.
2. WHO. (2011). *Guidelines for Drinking Water Quality*. World Health Organization, Geneva Switzerland.
3. WHO. (1998). *Guidelines for Drinking Water Quality*. World Health Organization, Geneva Switzerland.
4. Jakhu, R., Mehra, R., & Mittal, H.M. (2016). Exposure Assessment of Natural Uranium from Drinking Water. *Environ. Sci.: Processes Impacts Environ*., *18* (12).
5. Domingo, J.L. (1995). Developmental Toxicity of Metal Chelating Agents. *Reprod. Toxicol., 9* (2), 105–113.
6. Mudge, M.R., & Earhart, R.L. (1980). *Geological Survey Professional Paper 1174*. Library of Congress Cataloging-in-Publication Data.
7. AERB. (2004). *Drinking Water Specifications in India*. Department of Atomic Energy, Govt. of India.
8. USEPA. (2000). *National Primary Drinking Water Regulations, Radionuclides*. Final Rule. Washington, DC: United States Environmental Protection Agency.
9. United Nations Scientific Committee on the Effects of Atomic Radiation (UNSCEAR). (1982). *Ionizing Radiation: Sources and Biological Effects*. New York, NY, USA.
10. International Commission on Radiological Protection (ICRP). (1993). ICRP Publication 65. *Annals of the ICRP, 23* (2). Oxford: Pergamon Press.
11. Kumar, A., Usha, N., Sawant, P.D., Tripathi, R.M., Raj, S.S., Mishra, M., … & Kushwaha, S. (2011). Risk Assessment for Natural Uranium in Subsurface Water of Punjab State, India. *Hum. Ecol. Risk Assess, 17* (2)
12. Virk, H.S. (2016). Measurement of Concentration of Natural Uranium in Ground Waters of Bathinda District (S. Punjab) for the Assessment of Annual Effective Dose. *Global J. of Human-Soc. Sci.: B Geography*, 16.
13. Ravisankar, R., Vanasundari, K., Suganya, M., Raghu, Y., Rajalakshmi, A. Chandrasekaran, A., & Vijayagopal, P. B. (2014). Multivariate Statistical Analysis of Radiological Data of Building Materials Used in Tiruvannamalai, Tamilnadu, India. *Appl. Radiat. Isot., 85*.
14. Ravisankar, R., Raghu, Y., Chandrasekaran, A., Suresh Gandhi, M., & Vijayagopal, P. (2016). Determination of Natural Radioactivity and the Associated Radiation Hazards in Building Materials Used in Polur, Tiruvannamalai District, Tamilnadu, India Using Gamma Ray Spectrometry with Statistical Approach. *J. of Geoch. Expl., 163*.